Development and Characterization of a Unique Photoactivatable Label

Zur Erlangung des akademischen Grades eines

DOKTORS DER NATURWISSENSCHAFTEN

(Dr. rer. nat.)

Fakultät für Chemie und Biowissenschaften
Karlsruher Institut für Technologie (KIT) - Universitätsbereich

genehmigte

DISSERTATION

von

Dipl.-Biochem. Susan Gayda

aus

Leipzig

Juni 2011

Dekan: Prof. D. Stefan Bräse
Referent: Prof. Dr. Gerd Ulrich Nienhaus
Korreferent: Prof. Dr. Tilman Lamparter
Tag der mündlichen Prüfung: 13.07.2011

Contents

List of Figures VII

List of Symbols IX

Introduction 1

Relevance of Photoactivatable Fluorescent Proteins 1
Thesis Outline 2

I Scientific Background 3

1 GFP-like Fluorescent Proteins **5**
1.1 Properties of GFP-like Fluorescent Proteins 6
1.1.1 Three-Dimensional Structure 6
1.1.2 Formation of the 'GFP'-Chromophore, *p*-HBI 7
1.1.3 Modifications of the *p*-HBI Chromophore 8
1.1.4 Diversity Among GFP-like Proteins 9
1.2 Photophysical Properties of GFP-like proteins 10
1.2.1 Spectroscopic Properties of the Chromophore 10
1.2.2 pH Sensitivity of the Chromophore 11
1.2.3 Excited State Proton Transfer 12
1.2.4 Blinking 13
1.2.5 Shift in Emission Color 15
1.3 Photoactivatable Fluorescent Proteins 15
1.3.1 Irreversible Photoconversion 16
1.3.2 Reversible Photoactivation - Photoswitching 22
1.3.3 PAFPs Showing Reversible AND Irreversible Photoactivation 25
1.4 FPs in Superresolution Live-Cell Imaging 25

II Materials and Methods 29

2 Molecular Biology 31
- 2.1 Mutagenesis 31
  - 2.1.1 Site-Directed Mutagenesis 31
  - 2.1.2 Random Mutagenesis — *Error Prone* PCR 33
- 2.2 Protein Expression and Purification 35
  - 2.2.1 Cell Culturing 35
  - 2.2.2 Protein Purification 35
  - 2.2.3 Analytical Gel Filtration 36

3 Tracking Structural Modifications by Spectroscopy 39
- 3.1 Principles of Light-Matter Interaction 39
- 3.2 Absorption Spectroscopy 42
- 3.3 Circular Dichroism 45
- 3.4 Fluorescence 45

III Results and Discussion 51

4 Combining Reversible and Irreversible Switching Modes - IrisFP 53
- 4.1 Introduction 53
  - 4.1.1 Structural Background of Photoinduced Color Changes 54
- 4.2 Spectroscopic Characterization of IrisFP 57
- 4.3 Photoactivation in IrisFP 62
  - 4.3.1 General Aspects of Photoswitching 62
  - 4.3.2 Green-to-Red Photoconversion 66
  - 4.3.3 Modulation of Irreversible and Reversible Photoactivation Modes 68
- 4.4 Summary and Conclusions 72

5 A Genetic Label with Multiple Photoactivation Modes – mIrisFP 75
- 5.1 Introduction 75
- 5.2 Semi-rational Engineering of mIrisFP 76
  - 5.2.1 Molecular Engineering 76
- 5.3 Photophysical Characterization of mIrisFP 80
  - 5.3.1 The Thermally Relaxed Ground State 81
  - 5.3.2 Photoactivation 82
- 5.4 Applications of mIrisFP 85

5.4.1 mIrisFP as a Genetically Encoded Marker 85
5.4.2 Combining Pulse-Chase Experiments and Superresolution Imaging 85
5.5 Summary and Conclusion 90

6 Investigation of Photoswitching Using mIrisGFP 91
6.1 mIrisGFP – a Model System 91
6.2 Spectroscopic Characterization of mIrisGFP 91
6.3 Effect of pH on the Thermal Equilibrium of the mIrisGFP Chromophore 93
6.3.1 Protonation Equilibrium of the *Cis* Chromophore 93
6.3.2 Protonation Equilibrium of the *Trans* Chromophore 98
6.3.3 Structural Interpretation of the Protonation Equilibrium Shift upon *Cis*-*Trans* Isomerization of the Chromophore 100
6.4 Chromophore Interconversion in mIrisGFP at the Macroscopic Level . 100
6.4.1 Wavelength Dependence of Photoswitching 100
6.4.2 Exciting the Anionic Chromophore 102
6.4.3 Thermal Recovery of the *Cis* Chromophore 107
6.4.4 Excitation of the Neutral Chromophore 110
6.5 Energetic Interpretation: Interconversion of the Chromophore Species on the Microscopic Level 114
6.5.1 Exciting the Anionic *Cis* Chromophore - Along the 'Green Pathway' 115
6.5.2 Thermal Recovery of the *Cis* Chromophore - Along the 'Red Pathway' 118
6.5.3 Exciting the Neutral *Cis* Chromophore - Along the 'Blue Pathway' 119
6.5.4 Exciting the Neutral *Trans* Chromophore - Along the 'Gray Pathway' 120
6.6 Summary and Conclusions 121

Summary 123
Zusammenfassung 126

Bibliography 145

Appendix i
Danksagung i
List of Publications iii

Curriculum Vitae vii

List of Figures

1.1 Structure of GFP-like Proteins. 7
1.2 Formation of the *p*-HBI Chromophore. 8
1.3 Variations of the Chromophore. 9
1.4 pH sensitivity of EGFP. 11
1.5 Model of chromophore protonation energetically coupled to an adjacent residue. 12
1.6 Excited State Proton Transfer 13
1.7 Single molecule fluorescence trajectories of GFP S65T. 14
1.8 Green-to-red photoconversion of GFP. 15
1.9 Photoactivation in PA-GFP. 17
1.10 Photoactivation in PAmCherry. 18
1.11 Photoconversion in EosFP. 20
1.12 Natural occurrence and spectral properties of EosFP. 21
1.13 Photoconversion in EosFP. 21
1.14 Reversible photoswitching in Dronpa. 22
1.15 Photoswitching of Dronpa variants featuring a positive and a negative switching mode. 24
1.16 Schematic illustration of the principle of PALM. 27

2.1 Schematic illustration of site-directed mutagenesis. 32
2.2 Principle of the generation of random clones. 33
2.3 Steps of protein purification by affinity chromatography utilizing a TALON® matrix. 36

3.1 Jablonski diagram. 40
3.2 Schematic illustration of the Frank-Condon principle. 41
3.3 Absorption of light passing through a sample. 42

3.4 Optical setup for the photoswitching experiments mounted at the Fluorolog II fluorometer. 47
3.5 Time traces of the emission intensity during photoswitching. 47

4.1 IrisFP protein solution after different illumination conditions. 54
4.2 IrisFP crystals under different illumination conditions. 54
4.3 Structural differences between EosFP and IrisFP in the chromophore vicinity. 55
4.4 Structural changes in the chromophore vicinity of IrisFP upon photoswitching. 57
4.5 Spectroscopic comparison of EosFP and IrisFP. 59
4.6 pH-dependence of thermally relaxed IrisFP. 60
4.7 Spectral changes of IrisFP upon pH variation. 61
4.8 Photoinduced transformations in IrisFP. 62
4.9 Spectroscopic changes upon photoactivation. 63
4.10 Thermal recovery of IrisFP. 64
4.11 Time traces of IrisFP photoactivation. 65
4.12 Photoswitching cycles of IrisFP. 66
4.13 Photoconversion in IrisFP and its side effects. 67
4.14 Action spectra of IrisFP. 69
4.15 Schematic illustration of the photoreactions during 390 nm-illumination. 71

5.1 Structural changes in mIrisFP. 76
5.2 Amino acid sequence alignment of several monomeric anthozoa FPs and mIrisFP. 78
5.3 Oligomerization of mIrisFP and its predecessors. 79
5.4 Absorption and fluorescence spectra of mIrisFP and IrisFP. 81
5.5 pH-dependence of the thermally relaxed mIrisFP. 82
5.6 Time traces of photoactivation and thermal recovery in mIrisFP. . . . 83
5.7 Spectral changes upon photoactivation. 84
5.8 Combined pulse-chase experiments and superresolution imaging utilizing mIrisFP. 87
5.9 Focal adhesion dynamics in a live HeLa cell expressing paxillin-mIrisFP. 89

6.1 Spectral properties of mIrisGFP. 93
6.2 pH dependence of optical spectra of mIrisGFP in thermal equilibrium. 94
6.3 pH-dependence of optical band intensities and positions of the thermally relaxed mIrisGFP chromophore. 95

6.4 Schematic illustration of the protonation equilibrium of the mIrisGFP chromophore interacting with adjacent amino acid side chains. 96
6.5 Schematic illustration of the hydrogen bonding network below the chromophore upon pH change. 97
6.6 Shift of mIrisGFP Glu212Gln absorption bands. 98
6.7 pH-dependent optical spectra of the mIrisGFP chromophore in the *trans* state. 99
6.8 Shift of the *trans* chromophore bands with pH. 99
6.9 Eight-state model comprising the possible chromophore species of mIrisGFP. 101
6.10 Wavelength dependence of the off switching in mIrisGFP. 102
6.11 Off switching by excitation within the neutral chromophore band. . . 103
6.12 UV/visible spectra of mIrisGFP, pH 6, before and after illumination with 473-nm light. 104
6.13 pH dependence of the off switching quantum efficiency, ϕ_{off}. 105
6.14 Off switching by different excitation powers. 106
6.15 Absorption spectra collected during thermal recovery of mIrisGFP at pH 7, 310 K. 108
6.16 pH dependence of the *trans*-to-*cis* isomerization. 109
6.17 Structural rearrangements around the *trans* chromophore upon pH changes. 110
6.18 Spectral changes upon off switching with 405-nm light. 112
6.19 Time traces of the decrease in emission intensity during off switching with 405-nm light. 113
6.20 Isomerization/protonation pathways in mIrisGFP from the energetic point of view. 115
6.21 Temperature sensitivity of the off switching. 116
6.22 Temperature dependence of the mIrisGFP emission spectrum. 117
6.23 Autocorrelation curve of mIrisGFP. 118
6.24 Off switching in the presence and absence of molecular oxygen. 119

List of Symbols

FUNDAMENTAL CONSTANTS

c	speed of light
E	energy
h	Planck's constant
k_b	Boltzmann constant
λ	wavelength
ν	frequency
N_A	Avogadro's number
R	gas constant

EXPERIMENTAL PARAMETERS

A	absorption
β	stretching factor
c	molecular concentration
d	sample thickness
ΔG	Gibbs free energy
ΔH^*	activation enthalpy
ΔS^*	activation entropy
ε	molecular extinction coefficient
n	refractive index
Γ	Gamma function
I_0	intensity of the incident light
I	intensity if the emergent light
k	rate coefficient
K_D	dissociation coefficient

MW	molecular mass
MW_0	molecular mass of a monomeric protein
n	Hill coefficient
P	power density
ϕ	quantum efficiency of a particular process
τ	lifetime
Θ	ellipticity

Absorption Bands

A band	absorption band of a neutral chromophore
B band	absorption band of an anionic chromophore
$\mathrm{A}_\mathrm{c}^\mathrm{G}$	neutral *cis* chromophore of the green form
$\mathrm{A}_\mathrm{t}^\mathrm{G}$	neutral *trans* chromophore of the green form
$\mathrm{B}_\mathrm{c}^\mathrm{G}$	anionic *cis* chromophore of the green form
$\mathrm{A}_\mathrm{c}^\mathrm{R}$	neutral *cis* chromophore of the red form
$\mathrm{A}_\mathrm{t}^\mathrm{R}$	neutral *trans* chromophore of the red form
$\mathrm{B}_\mathrm{c}^\mathrm{R}$	anionic *cis* chromophore of the red form

Spectroscopic Parameters

$\varepsilon_c(\lambda)$	molar extinction coefficient of the *cis* state
$\varepsilon_t(\lambda)$	molar extinction coefficient of the *trans* state
λ_max	peak wavelength
ϕ_fl	fluorescence quantum yield

Species of Photoactivation

cG	*cis* green state
tG	*trans* green state
cR	*cis* red state
tR	*trans* red state

C^H	neutral *cis* chromophore
T^H	neutral *trans* chromophore

C^-	anionic *cis* chromophore
T^-	anionic *trans* chromophore

C^{H*}	excited neutral *cis* chromophore
T^{H*}	excited neutral *trans* chromophore
C^{-*}	excited anionic *cis* chromophore
T^{-*}	excited anionic *trans* chromophore

Parameters of Photoactivation

k_{rec}	rate coefficient of thermal recovery
τ_{rec}	lifetime of the *trans* chromophore
k_{ct}	rate coefficient of *cis*-to-*trans* photoisomerization
k_{tc}	rate coefficient of *trans*-to-*cis* photoisomerization
ϕ_{ct}	quantum efficiency of *cis*-to-*trans* photoisomerization
ϕ_{tc}	quantum efficiency of *trans*-to-*cis* photoisomerization

Apparent rate coefficient of:

k_{GR}	green-to-red photoconversion
k_{off}	off switching
$k_{\mathrm{off}}^{\mathrm{G}}$	on switching of the green form
$k_{\mathrm{off}}^{\mathrm{R}}$	off switching of the red form
k_{on}	on switching
$k_{\mathrm{on}}^{\mathrm{G}}$	on switching of the green form
$k_{\mathrm{on}}^{\mathrm{R}}$	on switching of the red form

Apparent quantum efficiency of:

ϕ_{GR}	green-to-red photoconversion
ϕ_{off}	off switching
$\phi_{\mathrm{off}}^{\mathrm{G}}$	off switching of the green form
$\phi_{\mathrm{off}}^{\mathrm{R}}$	off switching of the red form
ϕ_{on}	on switching
$\phi_{\mathrm{on}}^{\mathrm{G}}$	on switching of the green form
$\phi_{\mathrm{on}}^{\mathrm{R}}$	on switching of the red form

Introduction

Relevance of Photoactivatable Fluorescent Proteins

In the past two decades, GFP-like fluorescent proteins have emerged as important tools in live-cell imaging. In contrast to extrinsic labeling methods, fluorescent protein labels can be genetically encoded. Introducing the cDNA sequence of a fluorescent protein into the gene pool of the cell of interest enables expression of the fluorescent label by the cell itself, rendering the introduction of the marker minimally invasive. Furthermore, fusion of the gene of the fluorescent protein to that of another protein of interest allows precise targeting of intra-cellular components. Because of this combination of accuracy and non-invasiveness, fluorescent proteins are very attractive for live-cell imaging, even though other labeling techniques often yield brighter signals.

Fluorescent proteins are sensitive probes of their environment, and are, therefore, utilized in a broad range of applications, such as: probes of gene expression[1,2], calcium sensors[3,4], pH indicators[5], sensors for protein-protein interactions, and even voltage[1,6]. Photoactivatable fluorescent proteins extend this range even further. This class has emission characteristics that can be controlled through the irradiation with light of specific optical wavelengths. Some of these proteins efficiently change their emission color upon illumination and, therefore, permit to distinguish between subpopulations. This capability is utilized in pulse-chase experiments where a group of proteins within a cell is defined spatially by irradiation with the activating light, allowing their subsequent tracking. This technique reveals processes invisible in steady state, such as protein diffusion or exchange between compartments[7,8]. Recently, photoswitchable fluorescent proteins, which reversibly alter their emission intensity between a dark and bright state, have been identified. Both groups of photoactivatable fluorescent proteins have found widespread application as probes in superresolution microscopy techniques[9–13]. However, a particular photoactivation pathway can be utilized either for imaging, or for pulse-chase experiments, but not for both. Here, we present and characterize a label that combines both photoactivation modes, thereby allowing the combination of pulse-chase and superresolution imaging in a single experiment. Furthermore, the project aimed at a detailed characterization of the protein and its individual photoactivation pathways to provide a molecular understanding of the underlying photophysics and photochemistry. This knowledge will be beneficial for optimizing the experimental conditions, and for further developments of the label itself.

Thesis Outline

The scope of this thesis is to develop and characterize new photoactivatable fluorescent proteins, based on the current state of scientific knowledge, which is summarized in Chapter I. The experimental methods are briefly explained in Part II, describing the utilized methods of molecular biology (Chapter 2) and the spectroscopical methods and evaluation procedures (Chapter 3). In the main body of this thesis, Part III, we describe the history of a new photoactivatable fluorescent protein, starting from its discovery by Virgile Adam in a random clone of the well established green-to-red photoactivatable protein EosFP. This new protein, termed IrisFP, exhibits multiple photoinducible functionalities, the characteristics and interdependencies of which are discussed in Chapter 4. Chapter 5 describes the development of a monomeric version of the protein, mIrisFP. Here, we present a detailed characterization of this protein and its application in live-cell superresolution imaging, which demonstrates the advantages of the new genetic label over previously introduced photoactivatable fluorescent proteins.

The photophysical background of the photoswitching reaction is investigated in great detail for an analogue of mIrisFP, mIrisGFP. The results of this investigation are described and discussed in Chapter 6. Based on these findings, we propose a model that illustrates the interdependence of four chromophore species in the ground and excited states that are involved in the photoswitching reaction. In the conclusion section, we propose the utilization of the obtained knowledge in the application of mIrisFP in superresolution imaging.

Part I

Scientific Background

Chapter 1

GFP-like Fluorescent Proteins

Fluorescence of proteins is a widespread phenomenon, typically observed in proteins involved in redox reactions, which become fluorescent by incorporation of an aromatic cofactor as chromophore. In some marine organisms, among them several classes of *cnidaria*, proteins have been identified that encode a chromophore forming tripeptide motif, X-Tyr-Gly, with X representing any amino acid. The first of these amino acids, X, is highly variable, while the second (Tyr) and the third one (Gly) are strictly conserved among these naturally occurring *f*luorescent *p*roteins (FPs). The first protein of this family was the *g*reen *f*luorescent *p*rotein, GFP. In 1962, Osamu Shimomura isolated the protein from tissue extracts of the jellyfish *Aequorea victoria*[14]. He characterized the optical properties of *av*GFP and succeeded in identifying the chemical nature of the chromophore in 1979[15]. In 1992, recombinant expression of this protein was enabled by the cloning of the *av*GFP gene by Prasher and co-workers[16]. Soon thereafter, Martin Chalfie and collaborators recognized its potential as a genetically encoded marker in living organism and used it to quantify gene expression in *Caenorhabditis elegans*[17]. That finding inspired new interest in GFP, promoting detailed studies of its structure-function relationship and photophysical properties. It was shown that *av*GFP maturates autocatalytically into its functional fluorescent form with oxygen as the only additional required ingredient. The autocatalytical chromophore formation facilitates the function of *av*GFP in essentially all aerobic organisms, which led to its widespread utilization in a variety of applications, particularly in advanced live-cell imaging techniques using light microscopy. These achievements were recognized by the 2008 Nobel Prize in Chemistry awarded to Shimomura, Chalfie and Tsien for "the discovery and development of the green fluorescent protein, GFP"[18,19]. The development of differently colored GFP variants[20] and the discovery of red emitting proteins in non-bioluminescent anthozoa in the late 1990s[21] was a great improvement especially for imaging applications by allowing multicolor labeling or *F*örster *r*esonance *e*nergy *t*ransfer (FRET) experiments. Moreover, orange and red emitting FPs are preferable in live-cell and tissue imaging because of the reduced cellular autofluorescence, scattering in the red spectral range, and the reduced phototoxicity of the required excitation light.

Meanwhile, fluorescent proteins have been discovered even in organisms evolutionarily distant from cnidaria, including crustaceans[22], comb jellies[23], and chordates (lancelets)[24]. These proteins are structurally and photophysically very similar to GFP and are therefore collectively termed GFP-like proteins.

1.1 Properties of GFP-like Fluorescent Proteins

1.1.1 Three-Dimensional Structure

GFP-like proteins fold into a rigid 11-stranded β-can structure. The β-can surrounds a central α-helix, which is interrupted by the chromophore close to the geometric center of the protein (Figure 1.1)[25–27]. Surrounding the chromophore, adjacent amino acid residues and structural water molecules establish a tight hydrogen bonding network, which anchors the chromophore in a more or less planar conformation, depending on the particular FP. Short helical sections and loops close off the ends of the β-can, protecting the chromophore from extrinsic molecules.

The protomers of GFP-like proteins tend to form oligomeric structures. The oligomerization tendency correlates with the organisms the protein was originally isolated from. *av*GFP is considered monomeric, even though it forms dimers at high concentration[28]. In contrast, GFP from the sea pansy *Renilla*[29] occurs as a strongly bound dimer, even at very low concentration. Among natural anthozoan FPs even tetramers are frequently found[30,31]. DsRed, a red FP isolated from *Discosoma sp.*, was the first tetrameric FP with its structure solved by crystallography[32,33]. Each of the four subunits, termed A to D, interacts with two other ones, forming two different interfaces (Figure 1.1)[27,34]. The extended interface, denoted by A/B (C/D), is hydrophilic, stabilized by salt bridges and hydrogen bonds between polar residues and structural water molecules[33,35]. The smaller interface, denoted by A/C (B/D), is hydrophobic, reinforced by a cluster of hydrophobic amino acids. Overall, the resulting tetramer can be viewed as two interacting dimers with each of those dimers established by antiparallel associated monomers.

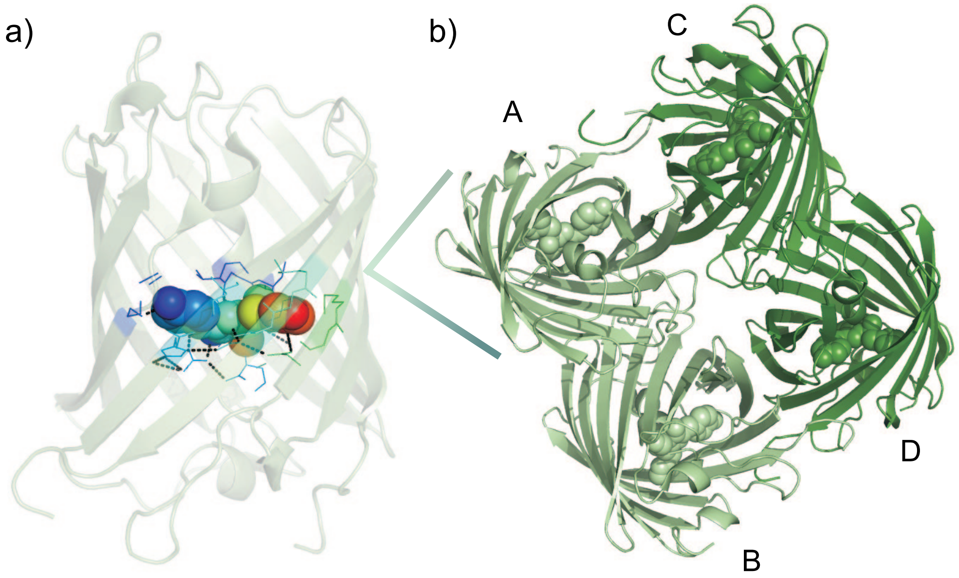

Figure 1.1: Structure of GFP-like Proteins. (a) Protomer of a GFP-like protein, forming the typical 11-stranded β-barrel, which surrounds the central α-helix with the chromophore. The chromophore atoms are depicted as spheres, color coded on a temperature scale according to the thermal motility of the individual atoms, determined for a tetrameric protein. (b) Tetramer assembled of two dimers with A/B (C/D) and A/C (B/D) interfaces.

1.1.2 Formation of the 'GFP'-Chromophore, *p*-HBI

The bioluminescence in GFP-like proteins is based on the post-translational cyclization of the tripeptide Ser65-Tyr66-Gly66 (numbering according to GFP). An attack of the protein backbone onto itself initiates the formation of a chromophore. Although rarely observed, this feature is not unique to GFP-like proteins but also occurs in enzymes such as histidine ammonia lyase (HAL) and the closely related phenylalanine ammonia lyase (PAL)[36,37]. In GFP-like proteins, the β-barrel structure enforces the chromophore formation by scaffolding the involved residues Ser65 and Gly67 in distinct positions[38]. The nucleophilic addition of the nitrogen of Gly67 to the carbonyl carbon of Ser65 results in the formation of a heterocyclic intermediate, which dehydrates in a subsequent reaction. The Tyr66 C_α-C_β bond of the emerging product is oxidized by molecular oxygen[39,40] (Figure 1.2). Supposedly, the chromophore formation involves several proton transfer reactions, which are mediated by the conserved amino acids Arg96 and Glu222 adjacent to the chromophore[41].

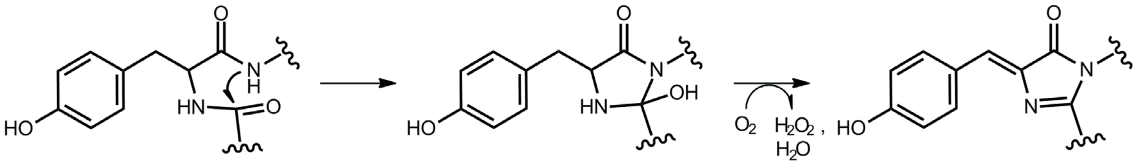

Figure 1.2: Formation of the *p*-HBI Chromophore. The pre-organized amino acids Ser65, Tyr66 and Gly67 form an intermediate state, which is oxidized by molecular oxygen into the mature *p*-HBI chromophore.

In GFP, the conjugated π-electron system includes the *p*-hydroxyphenyl moiety of Tyr66 and the imidazolinone ring formed by cyclization between Ser65 and Gly67. The two rings are aligned into a coplanar *cis* conformation with respect to the methylene bridge that links them into a 4-(*p*-hydroxybenzylidene)-5-imidazolinone (*p*-HBI).

1.1.3 Modifications of the *p*-HBI Chromophore

The emission color of FPs is influenced by the chromophore environment, which depends on the primary structure of the protein and the nature of the chromophore's π-electron system. In naturally occurring FPs, Tyr66 and Gly67 are strictly conserved, whereas a variety of amino acids is observed at position 65. The first non-green FPs were engineered by chromophore modifications through substitution of Tyr66 in GFP, yielding blue and cyan GFP variants[28] (Figure 1.3). Naturally occurring chromophore modifications result mostly in a red shift of the emission color. E.g., in DsRed ($\lambda_{\max} = 583\,\mathrm{nm}$)[42] or *eq*FP611 ($\lambda_{\max} = 611\,\mathrm{nm}$)[43], the conjugated π-electron system of the chromophore is extended by oxidation of the single bond between the amide nitrogen and the C_α of amino acid 65. The resulting acylimine group is in-plane with the *p*-HBI chromophore, extending it to a 2-imino-5-(4-hydroxybenzylidene)-imidazolinone (Figure 1.3). In some GFP-like proteins, the chromophore even adds a third heterocycle, e.g., in mOrange ($\lambda_{\max} = 562\,\mathrm{nm}$), which features an oxazole heterocycle formed by cyclization of Thr65[44], or in the yellow protein *z*FP538 ($\lambda_{\max} = 538\,\mathrm{nm}$), which forms the third heterocycle by ring closure of Lys65[45]. In the *as*FP595 variant Ala143Ser (AsRed, $\lambda_{\max} = 592\,\mathrm{nm}$), chromophore maturation induces backbone cleavage of the polypeptide chain, generating a carbonyl group that extends the chromophore π-electron system[46–49]. However, Figure 1.3 illustrates that the emission wavelength is not only determined by the nature of the chromophore but is also tuned by the surrounding amino acid residues and the hydrogen bonding network, which governs the chromophore protonation state, planarity and flexibility (Figure 1.1 a).

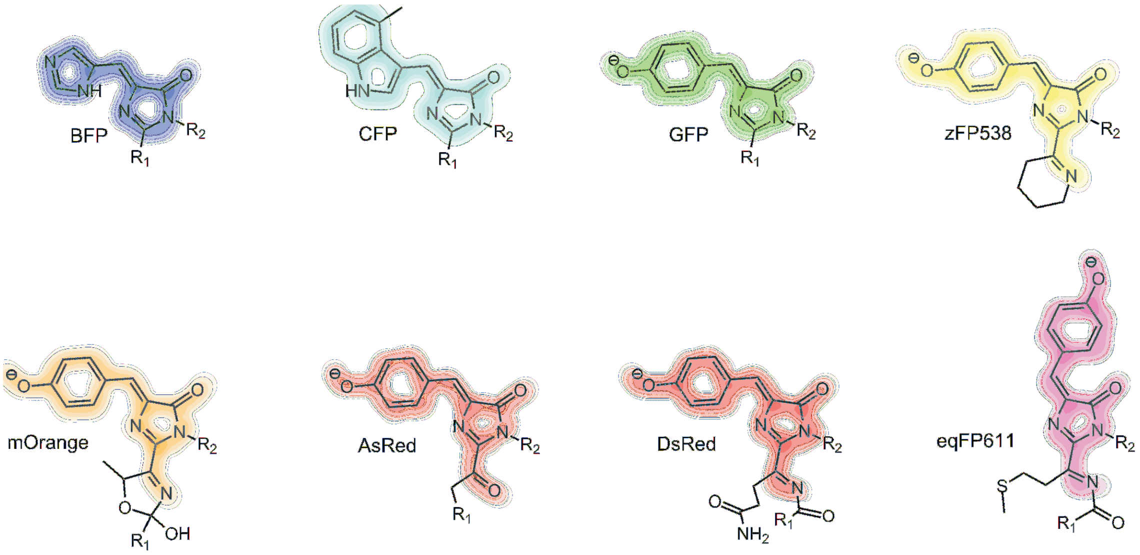

Figure 1.3: Variations of the Chromophore. Chromophores of differently colored FPs, as indicated by the labels next to the respective chromophore structures. The color shading indicates the emission color of the respective proteins.

1.1.4 Diversity Among GFP-like Proteins

The color diversity among even monomeric FPs, discovered or engineered over the last two decades, spans almost the whole visible spectrum. Since 2009, a violet protein named Sirius is available, featuring an emission peak at 424 nm[50]. The *av*GFP Tyr66His variant, EBFP, emits in the blue spectral range[51,52] and several improved variants have been presented[53–55]. Recently, a much brighter blue emitting FP, TagBFP, was introduced, which exhibits the original *p*-HBI chromophore[56]. FPs emitting in the cyan spectral range were mostly engineered from ECFP, a GFP variant featuring Trp66 in the chromophore tripeptide[57–60], although mTFP1 containing the *p*-HBI chromophore outclasses the cyan GFP variants in brightness[61]. The dominant emission color of naturally occurring FPs is green. EGFP, an early GFP variant introduced in 1995, already meets most technical requirements of a fluorescent marker protein[62]. Still, a variety of derivatives followed, which mainly feature improved maturation properties[56,62–65]. π-stacking of the *p*-HBI chromophore with Tyr203 induces a bathochromic shift of both the excitation and the emission spectra, resulting in yellow FPs[25] such as EYFP and its variants[66–69]. Orange and red emitting proteins are mainly derived from naturally occurring anthozoa FPs. Two orange proteins and their respective variants have been reported, namely mKO (monomeric Kusabira Orange)[70] and mOrange[71]. The orange-red spectral range is covered by TagRFP[72] and its variants[73]. mStrawberry[71] and mRuby[74] further extend this class. A monomeric protein developed from the *Montipora* stony coral, mKeima, exhibits the largest known Stokes shift among FPs, with a blue excitation peak at 440 nm and red emission peak at 620 nm[75,76]. mRaspberry[77], mPlum[77], mKate2[78] and mNeptune[79] are among the most red-shifted monomeric FPs, and emit at wavelengths beyond 630 nm. For FPs of higher oligomerization state, emission wavelengths up to 670 nm have been reported[80].

1.2 Photophysical Properties of GFP-like proteins

The photophysics of GFP-like proteins is rather complex. Emission intensity and wavelength, molecular brightness and photostability are influenced by a variety of external factors, e.g. pH, ionic strength, excitation wavelength and light intensity. These effects are based on subtle modifications in the chromophore chemistry that occur in response to modifications in the protein vicinity or in response to irradiation.

1.2.1 Spectroscopic Properties of the Chromophore

The absorption spectrum of the *p*-HBI chromophore in GFP-like proteins usually features two bands in the visible range of the spectrum, termed A and B bands, with the A band being blue-shifted relative to the B Band. Excitation within the B band typically yields bright fluorescence, with Stokes shifts ranging from 10 to more than 100 nm[81] while excitation within the A band may cause two different phenomena. Here, excitation either yields weak fluorescence, with Stokes shifts of about 50 - 100 nm, or a bright signal, with an emission maximum similar to that observed for excitation within the B band. Depending on the local environment in the respective protein, the spectroscopic properties of the chromophore vary significantly. For example, the *av*GFP absorption spectrum is dominated by the A band peaking at 395 nm under physiological conditions. The minor B band is centered on 475 nm, and excitation within this band yields maximal fluorescence at 503 nm ($\phi_{\mathrm{fl}} = 0.79$). Only two mutations, namely Phe64Leu and Ser65Thr, sufficed to gain an enhanced GFP variant, EGFP, which populates preferentially the B band and, therefore, shows increased fluorescence intensity and a shift of the excitation and emission maxima to 489/509 nm, respectively[62].

1.2.2 pH Sensitivity of the Chromophore

Several studies using X-ray crystallography[25,82] and FTIR spectroscopy[83] have shown that the hydroxyphenyl moiety of the *p*-HBI chromophore alternates between the phenol and the phenolate states. In FPs, different protonation states of the chromophore are indicated by the ratio between the A and B band amplitudes that is often observed to vary with pH (Figure 1.4). The varying ratio allows the assignment of the A band to the neutral phenol state and of the B band to the anionic phenolate state of the chromophore[28,84,85].

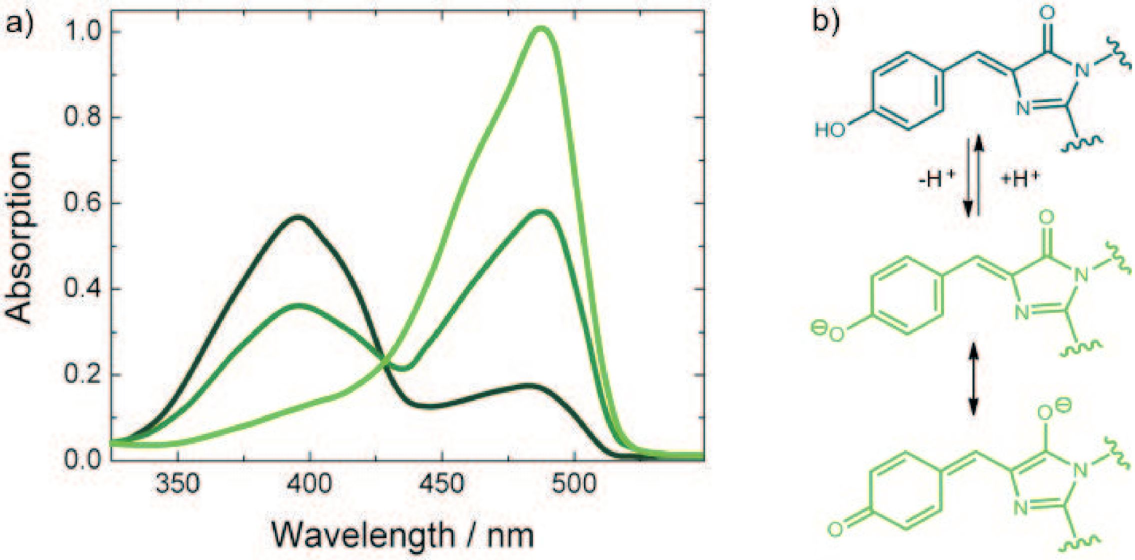

Figure 1.4: pH sensitivity of EGFP. (a) Absorption spectra of EGFP at pH 4.5 (dark green), pH 6.0 (olive) and pH 9 (green)[86]. (b) Protonation equilibrium of the *p*-HBI chromophore. The neutral chromophore (olive) deprotonates, yielding the anionic form (green), depicted in its mesomeric structures.

The pH response of the chromophore may differ significantly depending on the chromophore vicinity. For some FPs, such as *av*GFP[84,85] and *as*FP499[87], the ratio between neutral and anionic chromophores remains essentially fixed over a wide pH range. For other FPs, such as EGFP, the transition between the neutral and the anionic state follows a simple Henderson-Hasselbalch relation as expected for a two-state transition[88]. However, complex transitions involving multiple pK_a values are not uncommon[89,90] (Fuchs *et al.* and Gayda *et al.*, unpublished). The apparent midpoints of these transitions usually range from 4 to 7[81]. Detailed analyses of multi-step transitions suggest that the deprotonation of the chromophore is coupled to the deprotonation of a neighboring amino acid. Scharnagel *et al.* illustrated this type of interaction between two different amino acids in a four-state model[89]. This model was extended by Nienhaus *et al.* to explain the protonation behavior of the chromophore of *cm*FP512 in interaction with a near-by residue[90].

According to this model, the relative populations of the neutral (C^H) and anionic chromophore (C^-) are directly coupled to the protonation state of the respective adjacent group and vice versa, e.g., a neighboring amino acid $X^- + H^+ \rightleftharpoons X^H$. Thus, four species have to be considered; $C^H X^H$, $C^H X^-$, $C^- X^H$ and $C^- X^-$, with their relative populations being subject to four different equilibria (Figure 1.5). A change in the protonation state of the residue X leads to a shift of the chromophore absorption band.

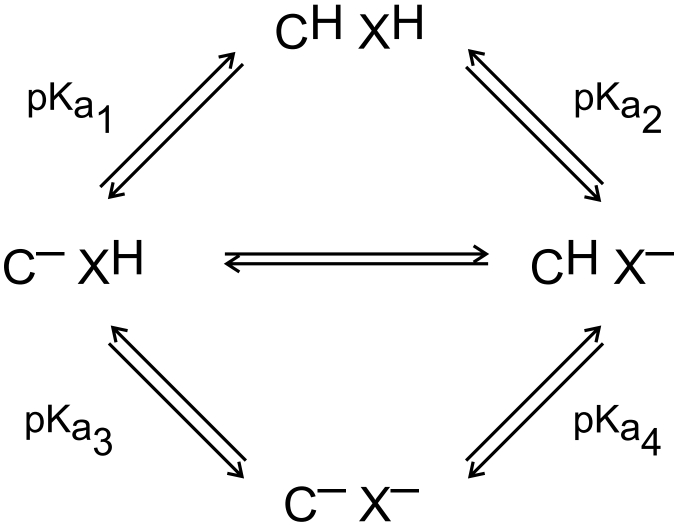

Figure 1.5: Model of chromophore protonation energetically coupled to an adjacent residue. C^H / C^- represent the neutral and anionic forms of the chromophore next to the interacting residue X^H / X^- in its protonated and deprotonated states, respectively[90].

1.2.3 Excited State Proton Transfer

Previous studies suggested that the acidity of the chromophore increases upon excitation[91,92], which is based on the withdrawal of electrons from the hydroxyphenyl moiety and redistribution to the methylene and imidazolinone groups (Figure 1.6). In the presence of a suitable proton acceptor, this might result in deprotonation (excited-state proton transfer (ESPT)), yielding a fluorescent anionic chromophore.

Actually, the emission of GFP induced by a 395-nm flash temporally shifts from 460 nm to 508 nm within 10 ps, as was observed in picosecond spectroscopy studies[85]. The kinetics of this shift is significantly slowed by cooling the sample to 77 K or by deuterium substitution, which confirms the hypothesis of ESPT[85]. However, excitation within the neutral chromophore band (A) and the anionic chromophore band (B) results in different emission maxima (508/503 nm), which suggests that the local environment of the neutral chromophore does not adapt to the changed electrostatic conditions upon chromophore deprotonation during the excited state lifetime.

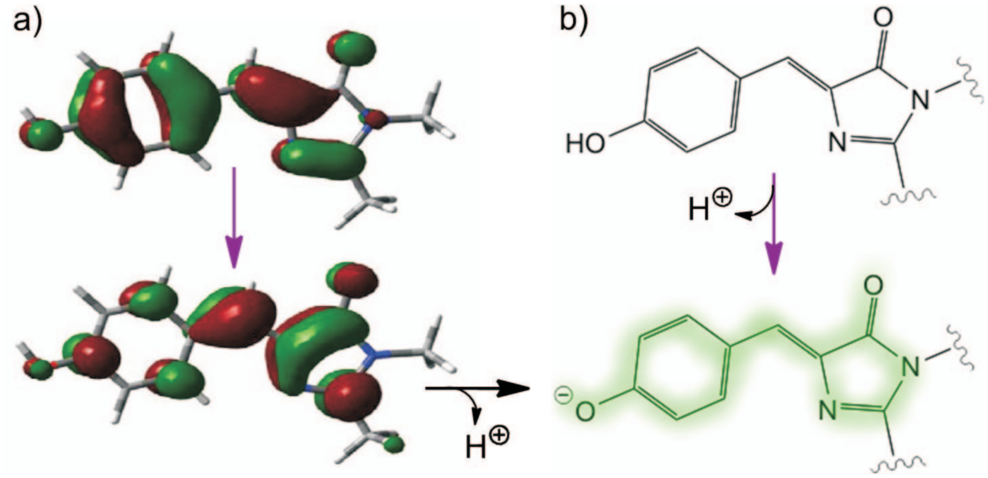

Figure 1.6: Excited State Proton Transfer (a) The illustration of the orbital electron distribution in HOMO and LUMO of the neutral *p*-HBI chromophore, reproduced with kind permission from quantum mechanics calculations of M. Lelimousin (IBS, Grenoble, France). (b) Due to the electron redistribution upon excitation of the neutral chromophore, the acidity of the hydroxyphenyl moiety increases, resulting in deprotonation to a fluorescent anionic chromophore species.

1.2.4 Blinking

Continuous illumination of a GFP sample in an ensemble measurement results in an exponential decay of the emission intensity, due to photobleaching. However, on a single molecule level, individual GFP molecules display short bursts of fluorescence turning up in between dark periods[93–95] (Figure 1.7).

The on-times, describing the duration of these fluorescence bursts, are apparently pH independent, while they increase significantly with decreasing excitation power. This behavior demonstrates that the on-to-off transition is a photoinduced process

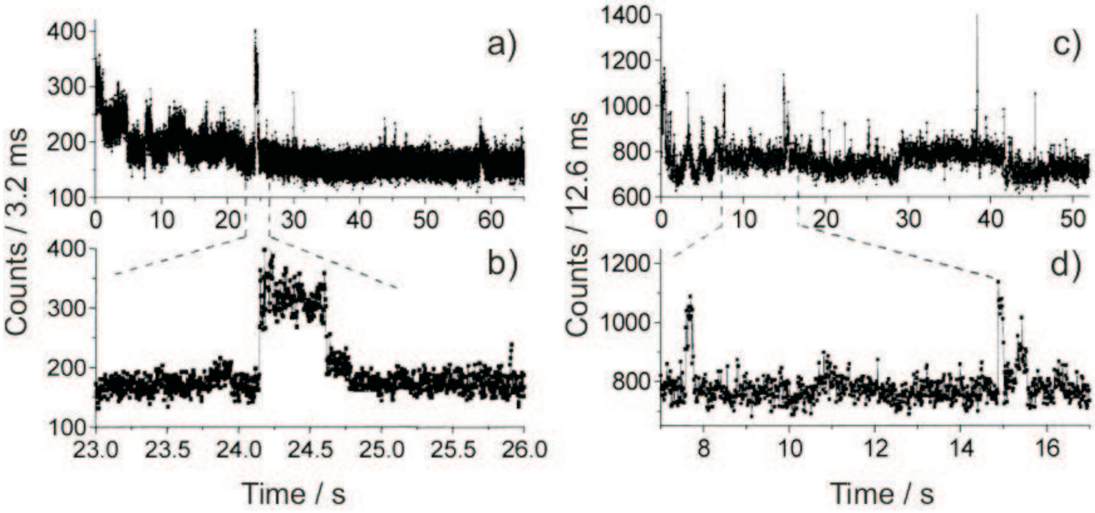

Figure 1.7: Single molecule fluorescence trajectories of GFP S65T. Fluorescence trajectories are shown for two different S65T molecules (a/b) and (c/d). Panels (a) and (c) show the total fluorescence time trace with occasional fluorescence bursts over otherwise dark background. (b) and (d) depict enlarged fluorescence bursts, respectively. The figure is reproduced from Garcia-Paraja *et al.*[95].

and not a thermally induced switching of the chromophore protonation state[94]. The dark periods subdivide into short- and long-lasting off-states[93], which are independent of the excitation intensity[95]. The intensity independence implies that they thermally relax to the fluorescent on-state. The chemical nature of these dark states is not conclusively clarified. Studies on the GFP mutant Glu222Gln have indicated that the short-lived dark state corresponds to the chromophore triplet state, while the long-lasting dark state corresponds to a neutral GFP chromophore[96]. 405-nm light, which is near to the absorption maximum of the neutral chromophore, activates the transition of the long-lasting dark state to the initial fluorescent on-state[93], also indicating an involvement of a neutral species. Time-resolved fluorescence and polarization anisotropy measurements of EGFP reveal that the interaction of the chromophore with the surrounding hydrogen-bonding network is pH dependent. The pH dependence is reflected in the increasing fraction of blinking molecules within the EGFP population upon decreasing pH values, characterized by a pK_a of ~ 5.8. Liu and coworker suggested that structural changes may trigger isomerization, either involving Thr203 or the chromophore[97]. A similar origin for the fluorescence quenching in the long-lasting dark state was suggested by quantum-chemical studies of Weber and coworkers[98]. However, in addition to photoisomerization, electron transfer reactions and proton rearrangements should be considered.

1.2.5 Shift in Emission Color

In 1997, GFP was found to shift its emission wavelength from green to red upon illumination with violet light. However, photoconversion occurred only under low oxygen concentrations, limiting the practical use of this property to anaerobic organisms[99] (Figure 1.8). Although hitherto not generally observed in conventional FPs, a photoinduced shift of the emission wavelength might occur regularly in FPs. Kremers and coworkers identified photoconversion in 8 of 12 orange and red FPs[100]. Among those were the red FPs Katushka, mKate and HcRed, which photoconverted to a green fluorescent state upon illumination with violet or green light. A similar photoconversion was observed for mPlum and mRaspberry, although both showed only a 10-nm shift. In mOrange, a bathochromic shift was observed upon intense 561-nm illumination. This protein photoconverts to a far-red species, featuring excitation and emission maxima at $\sim$610 nm and $\sim$640 nm, respectively. However, their practical use is limited by moderate increase of signal upon photoconversion compared to the initial signal in the detection window. This property is commonly described by the contrast, characterizing the ratio of the difference between the brightness in photoconverted and initial state to the sum of the brightness in both states.

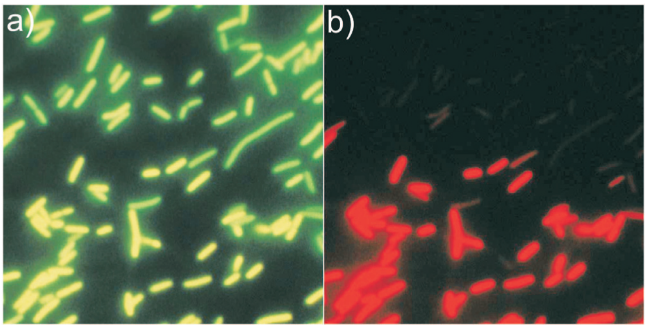

Figure 1.8: Green-to-red photoconversion of GFP. GFP-expressing *E.coli* cells imaged through fluorescein (a) and rhodamine (b) filter sets. The lower halves of the images were exposed to 475-495-nm light, photoconverting GFP to a red emitting state. The picture is copied from Elowitz *et al.*[99].

1.3 Photoactivatable Fluorescent Proteins

Considering the findings already discussed, a strict differentiation of GFP-like proteins into photoactivatable and non-photoactivatable might be ambiguous. However, in the last decade, several new FPs were discovered and engineered that achieve contrast ratios of up to several thousand upon photoactivation and, by far, outperform the previously described proteins[81] and are, therefore, referred to as *p*hoto*a*ctivatable *f*luorescent *p*roteins, PAFPs. The fluorescence properties of these proteins can be controlled by irradiation with light of a particular wavelength. The induced photoreactions can be classified as photoconversion (irreversible) and photoswitching (reversible) reactions[20]. Photoconversion causes a permanent increase in the fluorescence intensity at a particular wavelength. Photoswitching denotes the reversible alteration of the fluorescence intensity or color in response to illumination with light of particular wavelengths.

1.3.1 Irreversible Photoconversion

Irreversible photoconversion implicates changes in the covalent bond system, either involving the chromophore or an amino acid in its vicinity. The alteration of covalent bonds leads to a conversion of the chromophore π-electron system and, therefore, modifies its absorption and emission properties. Macroscopically, two modes of photoconversion can be observed, (i) conversion from a dark, non-fluorescent to a bright, fluorescent state and (ii) conversion from a bright fluorescent state to another one with a different emission color[81]. This classification does not hold for the underlying photoactivation mechanism, which varies significantly depending on the proteins the PAFPs were originally derived from. In the following, the PAFPs are sorted into three subgroups, with respect to the photoactivation mechanism.

Photoconversion due to Decarboxylation of Glu222

In *av*GFP, excitation of the neutral chromophore with violet light induces electron transfer from Glu222 to the chromophore, which triggers decarboxylation of Glu222[101,102]. Without the carboxyl moiety of Glu222, the hydrogen bonding network around the chromophore rearranges, leading to a decrease of the chromophore $\mathrm{p}K_a$[28,85,103] and, hence, to an increase in the fraction of anionic, fluorescent chromophores (Figure 1.9). However, *av*GFP shows substantial fluorescence even before photoactivation, due to the initial fraction of anionic chromophores. Thus, photoinduced enhancement of the anionic chromophore population generates only a $\sim$three-fold fluorescence increase, which makes *av*GFP unsuitable for practical applications as a PAFP[28,104], featuring a similar photoactivation mechanism. Still, several photoactivatable *av*GFP variants have been engineered based on this observation. Among those, PA-GFP yields a $\sim$100-fold gain in emission intensity upon 488-nm illumination[8] (Figure 1.9). PS-CFP and its variants convert from a cyan emitting state to a green one and thereby achieve a ∼1,500-fold cyan-to-green contrast increase[105].

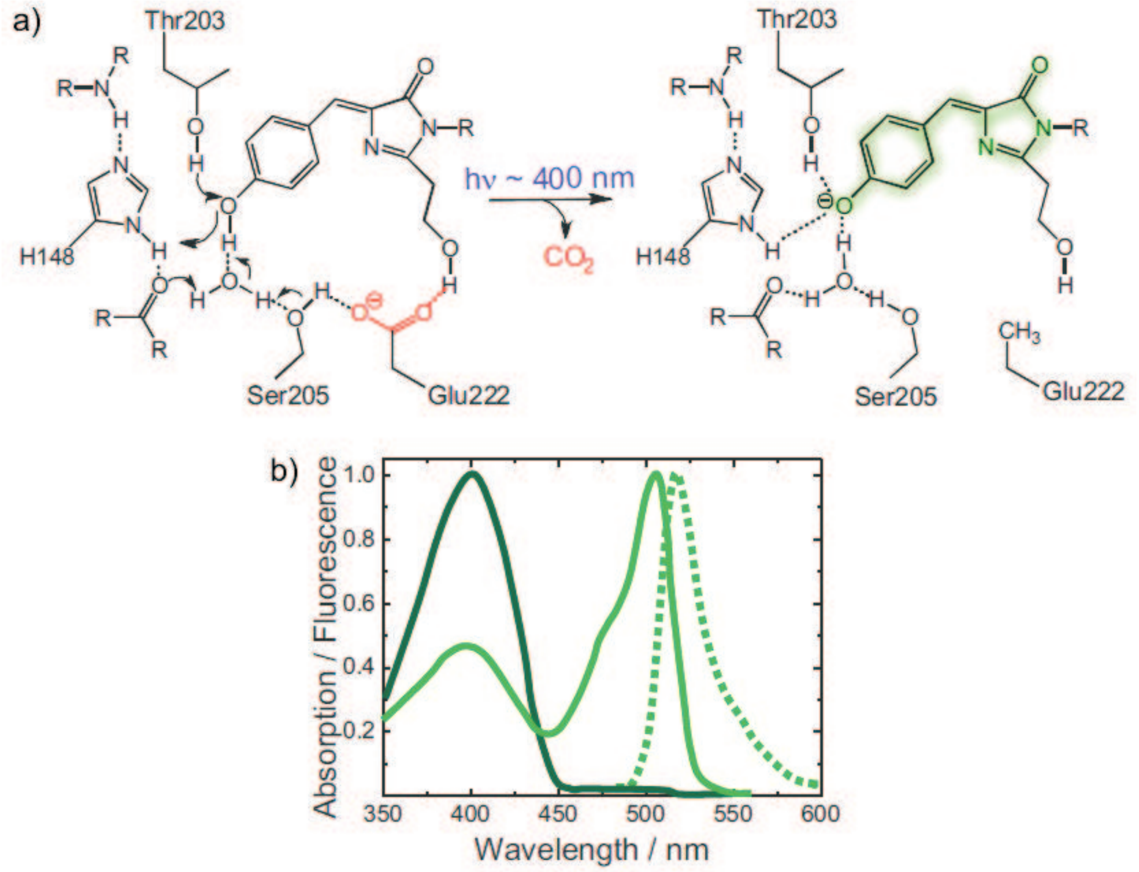
a)
Thr203
H148
Ser205
Glu222
hν ~ 400 nm
CO2
CH3
b)
Absorption / Fluorescence
0.2
0.4
0.6
0.8
1.0
350
400
450
500
550
600
Wavelength / nm

Figure 1.9: Photoactivation in PA-GFP. (a) Reorientation of the hydrogen bonding network surrounding the chromophore upon photoinduced decarboxylation of Glu212. (b) Absorption spectra before (dark green) and after (light green) photoactivation are depicted with the emission spectrum of activated of PA-GFP (dotted). All spectra have been scaled to the same amplitudes. The figure is reproduced from Gayda *et al.*[81].

Photoconversion due to Oxidation of Tyr66

Proteins of this group form their chromophore from the tripeptide Met65-Tyr66-Gly67. They irreversibly photoconvert from a dark to a red-emitting state after illumination with violet light. Absorption spectra of the initial dark-state chromophore suggest that it is similar for PA-RFP and PAmCherry. This dark state was identified as a N-[(E)-(5-hydroxy-1H-imidazol-2-yl)methylidene]acetamide[106]. It features an N-acylimine group conjugated with the cyclized 65-67 tripeptide. The C_α-C_β bond of the Tyr66 side chain is not oxidized, thus the hydroxyphenyl moiety of Try66 does not contribute to the π-electron system of the dark-state chromophore[106]. Photoexcitation with violet light induces oxidation of this C_α-C_β bond, which is possibly mediated by the concurrently observed decarboxylation of Glu222 (numbering according to GFP). The resulting methylene bridge extends the chromophore π-electron system toward the hydroxyphenyl moiety, forming a bright red emitting chromophore.

Photoactivation in PATagRFP involves an additional photochemical process prior to the previously described reaction[107]. Subach and coworkers suggested that the initial dark state of PATagRFP is an aromatic α-enolate, an early stage intermediate of chromophore maturation[41]. The additional photoactivation step may establish a chromophore similar to the initial dark-state chromophore in PAmCherry and PA-RFP[107].

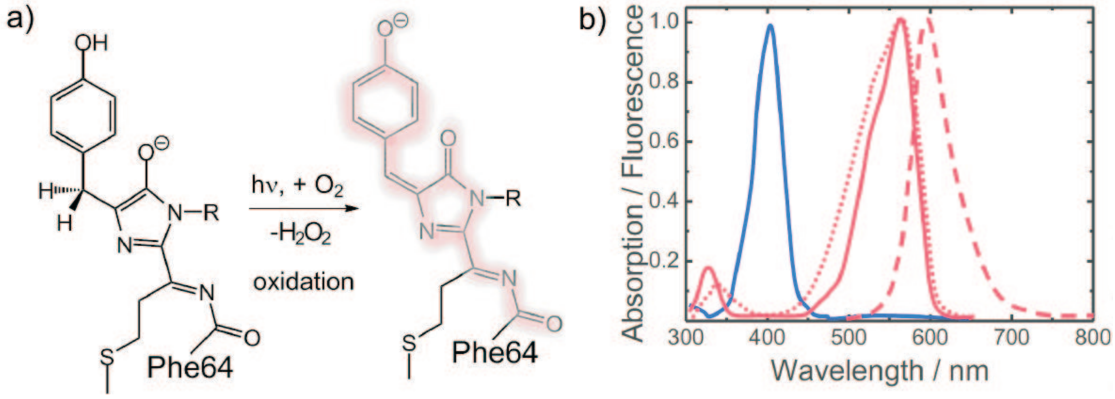

Figure 1.10: Photoactivation in PAmCherry. (a) Extension of the chromophore π-electron system is triggered by the photoinduced oxidation of the C_α-C_β bond of the Tyr66 side chain. (b) Absorption spectra (solid) before (blue) and after (red) photoactivation are depicted with the emission (dashed) and excitation spectrum (dotted) of activated of PAmCherry. All spectra have been scaled to the same amplitudes.The figure is reproduced from Gayda *et al.*[81].

Photoconversion due to β-Elimination within the Protein Backbone

All hitherto known naturally occurring photoconvertible FPs feature green-to-red transitions upon illumination. Proteins of this group feature the same chromophore-forming tripeptide His62-Tyr63-Gly64 (numbering according to EosFP). The replacement of His62 by any other amino acid resulted in a loss of the photoconversion ability[108,109], indicating that His62 is crucial for the underlying photoconversion mechanism. The red shift in excitation and emission upon illumination with violet light is due to the addition of covalent bonds to the conjugated π-electron system of the chromophore. These additional covalent bonds are formed by a β-elimination reaction between the amide nitrogen of Phe61 and the C_α of His62, establishing a double bond between the C_α and C_β of the His62 side chain[108,109] (Fig. 1.11) and, thereby, creating the 2-[(1E)-2-(5-imidazolyl)ethenyl]-4-(*p*-hydroxybenzylidene)-5-imidazolinone chromophore. The protein backbone between His62 and Phe61 is cleaved in the process. Several suggestions about possible photoconversion mechanisms have been put forward. They all agree in that the neutral chromophore is the reactive species. ESPT from the hydroxyphenyl moiety of the chromophore to the His62 might produce a doubly protonated His62[108,109]. To circumvent the high energy expense of such an ESPT, Li *et al.* proposed a stepwise ground state proton transfer from the His62 C_α to the His62 N_δ, based on quantum-chemical calculations on Kaede[110]. The doubly protonated His62 may trigger the β-elimination promoting backbone cleavage. Nienhaus *et al.* suggested Glu222[109] as the proton acceptor in the β-elimination reaction, while Hayashi *et al.* conjectured a nearby water molecule, which disappears upon photoconversion[111,109]. Lelimousin *et al.* proposed a mechanism, in which the reactive neutral chromophore remains protonated. Instead, ESPT from His62 to Phe61 triggers cleavage of the peptide bond. Their calculations also indicated two sequential intersystem crossings, which could account for the low quantum efficiency of the photoconversion reaction[112].

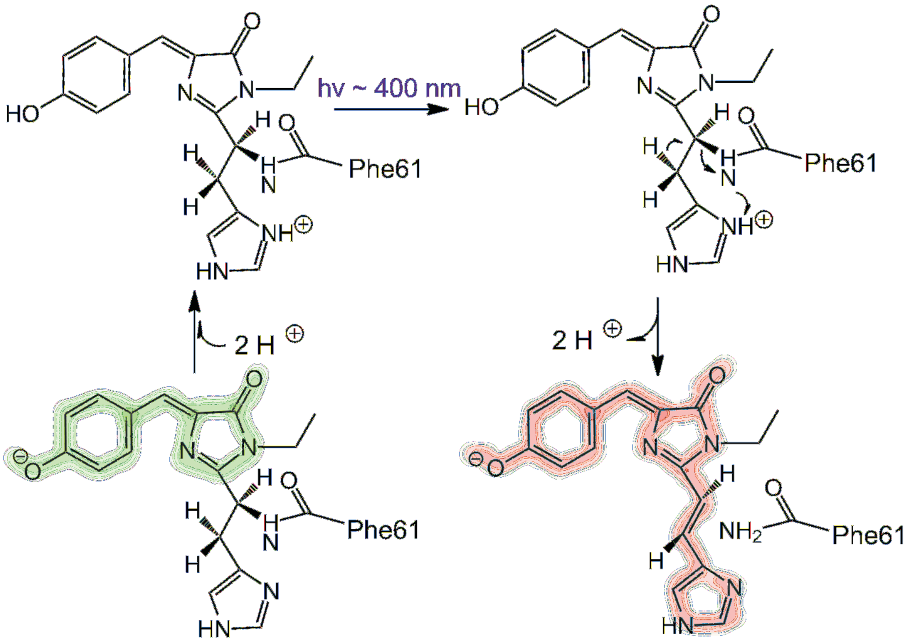

Figure 1.11: Photoconversion in EosFP. Extension of the chromophore π-electron system is triggered by the photoinduced β-elimination between the C_α and C_β of the His62 side chain. The figure is reproduced from Gayda *et al.*[81].

This kind of photoactivation is observed in Dendra[113], KikGr[114], Kaede[115] and EosFP[116]. While Kaede and EosFP are photophysically very similar, Dendra presents an exception. Its high pK_a value and, thus, high fraction of neutral chromophores at physiological pH, allows for more efficient photoconversion with blue light by exciting the neutral chromophore in its long-wavelength spectral wing. KikGR is the only engineered protein among the green-to-red photoactivatable FPs. Its predecessor is a green protein isolated from *Favia favus*, which obtained the photoconversion ability upon implementing His62 into the chromophore forming tripeptide and semi-rational mutagenesis of several amino acids in the chromophore vicinity[114].

EosFP

EosFP is the most utilized protein among the green-to-red photoconvertible PAFPs. It was originally isolated from the stony coral *Lobophyllia hemprichii*[116], which varies in color in response to its environmental conditions (Figure 1.12 a).

Naturally occurring EosFP associates into a tetramer, containing four identical protomers. The anionic green chromophore features maximum excitation and emis-

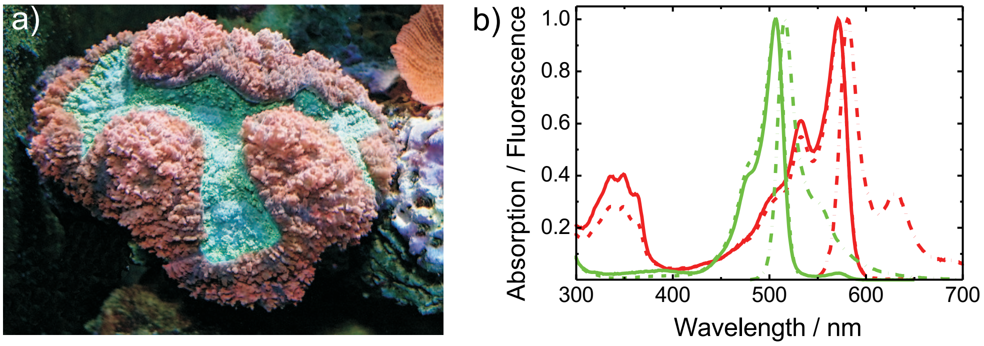

Figure 1.12: Natural occurrence and spectral properties of EosFP. (a) The coral *Lobophyllia hemprichii* expressing EosFP. The picture is reproduced with courtesy of Heinz Mahler (www.reefdreams.de). (b) Absorption (solid), excitation (dotted) and emission spectra (dashed-dotted) of EosFP before (green) and after (red) photoconversion, scaled to the same maximal amplitudes.

sion at 506 and 516 nm, respectively (ε (506 nm) = 72,000 $\mathrm{M^{-1}\,cm^{-1}}$, $\phi_{fl} = 0.70 \pm 0.02$)[116] (Figure 1.12 b). It protonates with a pK_a of 5.8 ± 0.1, producing a neutral chromophore that fluoresces only marginally. Its excitation with intense ~400 nm-light induces photoconversion to the red form, whose anionic state shows maximum excitation and emission at 571 and 581 nm, respectively (ε (571 nm) = 41,000 $\mathrm{M^{-1}\,cm^{-1}}$, $\phi_{fl} = 0.55 \pm 0.03$)[116]. Spectra of the red anionic chromophore of EosFP reveal pronounced vibronic sidebands at 533 and 629 nm in excitation and emission, respectively. An additional band in the violet spectral range corresponds to a higher electronic state.

In the X-ray structure, the green and red chromophores adopt an almost perfectly planar *cis* conformation[109] (Figure 1.13).

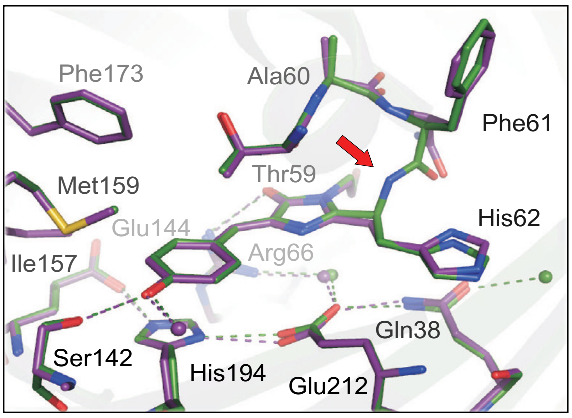

Figure 1.13: Photoconversion in EosFP. Superposition of the crystal structures of the green (PDB code: 1ZUX) and the red EosFP (PDB code: 2BTJ), illustrating backbone cleavage between His62 and Phe61 (red arrow).

The structure of the red form of EosFP differs from the green one only by (i) the backbone cleavage at Phe61, due to photoconversion, and (ii) the absence of a water molecule, which was previously adjacent to His62 (Figure 1.13)[109].

Recently, EosFP has become available as a monomer (mEos2[117], mEosFP-*thermo*[118]) and pseudomonomer (tdEosFP). Due to its tandem-dimer character, the latter construct features enhanced brightness and photostability[34,117].

1.3.2 Reversible Photoactivation - Photoswitching

A reversible transition between a bright and a dark state was first observed for *av*GFP and termed blinking[93] (Section 1.2.4). Reversibly photoactivatable FPs show similar behavior. However, the transition between a bright on-state and a dark off-state is visible even in the bulk. These proteins can be switched repeatedly by light of particular wavelengths and, therefore, are termed photoswitchable FPs. The transition is structurally based on a *cis*-*trans* isomerization of the chromophore and conformational rearrangements of amino acids in its vicinity[119–124]. Usually, photoisomerization is accompanied by a change in the chromophore protonation state, its planarity and its interaction with the β-barrel matrix[125,126].

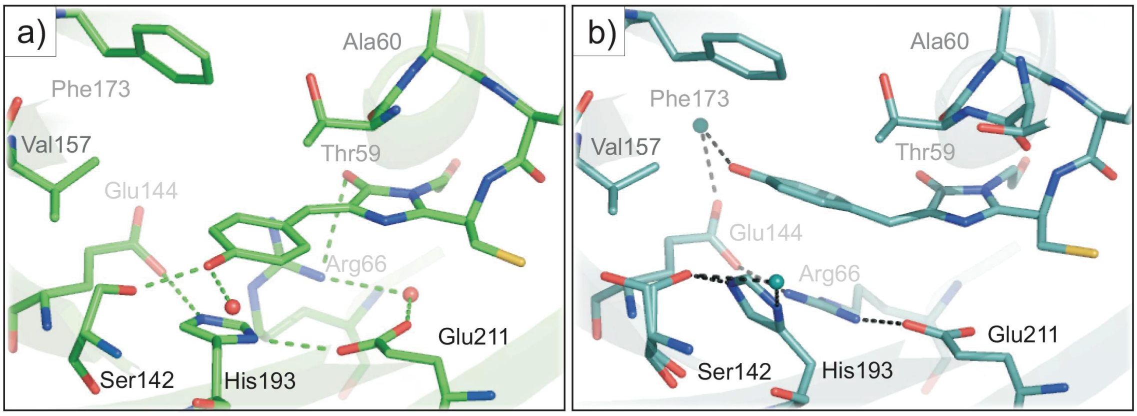

Figure 1.14: Reversible photoswitching in Dronpa. Superposition of the on- (PDB code: 2IE2) and off-state structures of Dronpa (PDB code: 2POX). Similar structural rearrangements in the chromophore vicinity have also been observed in other photoswitchable FPs[121,124,127,128].

Energetically, the two isomers are similarly stabilized in the absence of a chromophore matrix[47], with the *cis* conformation only ~4-13 kJ mol^{-1} lower in free energy than the *trans* chromophore[129,92]. *Ab initio* multiple spawning (AIMS) simulations indicate that stabilization of a particular isomer is not an intrinsic property of the chromophore but rather induced by the protein matrix[92]. For example, in mKeima, pH changes shift the equilibrium between the *cis* and the *trans* chromophore conformations, due to the pH-dependent rearrangements of the hydrogen bonding network in the chromophore vicinity[130]. In thermal equilibrium at physiological pH and temperature, the chromophore adopts the *cis* conformation in most photoswitchable FPs and the *trans* conformer is accessible only by photoswitching. Typically, the fluorescent on-state exhibits the *cis* conformer, whereas in the dark state the *trans* conformer is present. However, the chromophore conformation does not necessarily determine the fluorescence properties. For instance, eqFP611 features a brightly fluorescent *trans* chromophore ($\phi_{\text{fl}} = 0.45$)[43]. In fact, the fluorescence properties are directly related to the protein matrix surrounding the chromophore. The two isomers are exposed to different scaffolds and hydrogen bonding networks, causing modifications in coplanarity and pK_a, which account for the observed change of the chromophore protonation state upon isomerization. The direction of the photoswitching while exciting fluorescence defines the photoswitching mode. If the wavelength exciting the fluorescence concurrently induces off switching, i.e. populates the non-fluorescent dark state, the protein exhibits a 'negative switching mode'. If the wavelength exciting fluorescence concurrently induces on switching, i.e. populates the fluorescent on-state, the protein exhibits a 'positive switching mode'. When kept in the dark, the chromophore relaxes thermally into the energetically more favored conformation. This process can be accelerated by photoexcitation of the dark state chromophore.

Negative Switchers

The on-state in negatively switching FPs features a lower pK_a than the off-state. Thus, photoswitching of the anionic on-state results in a neutral dark state. The 'prototype' of a negative switcher is Dronpa. This green emitting protein was generated from the tetramer 22G, which was isolated from the stony coral Pectiniidae[7]. Its name accounts for its ability to vanish ('Dron' being a ninja term for vanishing) and reappear ('pa' for *p*hoto*a*ctivation). Irradiation with blue light decreases its fluorescence significantly, transferring the protein to a metastable state from which it takes hours to thermally recover to the on-state. The process is accelerated by irradiation with violet light. This on-off cycling can be repeated ~100 × with only 25 % loss in the original fluorescence[7]. In recent years, Dronpa variants featuring faster switching kinetics[127], shifted spectral properties and reverse switching were presented[131] (Figure 1.15).

The negatively switching FPs rsCherryRev and rsTagRFP fluoresce in the red spectral range. Blue light converts the proteins into the on-state, while green excitation results in red fluorescence and turns the proteins off[132,133].

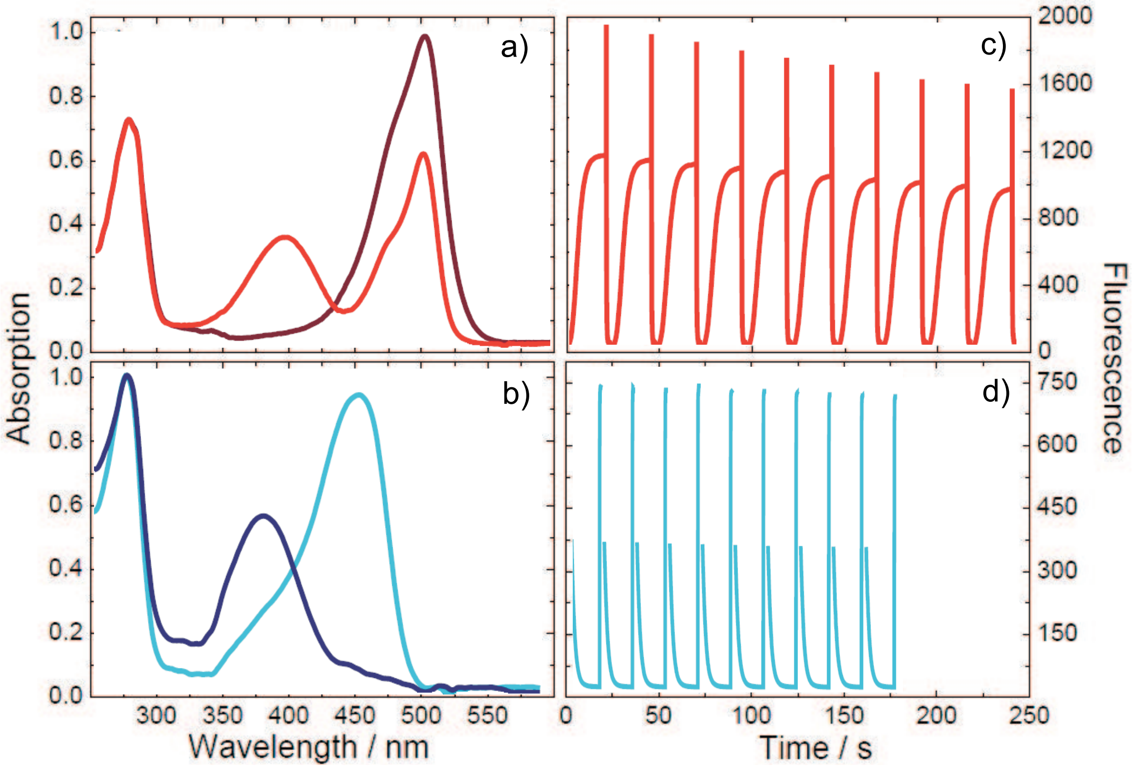

Figure 1.15: Photoswitching of Dronpa variants featuring a positive and a negative switching mode. Absorption spectra of (a) Padron and (b) bsDronpa in their on- (light red / blue) and off-states (dark red / blue), respectively. Photoswitching cycles were depicted in (c) for Padron featuring a positive switching mode and in (d) for bsDronpa featuring a negative switching mode. The images were redrawn from data by Andresen *et al.*[131].

Positive Switchers

The off-state chromophore of positively switching FPs is almost completely deprotonated at physiological pH. Photoswitching results in isomerization to the on-state, which features a lower pK_a value and is therefore partially protonated. Thus, the protonation state alone is not the crucial requirement for photoswitching.

The only green emitting photoswitchable FP featuring a positive switching mode is the Dronpa variant Padron[131]. In thermal equilibrium, Padron is essentially non-fluorescent. Irradiation with blue light converts the protein to the fluorescent on-state. The on-state is very stable and relaxes only slowly back to the off-state, with a half-time of $\sim 42\,\mathrm{h}$. The process is accelerated by irradiation with violet light.

In the orange-to-red spectral range, two photoswitchable FPs are known as yet. One is the naturally occurring asFP595 (= asulCP), the first PA-FP discovered[46]. This protein is non-fluorescent in thermal equilibrium (off-state) but converts into a fluorescent state upon illumination (on-state). The relative populations of its on- and off-states can be toggled by illumination with green (on switching) and blue light (off switching)[46]. The other protein is rsCherry, an mCherry variant, which is spectroscopically similar to the previously described rsCherryrev. Like asFP595, rsCherry adopts the off-state in thermal equilibrium and can be converted to the fluorescent on-state upon illumination. Here, the transition from dark to bright or from bright to dark is achieved by illumination with yellow and blue light, respectively[132].

1.3.3 PAFPs Showing Reversible AND Irreversible Photoactivation

In KFP, the photoactivation mode depends on the intensity and the duration of the activating light. Low intensity photoactivation ($\sim 1\,\mathrm{W\,cm^{-2}}$, 2 min) reversibly switches the protein into a fluorescent on-state, which thermally relaxes to a non-fluorescent off-state over tens of seconds. High intensity photoactivation ($\sim 20\,\mathrm{W\,cm^{-2}}$, 20 min) converts the non-fluorescent off-state irreversibly to the fluorescent on-state, yielding a 30-fold increase in fluorescence[123].

In the following, we will introduce a new PAFP of this class, IrisFP, which shows much more efficient reversible and irreversible photoactivation than KFP. It is the first protein that irreversibly converts its emission color from green to red and, within each state, reversibly switches between a bright and a dark state (Chapter 4)[120].

1.4 FPs in Superresolution Live-Cell Imaging

Studying cell physiology and cell dynamics requires observation of living cells. Most imaging approaches like scanning probe, electron and X-ray microscopy are associated with high cytotoxicity of the sample preparation or of the imaging process itself. Live-cell imaging is therefore preferentially performed by light microscopy, which is a minimally invasive imaging technique, interfering only marginally with the living system. For this imaging approach, the genetically encodable FPs are the most suitable probes, because of the accurate and non-invasive labeling. However, in the conventional light microscopy methods all FPs are detected at once. Each of those molecules is a point light source, which emits homogeneously in all spatial directions. Due to diffraction, the intensity shape of this emission corresponds to an Airy disc shaped point spread function (PSF) with its width determined by the wavelength of the emitted light. With rising FP density, the PSFs of the individual FPs increasingly overlap until they cannot be distinguished anymore, which defines the diffraction limit. Ernst Abbe recognized this fact in 1873 and quantified the relation between spatial resolution, wavelength and optical setup in an equation, called Abbe's law. Abbe's law defines the diffraction barrier with $d \approx \lambda/2 \approx 200\,\mathrm{nm}$ for visible light. Among other things, the continuing extension of the FP toolbox with proteins featuring enhanced or new properties promoted the ongoing advances in light microscopy methods[134,12] and recently led to the introduction of a new imaging approach, termed *p*hoto*a*ctivation *l*ocalization *m*icroscopy (PALM)[9,10]. This method relies on the off-to-on transition of individual molecules, which are photoactivated randomly in space. During data acquisition, the FPs are mainly dark in the selected detection window. Sparse photoactivation renders single molecules to a fluorescent state, which photoconvert to a dark state again, induced by the excitation light during imaging (readout). Thus, repeated photoactivation and readout presents ever-different subsets of FPs in the sample, each detected in an individual image frame. As adjacent molecules remain in the dark state, the position of the individual FPs can be determined precisely by calculating the center of gravity of its PSF[135]. The final image is a reconstructed density map of these calculated positions of the fluorescent molecules. The spatial resolution of this image depends on the localization precision of the center of gravity, plotted as the radius around the calculated coordinate. The localization precision can be much smaller than the width of the corresponding PSF, governing the spatial resolution in images achieved by conventional light microscopy methods (Figure 1.16). A higher average number of emitted photons per molecule improves the localization precision and, therefore, the spatial resolution. However, this number varies significantly among PAFPs. While molecules of the brightest PAFP, tdEosFP, typically emit up to 2,600 photons[136], monomeric PAFPs emit only a few hundred[118].

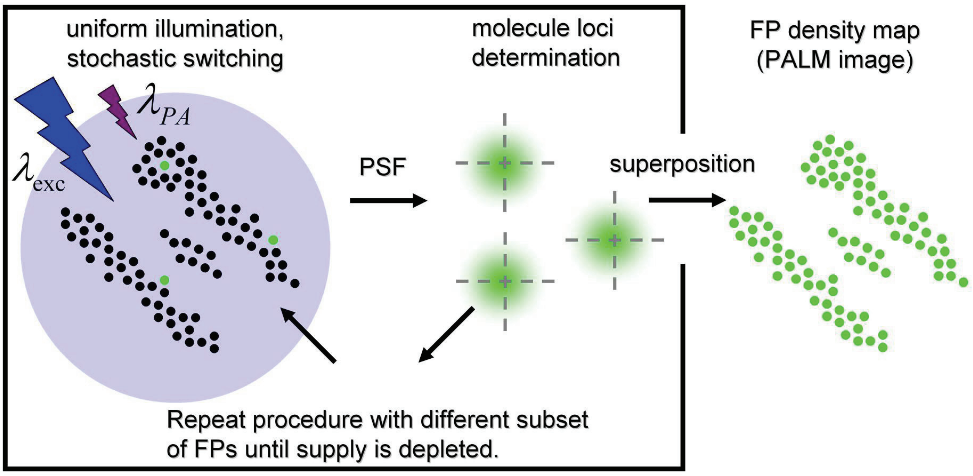
uniform illumination,
stochastic switching
λ_{PA}
λ_{exc}
PSF
molecule loci
determination
superposition
FP density map
(PALM image)
Repeat procedure with different subset
of FPs until supply is depleted.

Figure 1.16: Schematic illustration of the principle of PALM[118].

Part II

Materials and Methods

Chapter 2

Molecular Biology

2.1 Mutagenesis

Mutagenesis was used as a tool to selectively or randomly exchange individual amino acids. All protein variants described below originate from mEosFP Ala69Val (mEosFP*thermo*[118]). The resulting genes were commercially sequenced by the Eurofins MWG GmbH (Ebersberg, Germany) or the GATC-Biotech AG (Konstanz, Germany).

2.1.1 Site-Directed Mutagenesis

To specifically modulate the properties of the protein under investigation, site-directed mutagenesis was utilized to exchange specific amino acids. Selection of these amino acids and the type of substitutions were essentially motivated by structure analysis using the structure files with PDB codes 1ZUX (green form of EosFP), 2VVH (green form of IrisFP, on-state) and 2VVI (green form IrisFP, off-state). The substitution was performed by modifying the cDNA sequence of the target gene. The modification was performed by a *p*olymerase *c*hain *r*eaction (PCR), using appropriate primers, which encode for the base exchange (Figure 2.1).

The PCR was performed with the proofreading DNA polymerase PfuUltra, which exhibits error rates in the range of 10^{-6} to 10^{-7}. The PCR protocol was adjusted according to the properties of the primers and the recommendations of the enzyme manufacturers. Typical reaction conditions are specified in Table 2.1 and the sequences of the utilized primers are compiled in Table 2.2. Site-directed mutagenesis was carried out by using the 'QuickChangeII' kit (Quiagen, Hilden, Germany) or by mixing the individual components. The composition of a typical PCR reaction

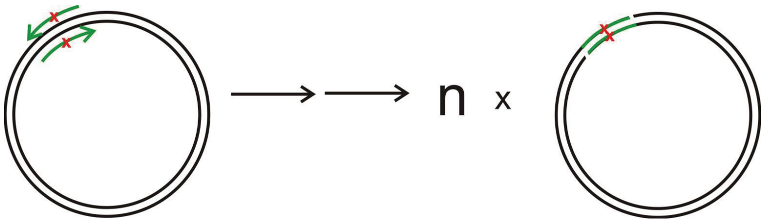

Figure 2.1: Schematic illustration of site-directed mutagenesis. The site-directed mutageneses PCR described above yields nicked PCR products, which contain the primer sequences (green), carrying the mutation (red cross). *n* represents the number of PCR cycles.

batch is indicated below.

PCR reaction batch:

- 10-50 ng template DNA
- ∼125 ng primer forward (5’ → 3’)
- ∼125 ng primer reverse (3’ → 5’)
- 0.2 mM dNTPs
- 2.5 u PfuUltra DNA polymerase

diluted in 50 µl PfuUltra DNA polymerase reaction buffer

Table 2.1: Reaction conditions for a site-directed mutagenesis PCR.

Reaction step	Temperature	Duration	Function
Denaturation	95°C	120 s	Untangling of the supercoiled plasmid and separation of the complementary DNA strands
Add 2 units polymerase			
Denaturation	95°C	30 s	Separation of the complementary DNA strands
Annealing	(55 ± 5)°C	30 s	Attachment of the primers.
Elongation	72°C	60 s per 1000 bp	Extension of the primer DNA by assembling free nucleotides into a new complementary DNA strand.
Repeat 15 to 30 times			
Elongation	72°C	10 min	Completion of unfinished DNA strands.
Digestion with DpnI for 60 min			

Table 2.2: Sequence of the utilized primers.

Name	Sequence
SITE-DIRECTED MUTAGENESIS	
Eos K145I	GGAGTCCCTCCACTGAGATAATGTATGTGCGTGATG
mEos H158R	GCTGACGGGTGATATTCGCATGGCTTTGTTGC
Eos Y189A	GGGTGTCAAGTTACCAGGCGCCCACTTTGTGG
Eos F173S	CCGATGTGACTCCAGAACTACTTACAAAGC
Eos E212Q	GGTTAAGCTGTATCAGCATGCTGTTGC
RANDOM MUTAGENESIS	
Acc65I-Eos-pQE32	GCAGACACTAGTCGACCCGGGGTACCTTATCGTCTGGCATTG
BamHI-Eos-pQE32	CGGAGAGCAGAGACACCATCACCATGGGATCCATATGAGTGC

2.1.2 Random Mutagenesis — *Error Prone* PCR

Random mutagenesis was applied to the cDNA of mEosFP*thermo* Phe173Ser utilizing an Error Prone approach. Here, mutations in the gene of interest are induced by performing a PCR reaction under conditions that promote the error-rate of the DNA polymerase. The JBS Error-Prone Kit (Jena Biosciene, Jena, Germany) increases the error rate of the Taq DNA polymerase (error rate usually $\sim 10^{-4}$ to 10^{-5}) by increasing the Mg^{2+}-concentration, partial substitution of Mg^{2+} with Mn^{2+} and using dNTP concentrations at unbalanced ratios. This approach yields a mutation rate in the range of 0.06-0.2 %.

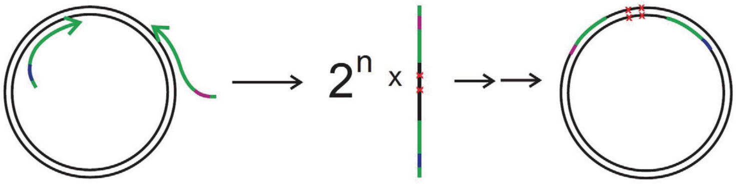

Figure 2.2: Principle of the generation of random clones. The error prone random PCR described above yields linear PCR products carrying one or more mutations (red crosses) in between the primer sequences (green). The PCR product was cloned into a pQE32 vector utilizing the restriction sites, encoded by a non-complementary base overhang of the two primers. The primers present recognition sites for different restriction enzymes (blue and violet), respectively. n represents the number of PCR cycles.

The PCR product featured a short base overhang, which was encoded by the primers. It presented restriction motives for BamHI and Acc65I (Table 2.2), which were used for cloning the PCR product into pQE32 using BamHI / Acc65I restriction enzymes (Figure 2.2). A clone library was generated by transforming the constructs into *E.coli* XL1-*blue*.

The PCR was performed in the following batch with the specifications listed in Table 2.3.

PCR reaction batch:

- 1-5 ng template DNA
- ~125 ng primer forward (5' → 3')
- ~125 ng primer reverse (3' → 5')
- 2 µl dNTP error prone mix (unbalanced dNTP ratio)
- 2-5 u Taq polymerase

diluted in 50 µl Error prone solution

Table 2.3: Reaction conditions for random mutagenesis.

Reaction step	Temperature	Duration
Denaturation	95°C	120 s
	Add polymerase	
Denaturation	95°C	60 s
Annealing	48°C	60 s
Elongation	72°C	60 s
	repeat 30 times	
Elongation	72°C	10 min

Screening

Bacterial colonies expressing a functional mEosFP*thermo* Phe173Ser variant turn green. Screening for enhanced photoconversion in comparison to mEosFP*thermo* Phe173Ser was based on the level of green-to-red recoloring of the colonies upon illumination. The colonies of the clone library were exposed to 366-nm light by placing the agar plates on a UV table ('Chroma 42', Laborgeräte Vetter, Wiesloch, Germany) for ~2.5 h. Colonies efficiently converting from green to red were secured by a dilution streak. We checked for reversible photoswitching of the selected positive clones using a wide field fluorescence microscope ('Antevert 135 TV', Zeiss, Göttingen, Germany). Single colonies of the respective clones were exposed to blue light, which was selected from the spectrum of the xenon lamp (XBO 75 W, Carl Zeiss, Jena, Germany) of the microscope by using a HQ 470/40 filter. The level of off switching was estimated by the loss in emission intensity (emission filter: HQ 525/50) of the colony during exposure to blue light, which was monitored with a

CCD camera (C3077, Hamamatsu, Hersching, Germany) over 5 minutes. To distinguish between off switching and irreversible bleaching, we exposed the colonies to 405-nm light of an externally installed laser diode (PPL-SL-405 nm-25, Laser 2000, Wessling, Germany) for ∼ 10 s. Subsequently, the emission intensity was checked upon recovery. To test for photoswitching of the red form of the respective clone, the protein expressed by the selected colony was photoconverted by applying 405-nm light of a laser diode (10 mW cm^{-2}; PPL-SL-405 nm-25, Laser 2000, Wessling, Germany) for 5 min. Off switching of the red emission was monitored during illumination with green light selected by an appropriate filter set. Clones with suitable photoswitching properties were cultured in 5 ml LB medium. The plasmids of these cultures was isolated using the PureYield^{TM} Plasmid Miniprep kit (Promega, Mannheim, Germany). The cDNA was commercially sequenced by the companies mentioned above.

2.2 Protein Expression and Purification

2.2.1 Cell Culturing

Plasmids were transformed into *E. coli* M15, BL21-gold or XL1-blue using a heat shock protocol (42°, 45 s). For protein expression, 50 - 100 ml LB or 2YT medium were inoculated with a single colony from an agar plate and cultured over night at 37°C as a starter culture. For the main culture, 1.5 l 2YT medium were inoculated with 5 - 10 ml of the starter culture. Protein variants based on mEosFP*thermo* were expressed overnight at 37°C. For other variants, the main culture was grown until it reached OD_{600} ∼ 1. Then it was cooled to 4 - 10°C, induced by adding 1 mM isopropyl β-D-1-thiogalactopyranoside and incubated with slight agitation until the culture medium turned green.

2.2.2 Protein Purification

The main culture was harvested by centrifugation. Cells were disrupted by ultrasonification or by using a pebble mill. Cell debris was pelleted by centrifugation. Proteins were isolated from the supernatant by metal affinity chromatography using a TALON® Superflow Resin matrix provided by Clontech Laboratories (Basel, Switzerland). Expression of proteins based on cDNA cloned into a pQE32 vector yielded fusion proteins of the target protein and a His-Tag, which adheres to the TALON® matrix material. Other proteins were rinsed out by washing the column with at least 5 times the volume of the matrix with buffer A (50 mM sodium phosphate, 150 mM NaCl, pH 7). The recombinant proteins were eluted with buffer A, containing 300 mM imidazole (Figure 2.3), which replaces the His-tag at the matrix material. The eluate was concentrated using an ultrafiltration spin column with an exclusion volume of 10 kDa (Sartorius Stedim Biotech, Germany). The buffer in the protein solution was exchanged by several cycles of concentrating and subsequent diluting of protein in buffer A. Alternatively, the concentrated protein was run over a NAP^{TM} 10 Column (Amersham Bioscience, Sweden). The produced protein contained less than 2% (w/w) impurities (estimated by software supported intensity comparison of the Coomassie Blue stained protein bands with the protein ladder (BenchMark^{TM}, Invitrogen, Darmstadt, Germany; *Quantity One* 4.6.7, Bio-Rad, München, Germany).

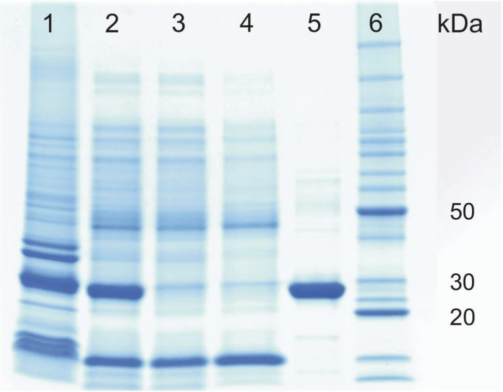

Figure 2.3: Steps of protein purification by affinity chromatography utilizing a TALON® matrix. The cell lysate was separated in cell debris (1) and supernatant (2). The protein was extracted from the supernatant by immobilized metal ion affinity chromatography (IMAC). Non-specifically bound proteins were rinsed out in several washing steps (3,4). The eluted protein contained less than 2% (w/w) impurities. The target protein (5) was identified by size, utilizing a BenchMark^{TM} protein ladder (6; Invitrogen)

2.2.3 Analytical Gel Filtration

The protein size was estimated by size exclusion chromatography, using a Superdex 75 10/300 GL column (GE Healthcare). The molecular mass determination was achieved by comparing the gel phase distribution coefficient, which is determined from the elution volume, with the values of calibration standards (Gel Filtration Calibration Kit LMW, GE Healthcare). The elution volume is obtained from the maximum peak of the elution profile monitored via the absorption at 280 nm. The calibration proteins were dissolved in 20 mM sodium phosphate buffer, 150 mM NaCl and loaded onto the column in two different runs (1: conalbumin, carbonic anhydrase and aprotinin; 2: ovalalbumin and ribonuclease A). The relationship between their gel phase distribution coefficients and the logarithm of their molecular mass was linearly fitted, yielding the calibration curve. This curve was used for the determination of the molecular mass of the protein of interest at different protein concentrations. The protein concentration was calculated from the absorption at 280 nm in the peak maximum fraction. Details of the procedure are described in the manual of the GE Healthcare Gel Filtration Calibration Kit LMW (data file 28-4073-84 AA).

The molecular mass, plotted as a function of protein concentrations were fitted with

$$MW = MW_0 + \frac{MW_0}{1 + (\frac{K_D}{c})^{\mathrm{n}}} \tag{2.1}$$

to determine the dissociation coefficient, K_D, of the protein dimer. Here, MW describes the molecular mass at a particular concentration, MW_0 the molecular mass of a monomer, K_D the dissociation coefficient of the dimer and n the Hill coefficient.

Chapter 3

Tracking Structural Modifications by Spectroscopy

3.1 Principles of Light-Matter Interaction

Optical spectroscopy utilizes the interaction of light with matter. This interaction can be understood with the concept of wave-particle duality that combines the classical description of light as a transversal electro-magnetic wave with the description of light as particles called photons of distinct energy given by

$$E = h\nu \qquad \text{and} \qquad \nu = \frac{c}{\lambda} \tag{3.1}$$

E denotes the energy of the photon, h the Planck's constant, ν the frequency, c the speed of light and λ the wavelength.

In UV/Vis spectroscopy in the spectral range of 200-750 nm, light typically interacts with the π- and n-orbitals of the valence electron system of chromophores. If the energy of a photon fulfills the resonance condition between two singlet states of the chromophore, the photon is absorbed, transferring its energy to the chromophore and, thereby, inducing its transition to a higher electronic level. Even small variations in the molecular structure can give rise to modified electronic levels, entailing electron redistribution, changes in the vibrational frequencies and, eventually, polarization of the chromophore. Optical spectroscopy provides sensitive methods to correlate these changes with the shape and the position of the respective spectra and is therefore a powerful tool to judge differences in molecular structure.

Jablonski Diagram

In 1935, Aleksander Jabłoński described the transition between the molecular electronic ground state and higher energy levels, which he summarized schematically in the Jablonski diagram. The Jablonski diagram depicts the different energy levels with horizonal lines, which are connected by vertical lines, representing the radiative and non-radiative transition mechanisms (Figure 3.1).

Figure 3.1: Jablonski diagram. Schematic illustration of electronic transitions between different energy levels.

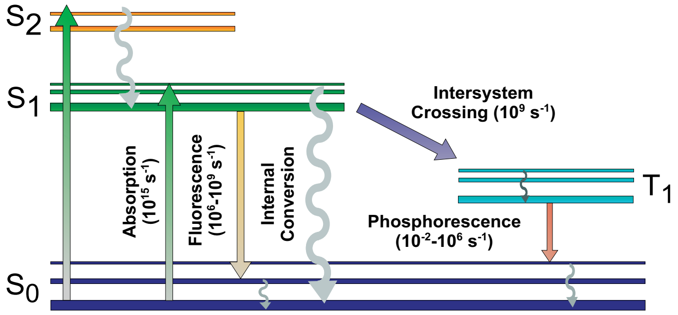
S2
S1
S0
T1
Absorption (10^15 s^-1)
Fluorescence (10^6-10^9 s^-1)
Internal Conversion
Intersystem Crossing (10^9 s^-1)
Phosphorescence (10^-2-10^6 s^-1)

At ambient temperature, almost all electrons exist in antiparallel pairs in the ground state, i.e. spin 0. Absorption of a photon of a particular energy, i.e. light of a particular wavelength, results, with a certain probability, in the transition of the electronic system from the ground state S_0 to a higher vibrational level of the first excited state S_1, while preserving the spin state. Within picoseconds, this higher vibrational level of the chromophore relaxes thermally along the S_1 potential surface. During this process, termed internal conversion, the absorbed energy dissipates through vibration (heat dissipation) or by collision with solvent molecules. If the S_1 and S_0 potential surfaces cross, internal conversion also results in non-radiative relaxation to the ground state. Non-crossing potential surfaces of two singlet states requires relaxation through emission of a photon, observed as fluorescence, which occurs usually within 10^{-9}-10^{-6} s. Here, the chromophore ends up at a higher vibrational level of the ground state. The population of the individual vibrational ground state levels is temperature dependent and adjusts by internal conversion. However, with a low probability, the spin state of the excited electron system may flip, leading to a transition from the singlet (spin = 0) to the triplet state (spin = 1) at a point where the two potential surfaces cross. This process, denoted as intersystem crossing, results in an electron pair featuring parallel spin. Relaxation from a triplet state requires spin reversal, which is forbidden, and, therefore, occurs with a very low probability. Consequently, relaxation of the triplet state takes place on very long time scales (10^{-2} - 10^{2} s). Its radiative relaxation by photon emission is termed phosphorescence.

Franck-Condon Principle

The overlap integral of the wavefunctions of the ground and excited state determines the excitation probability. This probability can be estimated with the Franck-Condon principle, which is illustrated for a two-atomic model in Figure 3.2. The overlap integral can be solved assuming the Born-Oppenheimer approximation that separates the wavefunctions of electrons and nuclei, based on their large differences in mass. The small mass of the electrons allows fast adaption (10^{-15} s) to the coulomb attraction of the slowly vibrating nuclei (frequences $\sim 10^{-13}$ s). The fast reorientation of the electrons is indicated as a vertical transition in Figure 3.2, illustrating that the overlap integral between the wavefunctions of the ground state and a higher vibrational level of the excited state increases with increasing distance of the nuclei. Thus, the transition of the system to a higher vibrational level of S_1 becomes increasingly likely. Depending on the relative positions of the nuclei in the vibrating system, different vibrational levels are accessed. The particular transitions cause multiple lines in the absorption spectrum, which, among other things, widen by natural or pressure line broadening, resulting in the typically observed absorption bands.

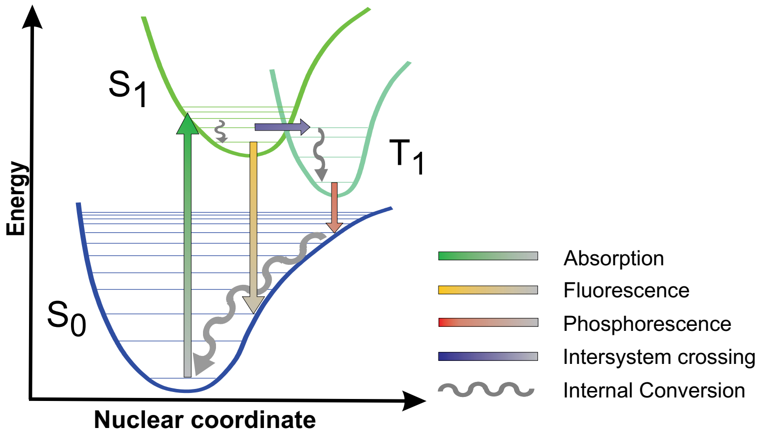

Figure 3.2: Schematic illustration of the Frank-Condon principle. Electronic transitions between different energy levels that are depicted by Morse potentials.

3.2 Absorption Spectroscopy

Absorption spectroscopy is a sensitive method to analyze the relative changes in the geometry of the electronic and vibrational potentials of the ground state S_0 and first excited state S_1. As illustrated by the Franck-Condon principle (Figure 3.2), these geometry changes are associated with the absorption probability of a photon of a particular wavelength and polarization, which is directly related to the molar extinction coefficient, ε. Thus, variations in the extinction coefficient indicate structural modifications, which is utilized in the interpretation of the spectroscopic data of different protein variants or species. The molar extinction coefficient is specific of each molecule species at a given wavelength, λ. Upon passing through a sample of thickness d, the intensity of the incident light, I_0, is reduced to I by light absorption (Figure 3.3). The decay of the light intensity on its way through the sample is described by Equation 3.2.

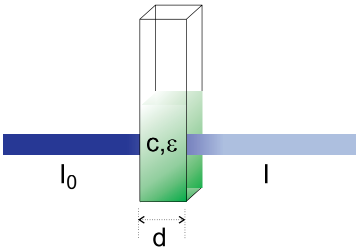

Figure 3.3: Absorption of light passing through a sample.

$$I = I_0 \, e^{-\varepsilon'(\lambda)dc}, \tag{3.2}$$

The resulting Equation 3.3, denoted as Lambert-Beer's law, directly relates the absorbance at a particular wavelength, A_λ, to the concentration of the absorbing molecules, c. Transposing this equation by taking the logarithm yields Lambert-Beer's law, with $\varepsilon'(\lambda) = \varepsilon(\lambda) \ln 10$

$$A_\lambda = -\log \frac{I_0}{I} = \varepsilon(\lambda) dc \tag{3.3}$$

The center of an absorption band is determined by the energy difference between the S_0 and S_1 states. Hence, band shifts reflect changes in the energy levels. Such shifts can be utilized as sensor for alterations of the electronic conditions in the chromophore vicinity, e.g. induced by changes in polarity, structural constitution and conformation of surrounding residues.

Samples were prepared in 20 mM buffer with an overall ionic strength of 150 mM. The protein was diluted to a final concentration of 1-30 µM. The absorption spectra were recorded with a Cary 50 or Cary 300 Bio UV/Vis spectrometer (Varian, Darmstadt, Germany) at a resolution of 0.4 nm. All experiments were carried out at ambient temperature, if not explicitly indicated otherwise.

Analysis of pH Sensitivity

The photophysical properties of the studied FPs are sensitive to changes in pH. The pH affects the protonation state of the chromophore and the polarity in the chromophore vicinity. The chromophore protonation state can be inferred from the relative amplitudes of the A and B bands of the absorption spectrum. Alteration of the polarity in the chromophore vicinity was judged by shifts in the absorption band position.

Experiments were performed with ∼ 2-5 µM protein in 20 mM buffer. The ionic strength of the respective buffer was adjusted with NaCl to 150 mM. The used buffer systems are listed in Table 3.1.

Table 3.1: Buffer systems used for the investigation of the pH sensitivity.

pH range	Buffer system
3.0 - 6.2	sodium citrate / sodium dihydrogen phosphate
6.2 - 8.7	sodium dihydrogen phosphate / disodium hydrogen phosphate
8.8 - 11.0	sodium hydrogen carbonate / disodium carbonate

The pH dependence of the equilibrium between a protonated and a deprotonated species can be modeled with the Henderson-Hasselbalch equation (Equation 3.4).

$$\mathrm{pH} = \mathrm{p}K_a + \log \frac{[\mathrm{X}^-]}{[\mathrm{X}^H]} \tag{3.4}$$

Here, X^- and X^H represent the deprotonated and the protonated species, respectively. To describe mixtures of populations featuring different equilibrium constants, Equation 3.4 was extended accordingly (Equation 3.5).

$$[\mathrm{X}^-] = \sum_{i=1}^{\infty} A_i \frac{1}{1 + 10^{pK_{a,i} - pH}} \tag{3.5}$$

The sum is extended over the populations, i, that contribute to the overall chromophore deprotonation with the amplitude A_i.

Calculation of Molar Extinction Coefficients

Aromatic amino acids cause an absorption band, which is typically observed at ~ 280 nm. The exact position and extinction coefficient of this band depend on the number of the respective aromatic amino acids in the protein sequence[137]. The concentration of the protein solutions was calculated from the absorbance in this band, according to Lambert-Beer's law, assuming a molecular extinction coefficient, ε (280 nm), of 27,500 $\mathrm{M^{-1}\,cm^{-1}}$ (calculated for IrisFP with *ProtParam*, www.expasy.org). Absorption spectra of the chromophores of the studied fluorescent proteins often represent a mixture of different subpopulations. The fractions of the individual species at a particular pH value were calculated from the equilibrium constants. If the absorption bands of individual species are spectroscopically well separated, their extinction coefficients could be calculated from the absorbance at a particular wavelength within their respective absorption band, using Lambert-Beer's law. If the spectra of different species are superimposed, the fractions of the individual components were extracted by fitting the overall spectrum to a linear combination of the individual spectra of the involved species.

Photoactivation Experiments

Photoswitching was induced by illumination with light of particular wavelengths, selected from a 150-W Xenon lamp with appropriate interference filters. Off switching of green and red IrisFP variants was induced by a 50 nm wide band of light centered on 470 nm (470/50 nm) and by light of 535/30 nm. For on switching of the green and the red forms, 400/100 nm and 450/50 nm were selected. Photoconversion was monitored under 400/100 nm illumination. Experiments with this setup were used for qualitative studies only. Quantitative analyses of the photoactivation reactions were performed as described in Section 3.4.

Thermal Recovery

Samples of green and red IrisFP and its variants were illuminated with blue and green light, respectively, until the color of the protein solution faded. Subsequently, the absorption increase at the maximum absorption wavelength of the respective species was followed over time. Some experiments were performed at 37° using a thermostatted cuvette holder.

3.3 Circular Dichroism

The probability of absorbing a photon is related to its polarization. Thus, the extinction coefficients for left and right circularly polarized light differ slightly in optically active molecules. This property is utilized in circular dichroism (CD) spectroscopy. For recording of CD spectra, the sample is illuminated with linear polarized light, which is alternating between the left and right circularly polarized components. The different absorption of the two polarizations causes the elliptical polarization of the emergent light. Although ΔA_λ is measured, for historical reasons, it is usually expressed in degrees of ellipticity Θ. The ellipticity is directly related to the difference of the extinction coefficients of left and right circularly polarized light by

$$\Theta(\lambda) \approx 3300\Delta\varepsilon(\lambda) \tag{3.6}$$

Circular dichroism spectra were recorded on a J-810 spectropolarimeter (Jasco Europe S.R-L, Cremella, Italy). Samples were prepared by diluting the protein to $\sim 30\,\mu\mathrm{M}$ in buffer (Table 3.1). Off-state spectra were recorded after illuminating the protein solution with 473-nm light until the color of the sample faded.

3.4 Fluorescence

Photon absorption populates a higher vibrational level of the excited state, S_1, which relaxes on the S_1 potential surface by internal conversion (Section 3.1). Subsequently, radiative relaxation of S_1 occurs to a higher vibrational level of the ground state, which also internally converts to the thermally relaxed state, dissipating energy. Thus, the emitted photon has less energy than the initially absorbed one. The energy of the emitted photon is decreased even further by solvent effects. Solvent molecules surrounding the chromophore rearrange to adjust to the changed electronic conditions of the excited chromophore, hence stabilizing the excited state but destabilizing the ground state in the process. This effect reduces the difference in free energy between S_1 and S_0, decreasing the energy of the emitted photon even further. The emission wavelength is, therefore, red shifted to the absorption wavelength. The difference between these two wavelengths is termed Stokes shift. In FPs, the 'solvent' of the chromophore is its protein vicinity. Hence, the extent of the Stokes shift is a measure of the vibrational levels accessed by chromophore excitation and of the structural response to the electron redistribution in the excited state chromophore.

Spectra were recorded on SPEX Fluorolog II and Fluorolog III spectrofluorometers (Spex Industries, Edison, NJ) that are equipped with a 450-W xenon lamp, closed cycle cryostats and temperature controllers, respectively. The spectral resolution was set to 0.85 nm. For sample preparation, the protein was diluted to ~ 1 µM in the buffers described above (Table 3.1).

Fluorescence Quantum Yield Determination

The fluorescence quantum yield of the studied fluorescent proteins, ϕ_{fl}, was obtained by relating the absorption at the excitation wavelength to the integrated fluorescence intensity at different sample concentrations. Plotting the integrated fluorescence intensity against absorption results in a line. The slope (m_{FP}) is compared to the slope obtained with a reference sample, m_{ref}, of known quantum yield, ϕ_{ref}, measured by the same procedure. ϕ_{fl} is given by

$$\phi_{fl} = \phi_{ref}(\frac{m_{FP}}{m_{ref}})(\frac{n_{FP}^2}{n_{ref}^2}) \tag{3.7}$$

where n represents the refractive indices of the solvents, in which the FP and the reference sample are dissolved, respectively.

Low Temperature Experiments

For experiments at cryogenic temperature (15 K), the protein was diluted in 20 mM potassium phosphate buffer, 150 mM potassium chloride, containing 75 % (v/v) glycerol. The sample was kept in a closed-cycle helium cryostat (model 22, CTI Cryogenics, Mansfield, MA) equipped with a Lake Shore Cryotronics (Westerville, OH) model 330 digital temperature controller.

Quantitative Analysis of Photoactivation

For better control of the illumination conditions during photoactivation the experiments were performed with monochromatic light. Wavelength selection and intensity were regulated with an *a*custo *o*ptical *t*unable *f*ilter (AOTF). The setup, including the fluorometer, is illustrated in Figure 3.4.

The kinetics of photoactivation was monitored at a single wavelength over time. Typical time traces resulting from these experiments are depicted in Figure 3.5.

Figure 3.4: Optical setup for the photoswitching experiments mounted at the Fluorolog II fluorometer.

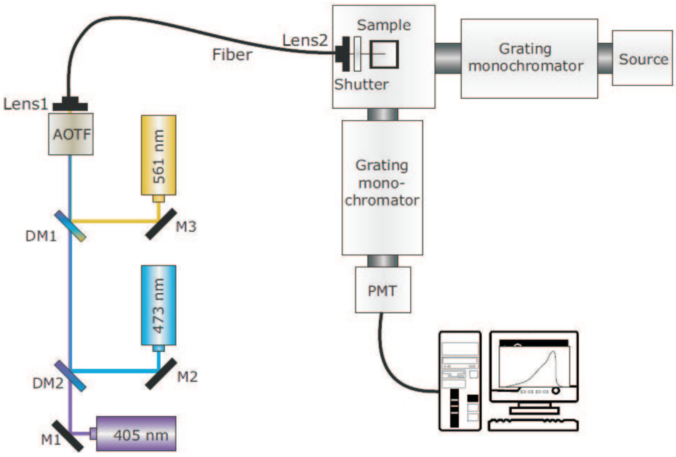
Sample
Lens2
Fiber
Shutter
Grating monochromator
Source
Lens1
AOTF
561 nm
Grating mono-chromator
DM1
M3
PMT
473 nm
DM2
M2
M1
405 nm

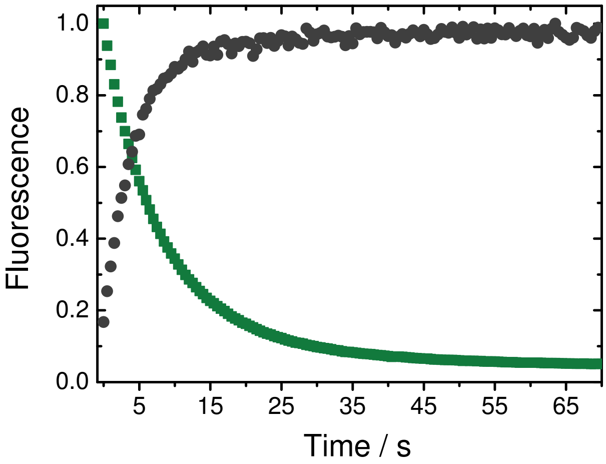

Figure 3.5: Time traces of the emission intensity during photoswitching. Off switching, emission intensity upon 473-nm illumination (green) and on switching, emission intensity upon subsequent 405-nm illumination (gray).

The time traces were fitted with a stretched single exponential function.

$$y = A_1 e^{-\left(\frac{\tau}{t}\right)^{\beta}} + A_0 \tag{3.8}$$

Here, the fluorescence signal, y, is described by the amplitude of the signal change, A_1, the residual fluorescence after photoswitching, A_0, the lifetime, τ, the stretching factor, β, and the time, t.

The mean lifetime $\langle\tau\rangle$ is calculated according to

$$\langle\tau\rangle = \frac{\tau}{\beta}\Gamma\left(\frac{1}{\beta}\right) \tag{3.9}$$

with Γ representing the Gamma function.

The rate coefficient of the photoactivation reaction is inversely proportional to the lifetime τ and is given by

$$k = \frac{1}{\tau} = \phi\,\varepsilon\,(\lambda)\,\ln 10\,\frac{\lambda\,P}{N_A\,h\,c} \tag{3.10}$$

It is determined by experiment-specific parameters, i.e. the power density P and the excitation wavelength, λ, sample-specific parameters, i.e. the extinction coefficient at the excitation wavelength, $\varepsilon\,(\lambda)$, and the quantum efficiency of a particular process, ϕ, and on the fundamental physical constants, i.e. Avogadro's number, N_A, Planck's constant, h, and speed of light, c.

Therefore, the quantum efficiency is given by

$$\phi = \frac{k}{\varepsilon(\lambda)\,\ln\,10}\,\frac{1}{\lambda\,P}\,(N_A\,h\,c) \tag{3.11}$$

As thermal relaxation of metastable chromophore species occurs on time scales three orders of magnitude larger than light-induced processes it can be neglected for the evaluation of photoreactions. However, multiple photoreactions induced by light of the same wavelength have to be considered. Therefore, we have to assume that the measured rate coefficients represent net coefficients containing several components. They are therefore termed 'apparent'. Apparent rate coefficients are denoted by subscripts describing the net reaction (off or on), whereas subscripts with 'c', abbreviating '*cis*' and 't', abbreviating '*trans*', describe a particular reaction in the indicated direction.

Determination of the Activation Energy

The activation energy was determined by the temperature dependence of the respective photoactivation reaction, according to Eyring theory (Equation 3.12).

$$k = \frac{k_b T}{h} e^{-\left(\frac{\Delta H^*}{RT}\right)} e^{\left(\frac{\Delta S^*}{R}\right)} \tag{3.12}$$

During the reaction, the temperature was controlled by a thermoelement that was placed directly into the solution in the cuvette. The time traces at a particular temperature were fitted with a stretched exponential function (Equation 3.8), yielding a rate coefficient, k. The activation enthalpy was calculated from the slope of the linearized plot of Equation 3.12, ln $\frac{k}{T}$ against the reciprocal temperature.

$$\ln\frac{k}{T} = -\frac{\Delta H^*}{R}\frac{1}{T} + \ln\frac{k_b}{h} + \frac{\Delta S^*}{R} \tag{3.13}$$

where the activation enthalpy, ΔH^*, is determined by the activation entropy ΔS^* and the fundamental constants: Boltzmann constant, k_b, the gas constant, R, and Plank's constant h.

Measurement of the Action Spectra

The action spectrum represents the efficiency of an individual photoactivation reaction upon illumination with light of a particular wavelength. In IrisFP, photoactivation was monitored by the change in the green and red emission intensity, respectively. The green and red emission bands, excited at 470 nm, and 540 nm, respectively, were recorded before and after illumination at a particular wavelength for 300 s. The relative change of the integrated emission intensity compared to the initial one was plotted against the respective wavelength, yielding the action spectrum. For mIrisGFP, the relative emission decrease at 520 nm (λ_{ex} = 330-490 nm) and 540 nm (λ_{ex} = 490-530 nm) was directly estimated from the ratio of the initial to the final emission intensity of a 300 s time trace recorded with excitation at the respective wavelength.

Fluorescence Correlation Spectroscopy

Fluorescence correlation spectroscopy was performed on a $\sim 30\,\mathrm{nM}$ protein solution in $20\,\mathrm{mM}$ pH 7 sodium phosphate buffer, $150\,\mathrm{mM}$ sodium chloride. The sample was excited with the 488-nm line of an argon laser (Stabilite 2017, Spectra-Physics) at $3\,\mu\mathrm{W}$ using a $60\times/1.2$w water immersion objective (UPLAPO, Olympus). Each correlation curve was integrated over $15\,\mathrm{s}$. Details of the experimental setup have been published[138,116,139].

Error Determination

Errors are calculated as standard deviation of at least three independent measurements.

Part III

Results and Discussion

Chapter 4

Combining Reversible and Irreversible Switching Modes - IrisFP

4.1 Introduction

The previously introduced EosFP changes its emission color from green to red upon excitation with $\sim$400-nm light. Random mutagenesis based on this protein yielded a variant with two point mutations, Phe173Ser and Phe191Leu. Phe191Leu has essentially no effect on the properties of EosFP. In contrast, Phe173 is in close proximity to the chromophore. Its substitution by a serine might affect the stabilization of the chromophore and, therefore, change its photophysical properties. Actually, the color of a EosFP Phe173Ser, Phe191Leu protein solution changes from green to almost colorless upon illumination with blue light (Figure 4.1 a, $\mathrm{cG} \rightarrow \mathrm{tG}$). Furthermore, continuous illumination of the colorless protein solution with intense violet light induces an irreversible recoloring of the sample towards red (Figure 4.1 a, $\mathrm{tG} \rightarrow \mathrm{cR}$). By exposing the solution to green light, its color changes once again, this time to orange (Figure 4.1 a, $\mathrm{cR} \rightarrow \mathrm{tR}$). Under weak UV-illumination, the green (cG) and red (cR) protein solutions fluoresce brightly in green and orange, respectively (Figure 4.1 b, cG / cR). The color conversions of the green and red protein solutions by blue and green light, respectively, are accompanied by a temporary decrease in the emission intensity (off switching, Figure 4.1 b, tG / tR). Inspired by the variety of colors, this random variant was named after the Greek goddess of the rainbow, Iris[120].

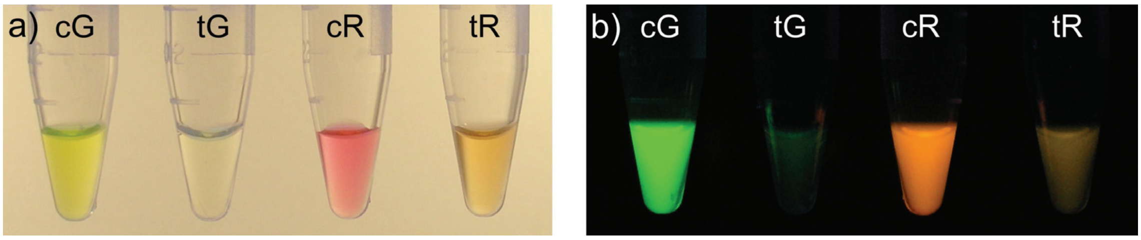

Figure 4.1: IrisFP protein solution after different illumination conditions. Color changes of a protein solution were monitored (a) at daylight and (b) with 254-nm illumination. The green protein solution (cG) becomes colorless upon illumination with 473-nm light (tG). Photoconversion from green to red was achieved by continuous 405-nm light illumination of green protein solution at 37°C, pH 7. The red protein solution (cR) becomes orange upon illumination with 532-nm light and shows significantly reduced emission intensity (tR).

4.1.1 Structural Background of Photoinduced Color Changes

IrisFP crystals were analyzed under different illumination conditions. Like the protein solutions, the crystals display different colors upon irradiation with blue, violet or green light (Figure 4.2).

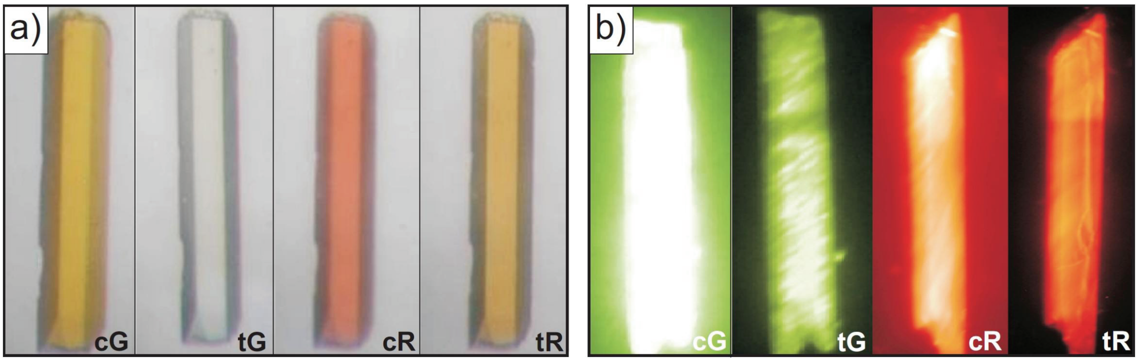

Figure 4.2: IrisFP crystals under different illumination conditions. Green IrisFP crystals before (cG) and after 473-nm illumination (tG) in absorption mode (a) and in fluorescence mode (b). Continuous 405-nm illumination of tG results in red IrisFP crystals, which are shown before (cR) and after 532-nm illumination (tR) in absorption (a) and fluorescence mode (b). Photographs of IrisFP crystals were reproduced from Virgile Adam with his kind permission.

IrisFP crystallizes as a tetramer, its subunits showing a classical β-can fold (Section 1.1.1)[120]. The chromophore is stabilized in a slightly twisted *cis* conformation by hydrogen bonds to Ser142 and two water molecules (Figure 4.3 a). The replacement of Phe173 by the smaller serine in IrisFP facilitates the rearrangement of the Met159 side chain, which rotates away from the chromophore and, thereby, reduces steric constraints (Figure 4.3). As a result, two water-filled cavities are created, which may lead to enhanced chromophore flexibility. For comparison, in EosFP, the chromophore is in van der Waals contact with Met159 and hydrogen-bonds to a water molecule.

Green-to-Red Photoconversion

The X-ray structure analysis of red IrisFP (cR) was performed after 405-nm illumination of a green crystal (Figure 4.2). The molecular structure was similar to the one described previously for EosFP[109] (Section 1.3.1). Backbone cleavage between Phe61 and the β-carbon atom of the His62 indicates a β-elimination reaction, which extends the chromophore π-electron system toward the His62 side chain by implementing a double bond (Section 1.3.1). The global structures and the structures of the chromophore pockets of the green and red forms are nearly identical (Figure 4.3 b). The only difference is a water molecule next to His62, which is dislocated in the red form. This phenomenon was also reported for Kaede[108] and EosFP[109]. Overall, the results suggest a similar green-to-red photoconversion mechanism for EosFP and IrisFP.

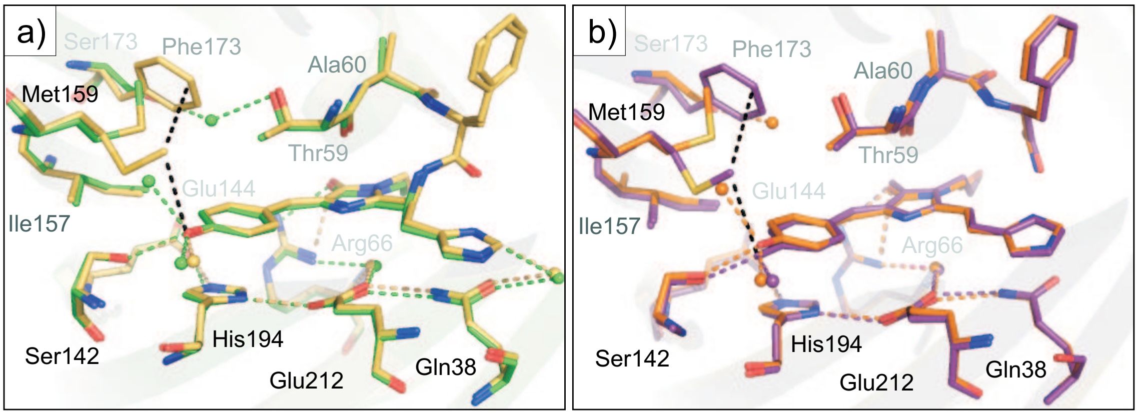

Figure 4.3: Structural differences between EosFP and IrisFP in the chromophore vicinity. (a) Green forms of IrisFP (green, PDB code: 2VVH) and EosFP (yellow, PDB code: 1ZUX). (b) Red forms of IrisFP (orange, PDB code: 2VVJ) and EosFP (purple, PDB code: 2BTJ), obtained after 405-nm illumination. Water molecules are shown as spheres, hydrogen bonds are represented by colored dotted lines, van der Waals contacts are indicated by black dotted lines.

Dark State Structures

To examine the structural basis of the photoinduced decoloring of the protein sample, a green IrisFP crystal (cG, Figure 4.2) was exposed to 488-nm laser light. As a result, the green crystal turned almost colorless and its emission intensity decreased (off-state; tG, Figure 4.2). It was flash-cooled immediately afterwards to conserve the photoinduced changes. The X-ray structure analysis of this dark state crystal reveals the chromophore in a non-planar *trans* conformation (Figure 4.4 b). The *trans* chromophore is stabilized by hydrogen bonds to a water molecule and Glu144. The *cis*-*trans* isomerization is accompanied by substantial rearrangements of several amino acids in the chromophore cavity. Transient repulsion during isomerization induces a flip of the Ile157 side chain of $\sim 145°$. The hydrogen bond between the chromophore phenylate oxygen and Ser142 no longer exists. Instead, Ser142 assumes two alternative conformations, with its side chain hydroxyl pointing either toward a water molecule or His194, which also changed its conformation. The His194 side chain, originally π-stacking to the phenyl group of the *cis* chromophore, flips by $\sim 120°$ and, thereby, the previous hydrogen bonds to Glu144 and Glu212 are removed. The carboxyl moiety of Glu212 rotates by $\sim 90°$ and establishes a hydrogen bond to the N_δ of the chromophore imidazolinone group and to Arg66, which repositions close to the former slot of His194.

The crystal structure of the red photoswitched IrisFP (tR) was analyzed after 532-nm illumination of cR and subsequent flash-cooling. The electron density indicates the existence of both, *cis* and *trans* isomers of the chromophore (Figure 4.4), which possibly results from the limited penetration depth of the green light into the crystal and the choice of the excitation wavelength (532 nm). The efficiency of photoswitching to the off-state is most likely limited by the spectral overlap of the involved red chromophore species. Still, partially *cis*-*trans* isomerized red IrisFP displays the same structural features in the chromophore vicinity as the green *trans* form (tG).

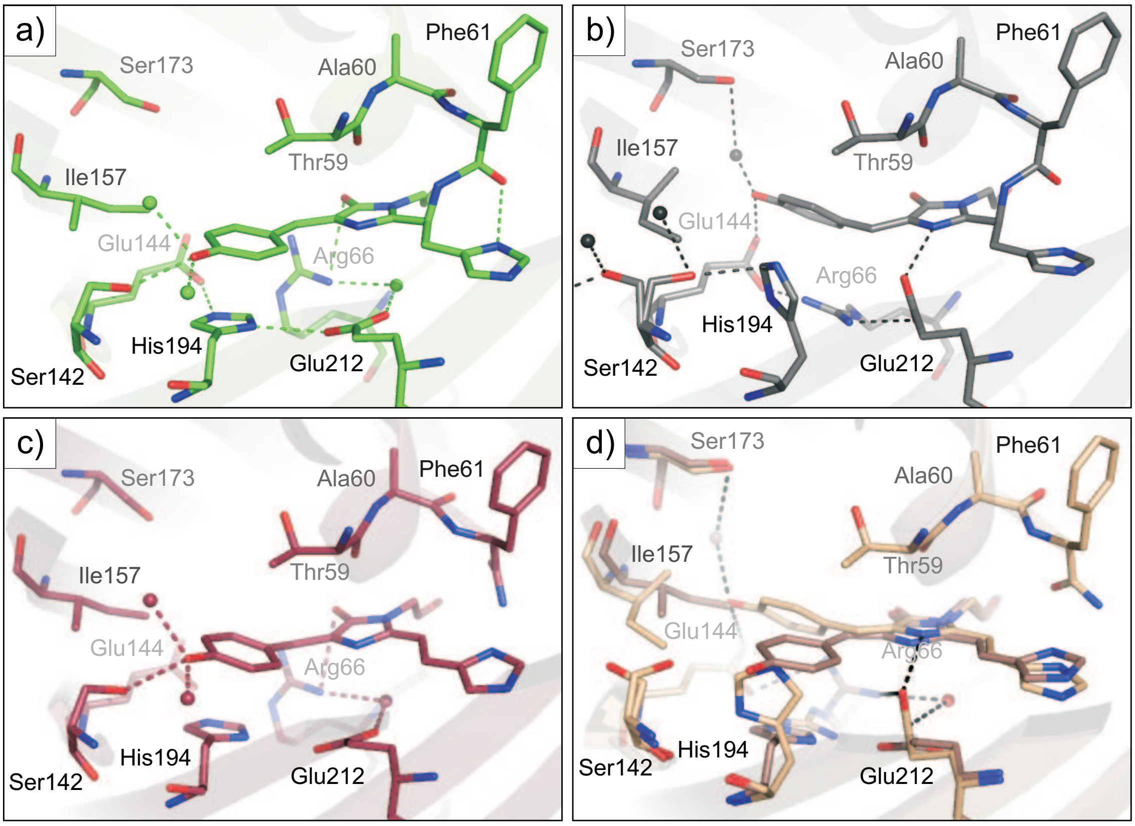
a)
Ser173
Ala60
Phe61
Thr59
Ile157
Glu144
Arg66
His194
Glu212
Ser142
b)
Ser173
Ala60
Phe61
Ile157
Thr59
Glu144
Arg66
His194
Ser142
Glu212
c)
Ser173
Ala60
Phe61
Ile157
Thr59
Glu144
Arg66
His194
Ser142
Glu212
d)
Ser173
Phe61
Ala60
Ile157
Thr59
Glu144
Arg66
His194
Ser142
Glu212

Figure 4.4: Structural changes in the chromophore vicinity of IrisFP upon photoswitching. (a) Native green fluorescent state (PDB code: 2VVH) and (b) non-fluorescent off-state obtained upon 488-nm illumination (PDB code: 2VVI). (c) Photo-converted red form (PDB code: 2VVJ) and (d) partially photoswitched state of the red fluorescent form of IrisFP, obtained by 532-nm illumination[120]. Water molecules are shown as spheres, hydrogen bonds are represented by dashed lines.

4.2 Spectroscopic Characterization of IrisFP

The spectroscopic properties of the green and red forms of EosFP and IrisFP are similar, even if they exhibit a few striking differences (Figure 4.5). The absorption spectra of IrisFP are much broader than those of EosFP, and the Stokes shift is significantly larger. Both observations suggest a higher flexibility of the chromophore in IrisFP, which might result in stronger electrostatic interactions of the chromophore with its vicinity. Extinction coefficients and quantum yields of the anionic chromophore are also reduced, probably due to an increased probability of internal conversion, further supporting the previous hypothesis. The photophysical parameters of EosFP and IrisFP are compiled in Table 4.1.

Table 4.1: Spectral properties of IrisFP and EosFP^{a}

	green EosFP	red EosFP	green IrisFP	red IrisFP
ANIONIC CHROMOPHORE				
$\lambda_{\max}$ (Ex/Em), nm	506 / 516	571 / 581	488 / 516^{b}	551 / 580^{b}
ε_c ($\lambda_{\max}$), M^{-1} cm^{-1}	72,000	41,000	50,800 $\pm$ 2,000	32,000 $\pm$ 2,800
ϕ_{fl}	0.70 ± 0.02	0.62 ± 0.03	0.43 ± 0.02	0.47 ± 0.02
NEUTRAL CHROMOPHORE				
$\lambda_{\max}$ (Ex/Em), nm	n.a.	n.a.	380 / 455^{c}	451 / 502^{c}
ε_c ($\lambda_{\max}$), M^{-1} cm^{-1}	n.a.	n.a.	22,000 $\pm$ 2,300^{d}	11,300 $\pm$ 4,100^{d}
ϕ_{fl}	n.a.	n.a.	0.027 ± 0.007	0.036 ± 0.008

[a] All values were estimated in 20 mM buffer, 150 mM ionic strength.

[b] Values at pH 10, peaks shift with pH.

[c] Values at pH 5, peaks shift with pH.

[d] Mean value for pH 7 to pH 4.

Compared to green EosFP, the green form of IrisFP shows an 18-nm hypsochromic shift in the main absorption band. It peaks at 487 nm and features a vibronic shoulder at ~ 460 nm (B_c^G band). Its overall shape is broader (full width half maximum (FWHM) 55 nm) compared to EosFP (FWHM 25 nm) and its extinction coefficient is reduced (IrisFP: ε (487 nm) = 50,800 $\pm$ 2,000 M^{-1} cm^{-1}; EosFP: ε (506 nm) = 72,000 M^{-1} cm^{-1} [116]).

At lower pH, a minor absorption band arises at 390 nm (A_c^G band, ε (390 nm) = 22,000 $\pm$ 2,300 M^{-1} cm^{-1}, Figures 4.6 and 4.7). The A_c^G and B_c^G bands interchange with pH in two steps, yielding $pK_{a_1} = 5.7 \pm 0.1$ and $pK_{a_2} = 8.3 \pm 0.1$ (Figure 4.6 a). A single isosbestic point at 424 nm indicates a two-state-transition, which underlines the association of the B_c^G band with the anionic chromophore and of the A_c^G band to the neutral chromophore (data not shown).

Excitation of the anionic chromophore (B_c^G band) induces fluorescence with peak emission at 516 nm. The quantum yield of this process is significantly reduced compared to EosFP (IrisFP: $\phi_{\text{fl}} = 0.43 \pm 0.02$; EosFP: $\phi_{\text{fl}} = 0.70 \pm 0.02$), in accordance with the hypothesis of a higher chromophore flexibility. Photoexcitation within the neutral absorption band A_c^G band leads to weak fluorescence peaking at 455 nm ($\phi_{\text{fl}} = 0.027 \pm 0.007$). Intense illumination within the A_c^G band by 405-nm light induces a red shift of the spectral bands of IrisFP, which is a consequence of the extension of the chromophore π-electron system toward His62 upon photoconversion (Section 4.3.2). At basic pH, the main absorption band of the red form of IrisFP is 20-nm blue shifted compared to the main absorption band in EosFP. It is maximal at 551 nm and has a vibronic shoulder at ~ 515 nm (B_c^R band, Figure 4.5 b). As for the green form, the extinction coefficient of red IrisFP is also reduced compared to red EosFP (IrisFP: ε (551 nm) = 32,000 ± 2,800 M^{-1} cm^{-1}; EosFP: ε (571 nm) = 41,000 M^{-1} cm^{-1} [116]). A minor absorption band at 360 nm shows two significant vibronic shoulders at 351 and 337 nm, respectively. Excitation in either the 551-nm or the 360-nm band results in maximal fluorescence at 580 nm. Therefore, the 360-nm absorption band was assigned to an higher-order electronic transition of the anionic chromophore. The fluorescence quantum yield is lower than for red EosFP (IrisFP: $\phi_{fl} = 0.47 \pm 0.02$; EosFP: $\phi_{fl} = 0.62 \pm 0.03$).

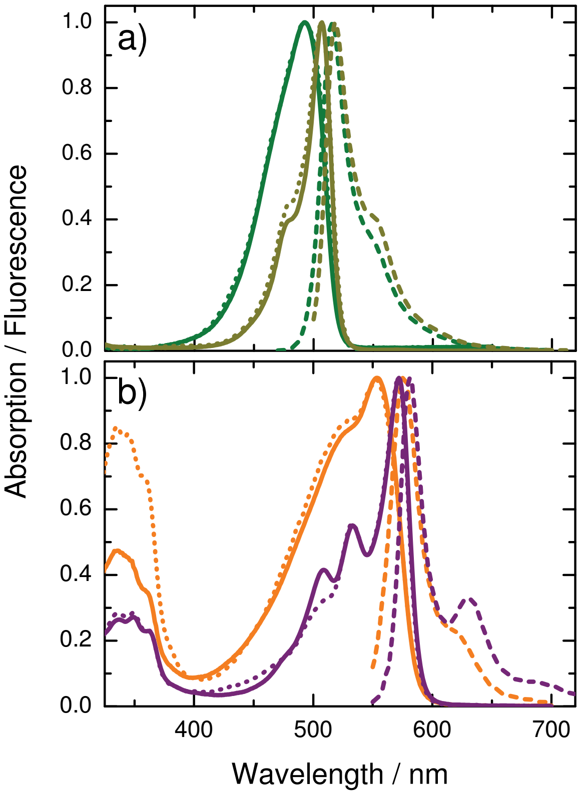

Figure 4.5: Spectroscopic comparison of EosFP and IrisFP. Absorption (solid lines), excitation (dotted lines) and emission spectra (dashed lines) of (a) the green forms of EosFP (yellow) and IrisFP (green) and (b) the red forms of EosFP (purple) and IrisFP (orange) at pH 10. The spectra are scaled to the same maximal amplitude.

With decreasing pH, the population of neutral chromophores increases. The deprotonation of the red chromophore occurs in two steps, with $pK_{a_1} = 5.9 \pm 0.1$ and $pK_{a_2} = 8.6 \pm 0.1$ (Figure 4.6 b). The neutral chromophore features a broad absorption spectrum, centered on ~ 450 nm and a shoulder is visible at ~ 435 nm (A_c^R band, ε (450 nm) = 11,500 ± 4,100 M^{-1} cm^{-1}). In addition, a red shifted band is observed at ~ 485 nm, which might originate from non-converted green IrisFP. Similar to the UV band observed for the anionic form, a minor absorption band associated with the neutral red chromophore shows up in the UV range at 334 nm together with a strong vibronic shoulder at 321 nm. Excitation in the A_c^R band and in the respective UV band results in weak fluorescence at ~ 500 nm ($\phi_{fl} = 0.036 \pm 0.008$). The absorption, excitation and emission maxima of the neutral red chromophore shift considerably with pH. However, the exact shift cannot be determined since residual green IrisFP distorts the spectra of the red species (Figure 4.7).

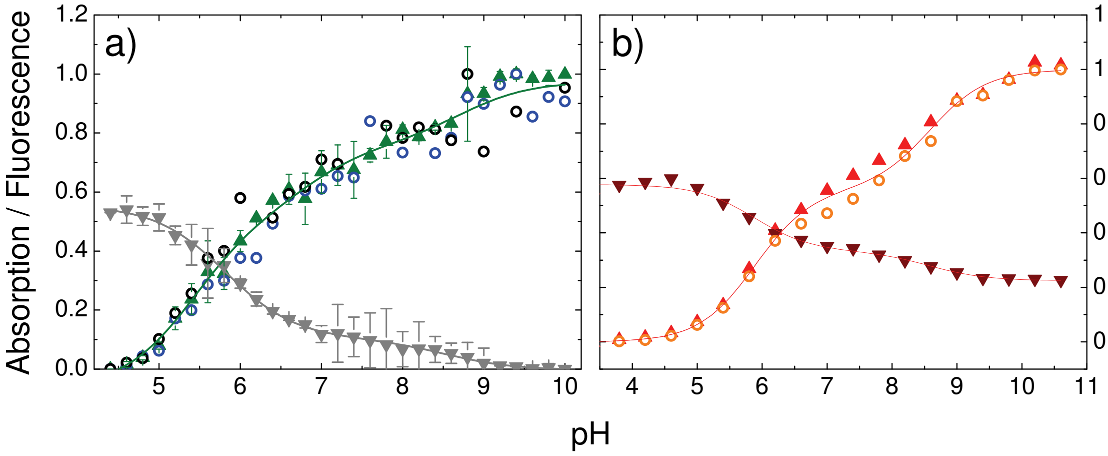

Figure 4.6: pH-dependence of the thermally relaxed IrisFP. (a) pH-dependence of the green form of IrisFP, monitored via the relative fractions of neutral and anionic chromophore represented by the intensities of the absorption A_c^G (gray triangles) and B_c^G bands (green triangles), the intensity of the fluorescence excitation band monitored for the emission at 540 nm (black circles) and the intensity of the fluorescence emission band monitored for excitation at 480 nm (blue circles). (b) A similar experiment was performed for the red form of IrisFP. Here, the relative intensities of the absorption A_c^R (bordeaux triangles) and B_c^R bands (red triangles) and the intensity of the fluorescence emission band monitored for excitation at 540 nm (orange circles) were measured. The absorption values are normalized relative to the maximum value of the absorption spectrum at pH 10 (green form) and pH 10.6 (red form). Intensities of the fluorescence bands are normalized to the match with the absorption B_c^G (B_c^R) band intensities. Experiments were performed with ~ 2 µM protein solution at varying pH values. Buffer conditions are specified in Section 3.2.

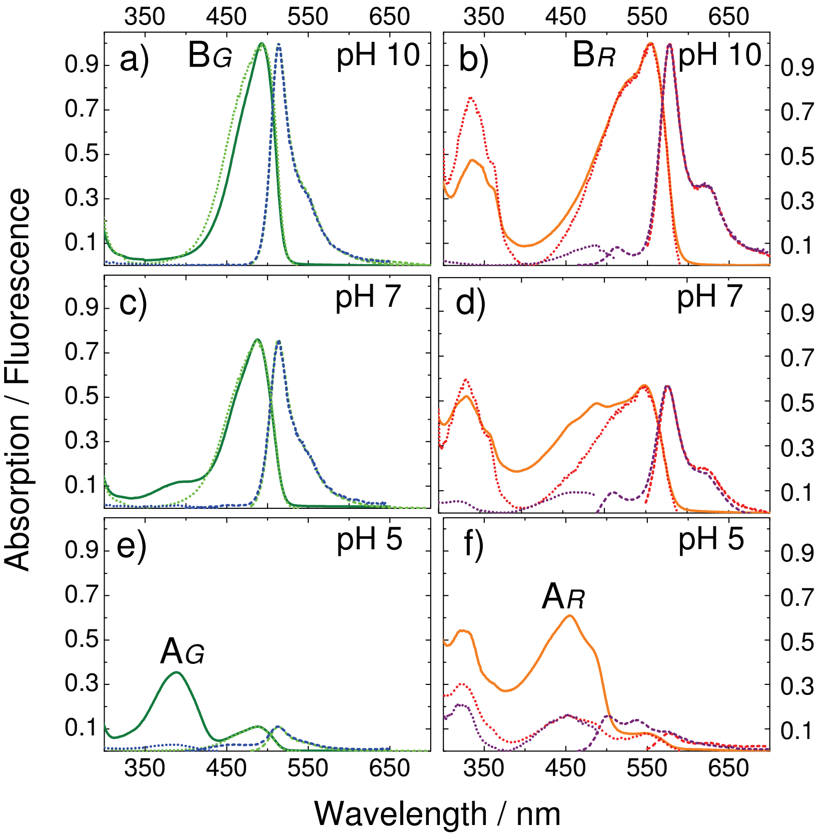

Figure 4.7: Spectral changes of IrisFP upon pH variation. Absorption (solid), excitation (dotted) and emission (dashed) spectra of (a,c,e) green and (b,d,f) red IrisFP at (a,b) pH 10, (c,d) pH 7 and (e,f) pH 5. Fluorescence spectra recorded for the neutral form of green (red) IrisFP are depicted as blue (purple) lines. The emission spectra were excited at 390 (455) nm and the excitation spectra were recorded for emission at 450 (500) nm. The fluorescence spectra of the anionic form of green (red) IrisFP are depicted as green (red) lines. The emission spectra were excited at 480 (540) nm and the excitation spectra were recorded for emission at 540 (600) nm. Absorption spectra are shown in dark green and orange lines for green and red IrisFP, respectively. Spectra recorded at pH 10 were scaled to equal amplitudes, whereas spectra recorded at lower pH were scaled to the ratio of the B_c^G (B_c^R)-band amplitude at the particular pH to its amplitude at pH 10, calculated from the respective pK_a value.

4.3 Photoactivation in IrisFP

IrisFP combines several photoactivation modes in response to illumination at particular wavelengths (Figure 4.8). The different light-induced transitions were investigated spectroscopically and the results are discussed referring to Figure 4.8 and interpreted with respect to the conclusions from X-ray analysis. The spectral changes concomitant with the structural rearrangements upon photoactivation are illustrated in Figure 4.9.

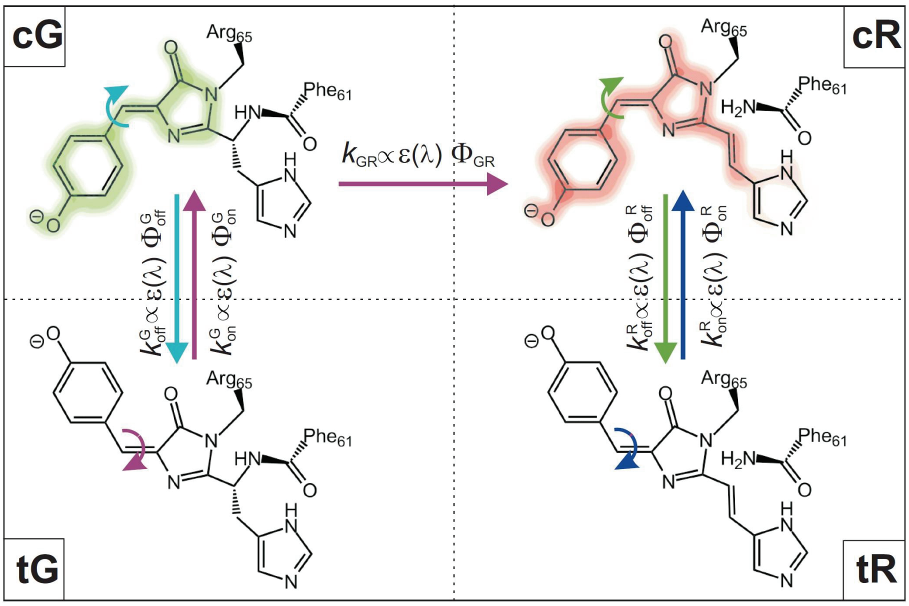
cG
cR
tG
tR
Arg65
Phe61
HN
H2N
$k_{GR} \propto \varepsilon(\lambda)\ \Phi_{GR}$
$k_{off}^{G} \propto \varepsilon(\lambda)\ \Phi_{off}^{G}$
$k_{on}^{G} \propto \varepsilon(\lambda)\ \Phi_{on}^{G}$
$k_{off}^{R} \propto \varepsilon(\lambda)\ \Phi_{off}^{R}$
$k_{on}^{R} \propto \varepsilon(\lambda)\ \Phi_{on}^{R}$

Figure 4.8: Photoinduced transformations in IrisFP. Schematic structures of the different chromophore forms. The *cis* and *trans* chromophores of the green and red forms of IrisFP are represented by cG / tG and cR / tR, respectively. The curved arrows indicate the direction of the photoinduced structural motions. The color coding represents the wavelength of the triggering excitation wavelengths 405 nm (violet), 488 nm (cyan), 440 nm (blue) and 532 nm (green). The rate coefficients of a particular reaction depend on the quantum efficiency and the extinction coefficient.

4.3.1 General Aspects of Photoswitching

In addition to green-to-red photoconversion, IrisFP undergoes reversible photoswitching. Here, a brightly fluorescent state is switched into a dark state and vice versa (Figure 4.12). Structurally, this transition was assigned to *cis*-*trans* isomerization of the chromophore and the concomitant structural reorientation of several

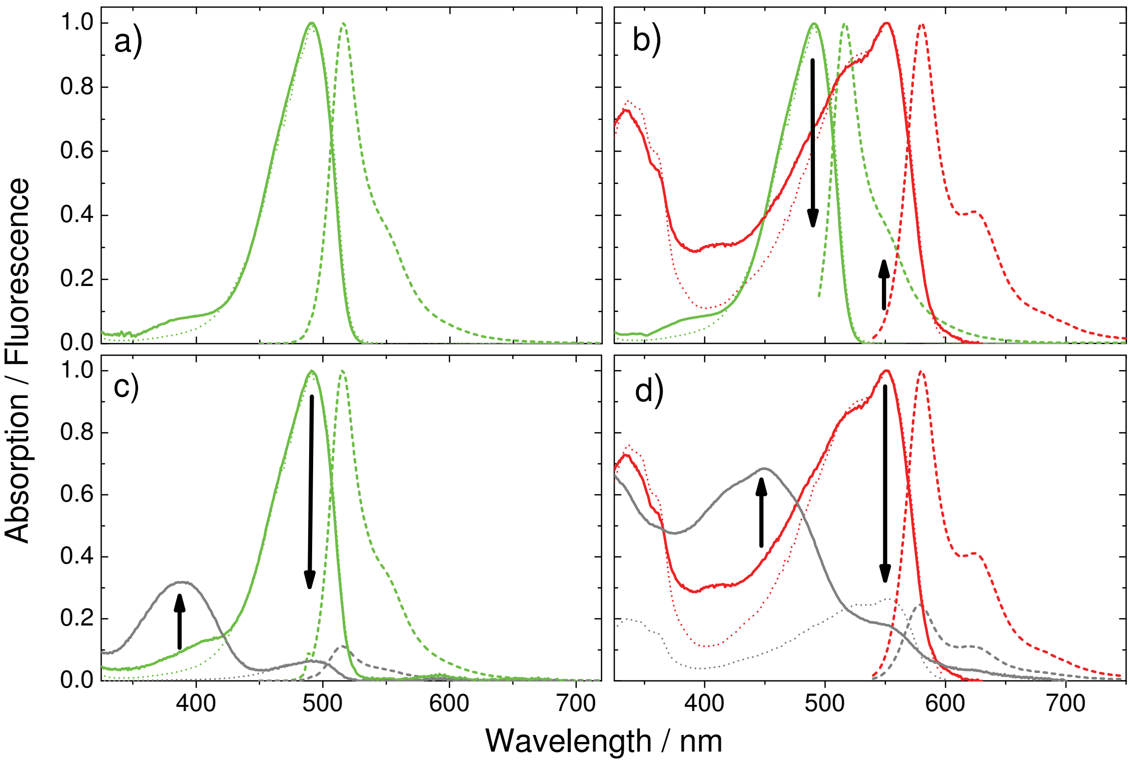

Figure 4.9: Spectroscopic changes upon photoactivation. Absorption, excitation, and emission spectra scaled to equal maximum amplitudes are depicted by solid, dotted, and dashed lines, respectively. Emission spectra of green (red) IrisFP were obtained by exciting at 440 (530) nm. Excitation spectra of green (red) IrisFP were obtained by detecting emission at 560 (620) nm. (a) Thermally relaxed green form of IrisFP. (b) Red IrisFP (red) after photoconversion of green IrisFP (green) with 405-nm light. (c) Green IrisFP before (green) and after (gray) illumination with 488-nm light. (d) Red IrisFP before (red) and after (gray) illumination with 532-nm light. All spectra were recorded on solution samples in 100 mM carbonate buffer, pH 9. The spectra were redrawn from Adam *et al.*[120].

amino acids in the chromophore vicinity. Photoswitching occurs in both the green and red forms of IrisFP. By exciting the bright green form (cG) with 488-nm light, the emission intensity decays rapidly (off switching) with a quantum efficiency of 0.014 ± 0.004 at pH 7. This is accompanied by a proportional decay of the absorption B_c^G band. Simultaneously, a neutral chromophore band emerges at $\sim 390\,\text{nm}$ (A_t^G), which is assigned to the *trans* chromophore (tG).

The neutral protonation state of the *trans* chromophore is most likely caused by its proximity to Glu144. The negative charge of its side chain impedes deprotonation of the *trans* chromophore and, therefore, maintains it in a neutral state (Section 4.1.1). The exchange between the B_c^G and A_t^G bands results in a crisp isosbestic point at 426 nm, indicating a two-state-transition between *cis* and *trans* chromophore isomers. The metastable dark state tG has a lifetime of ~476 min at ambient temperature and pH 7 (Figure 4.10).

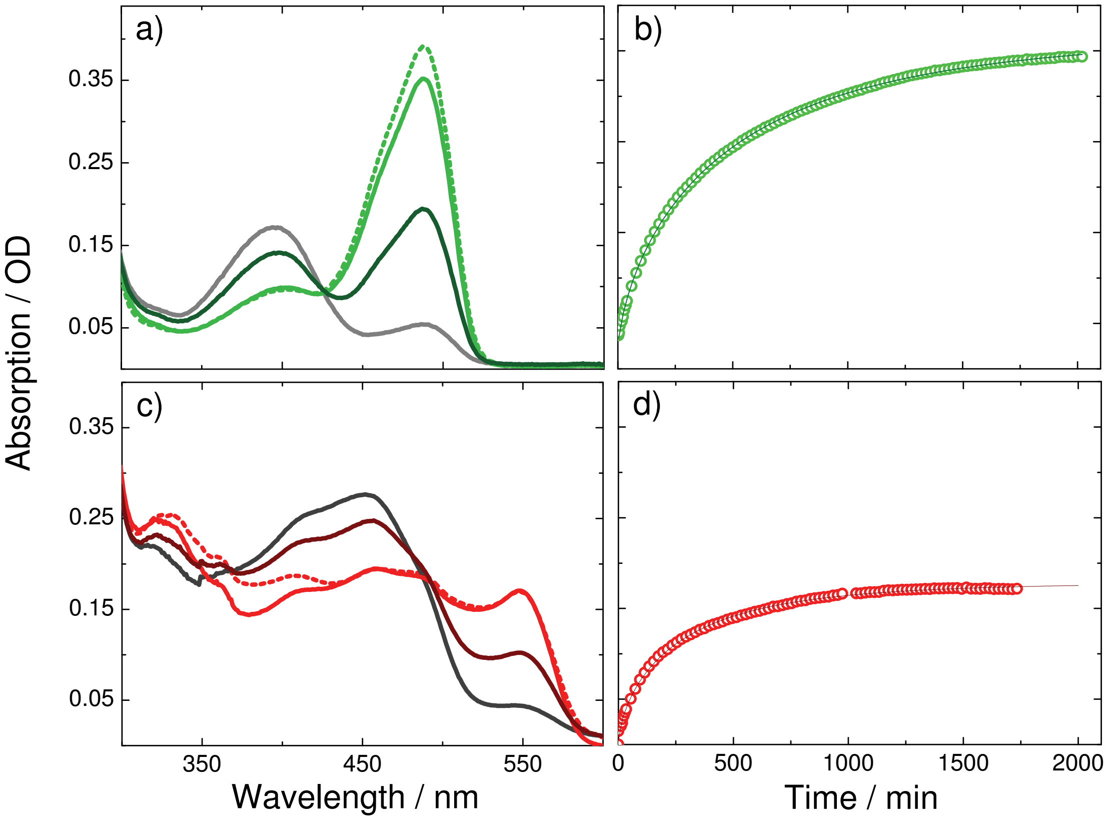

Figure 4.10: Thermal recovery of IrisFP. Absorption spectra of (a) the green and (b) the red forms of IrisFP before off-switching (green (red) dashed line) and after off-switching (solid lines), and after 0 h (gray (dark gray)), 4.5 (2.5) h (dark green (dark red)) and 63 (32) h (green (red)) in the dark. Absorption during recovery in the dark of (c) the green and (d) the red forms of IrisFP at 490 (550) nm. The experiment was performed at pH 7 and ambient temperature.

The recovery of the original absorption spectrum and emission intensity, assigned to cG, can be strongly accelerated by illumination with 405-nm light, which excites tG in the A_t^G band (on switching). The on switching process is 35-fold more efficient than off switching ($\phi^{G}_{on} = 0.5$, $\phi^{G}_{off} = 0.014$; Figure 4.11). These off/on switching cycles can be repeated many times (Figure 4.12).

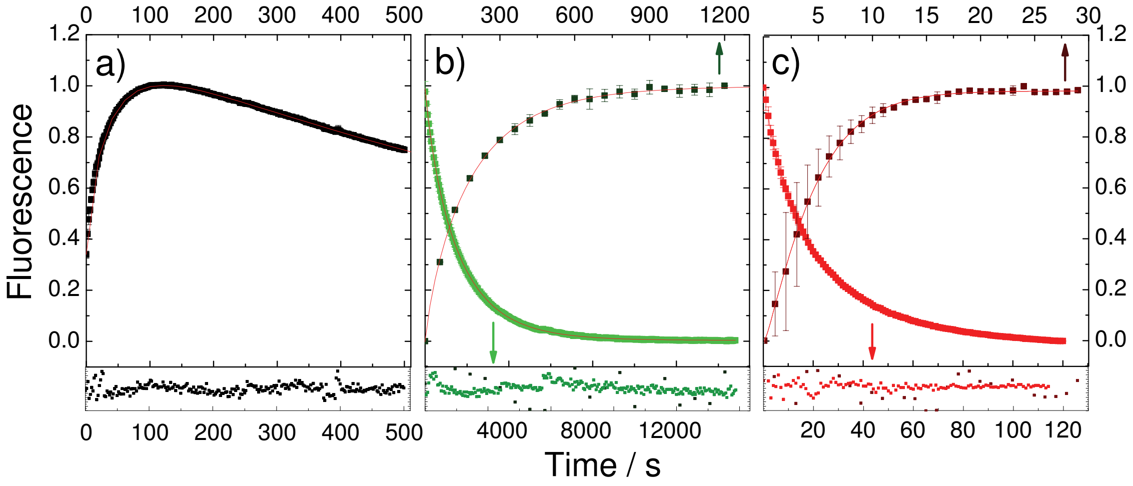

Figure 4.11: Time traces of IrisFP photoactivation. Mean time traces of at least three measurements, performed at ambient temperature at pH 7. (a) Green-to-Red photoconversion monitored via emission at 580 nm, induced by 405-nm illumination (2 mW cm^{-2}). Photoswitching of (b) the green and (c) the red forms of IrisFP; off-switching (green (red)) induced by 10 µW cm^{-2} (49 mW cm^{-2}) 488 (561)-nm light and on-switching induced by 9 µW cm^{-2} (31 mW cm^{-2}) 405 (440)-nm light. Fluorescence was monitored at 520 nm and 600 nm for green and red IrisFP, respectively. The time traces were fitted with a stretched exponential function. The residuals of the fits are represented as colored symbols below the respective panels.

Switching of the red form of IrisFP is similar to that of the green form. Off switching of the bright emissive state (cR) occurs through excitation within the B^{R}_{c} band by 532- or 561-nm light. During off switching, the B^{R}_{c} band decreases, while a broad neutral one arises at ~450 nm (A^{R}_{t} band) indicating a *cis*-to-trans isomerization, cR → tR. The exchange from the B^{R}_{c} into the A^{R}_{t} absorption band is accompanied by a decrease of the emission intensity at 580 nm (cR). The red dark *trans* isomer tR is somewhat less stabilized than the green dark *trans* isomer tG, with a lifetime of ~277 min. Exciting in the A^{R}_{t} band with 440-nm light strongly accelerates the recovery to the bright state cR. The phototransitions occur with a quantum efficiency of $\phi^{R}_{off} = 0.002$ and $\phi^{R}_{on} = 0.047$ for off and on switching with 532-nm and 440-nm light, respectively (Figure 4.11). Surprisingly, these values are much lower than those determined for photoswitching of the green chromophore, although the structural similarities in the chromophore pocket of the green and the red forms give no indication of differences in the photoswitching mechanism. However, both of the utilized switching wavelengths excite both chromophore species involved in the photoisomerization reactions, namely the red anionic *cis* cR and the red neutral *trans* chromophore tR. Thus, the excitation wavelength triggers photoswitching in both directions, i. e. off and on switching compete. The rate coefficients of the individual processes correlate with the excitation probabilities of the reactants, thus, the extinction coefficients of cR and tR at 532 nm and 440 nm, respectively. Hence, the observed rate coefficient presents the sum of off and on switching reaction, which results in a reduced quantum efficiency.

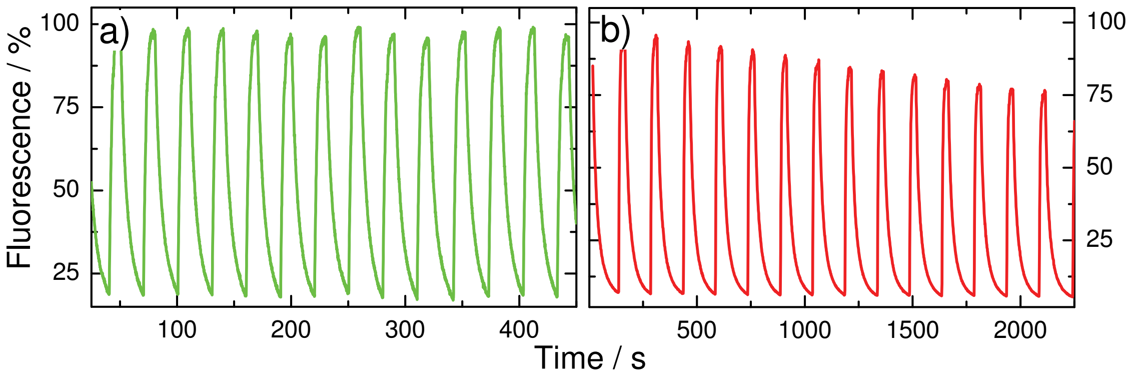

Figure 4.12: Photoswitching cycles of IrisFP. (a) Green IrisFP diluted in 0.1 M bicine (pH 9). The sample was exposed to continuous illumination with 488-nm light (50 mW cm^{-2}), while 405-nm light (37 mW cm^{-2}) was switched on every 30 s for 10 s. (b) Red IrisFP diluted in 0.1 M potassium-phosphate (pH 7) was exposed to continuous illumination with 561-nm light (49 mW cm^{-2}), while 440-nm light (31 mW cm^{-2}) was switched on every 120 s for 30 s. The figure is reproduced from Adam *et al.*[120].

4.3.2 Green-to-Red Photoconversion

Intense irradiation exciting the neutral green chromophore (cG, $\lambda_{\max} = 389$ nm) triggers the extension of the chromophore π-electron system by a β-elimination reaction[120] and, therefore, induces a red shift in the emission (cR, $\lambda_{\max} = 580$ nm). Still, at room temperature, 390-nm illumination of a 0.3 µM protein solution of IrisFP (pH 7) initially results only in an ~30 % increase of the emission intensity at 580 nm (Figure 4.13 a). Upon extended illumination, the green emission intensity decreases, which may be a result of protein degradation and / or conversion to a non-emitting state. Due to the spectral overlap of the emission bands of the green and red anionic species, the emission intensity at 580 nm represents the sum of the emission of both forms (Figure 4.9 b). Thus, a loss of emission intensity might originate from a decrease in green and / or red fluorescence. Indeed, the emission band of green IrisFP (cG) was reduced to less than 10 % of its original amplitude by 390-nm illumination (Figure 4.13 b), which does not correlate with the small gain in 580 nm emission (cR) due to green-to-red photoconversion and, hence, implies that dark, non-emitting species are generated. In the dark, a very slow fluorescence increase was observed at 580 nm (Figure 4.13 a). Simultaneously, the intensity of the emission bands of the green and red forms recovered, indicating a thermal relaxation of the non-emitting dark states back to the fluorescent states (Figure 4.13 c).

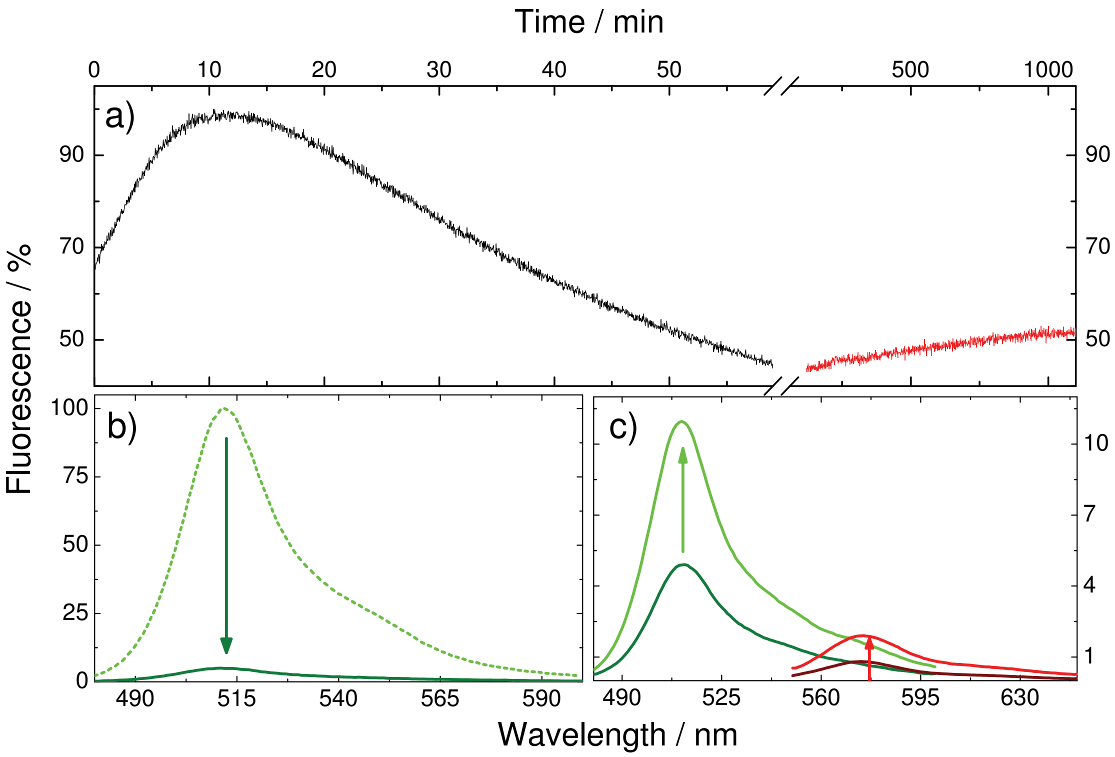

Figure 4.13: Photoconversion in IrisFP and its side effects. (a) Emission intensity at 580 nm (black) during continuous exposure to 390-nm light and (red) during recovery, monitored by 540 nm excitation for 100 ms every 60 s. (b) Emission of the green form excited at 470 nm before (dashed) and after (solid) 405-nm illumination. The maximal emission was scaled to 100 % before 390-nm illumination. (c) Emission of green (red) IrisFP after 390-nm illumination (dark green (dark red)) and after 60 min in the dark (bright green (bright red)).

Obviously, continuous 390-nm illumination induced a reversible transition in both colors ($cG \rightleftharpoons tG$ and $cR \rightleftharpoons tR$; Figure 4.8). The green dark state (tG) is not subject to green-to-red photoconversion[120], thus the yield of red IrisFP is limited by the supply of cG. The fraction of cG depends on the equilibrium coefficient of the photoequilibrium between the bright green cG and the dark state tG during 390-nm illumination ($k_{\mathrm{on}}^{\mathrm{G}}/k_{\mathrm{off}}^{\mathrm{G}}$, Figure 4.8). Overall, the green-to-red photoconversion in IrisFP is compromised by the competition between the reversible ($cG \rightleftharpoons tG$) and irreversible photoactivation pathways ($cG \rightarrow cR$). Even so, during $\sim 16\,\mathrm{h}$ in the dark, green emission recovered to only $\sim 20\,\%$ of the original fluorescence, which indicates that the bigger part of the protein actually degrades. For higher protein concentrations, the protein sample even got cloudy during exposure to 390-nm light, and aggregated, denatured protein precipitated.

The quantum efficiencies of the individual chromophore reactions are compiled in Table 4.2.

Table 4.2: Photoactivation properties of IrisFP^a.

Parameter	green IrisFP	red IrisFP
ϕ_{GR}	0.0018	—
$\phi_{\mathrm{off}}{}^a$	0.014	0.002
$\phi_{\mathrm{on}}{}^a$	0.5	0.047
$\mathrm{Efficiency_{off}}{}^b$	$\sim 85\,\%$	$\sim 75\,\%$
τ_{rec}, min	476	277

[a] Standard deviation $\sim 25\,\%$

[b] Switching efficiencies based on the following illumination conditions: Green IrisFP: 473 nm, 40 mW, $\sim$10 min. Red IrisFP: 532 nm, 50 mW, $\sim$10 min.

4.3.3 Modulation of Irreversible and Reversible Photoactivation Modes

Reversible photoswitching of green and red IrisFP are linked by irreversible photoconversion (Figure 4.9). The choice of the different photoactivation pathways is governed by the probability of inducing one process over the other. Below, we discuss the influence of the individual photoactivation pathways upon illumination with light of a particular wavelength.

A solution of green IrisFP at pH 7 contains a mixture of neutral and anionic chromophores (A_c^G and B_c^G bands). Exciting one of these chromophore species might preferentially result in off switching *or* green-to-red photoconversion. We investigated the yields of these photoactivation pathways by evaluating the relative changes in the integrated emission intensities compared to the initial emission achieved by illuminating the sample with light of a particular wavelength for 300 s (Figure 4.14). Emission of the green and red form was recorded for excitation at 470 nm and 540 nm, respectively (see Section 3.4 for details).

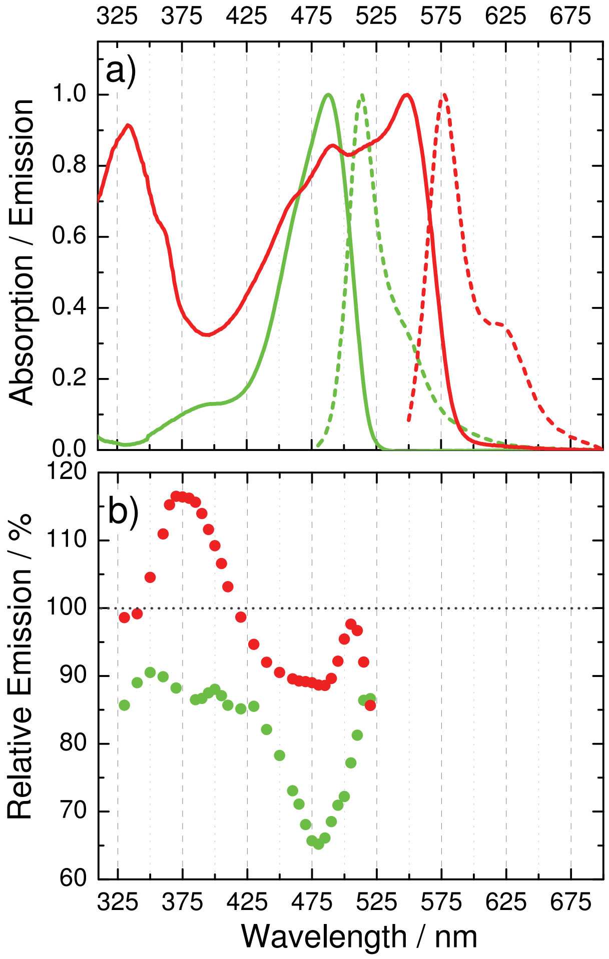

Figure 4.14: Action spectra of IrisFP. (a) Superposition of absorption (solid) and emission spectra (dotted) of green (green) and red (red) IrisFP. (b) The relative change of the integrated emission intensity compared to the initial one (100 %) is plotted against the respective wavelength. Emission spectra of green (red) IrisFP were recorded before and after illumination for 300 s by 470 (540)-nm excitation between 480-700 (550-750) nm.

The choice of the excitation wavelengths ensures excitation of either green (470 nm) or red emission (540 nm). Thus, changes in the emission intensity of green and red IrisFP can be determined independently. The extent of these changes are a measure for the probabilities of the individual photoactivation process upon illumination with a particular wavelength. The relative emission change plotted against the excitation wavelength are here termed action spectrum.

The action spectrum of green IrisFP shows a decrease of green emission for excitation in the whole spectral range of IrisFP absorption, but is maximal for excitation in the green anionic absorption band ($\mathrm{B_c^G}$). The fraction of red IrisFP increases upon excitation of the green neutral chromophore within the $\mathrm{A_c^G}$ band. At higher wavelengths, the red emission decreases. The wavelength dependence appears to match the absorption band of the red neutral chromophore, $\mathrm{A_c^R}$. Here, we note that the IrisFP solution used for this experiment contained already photoconverted red protein ($>1\,\%$). The decrease of the red emission apparently represents the off switching of this protein fraction via exciting the neutral red chromophore.

Photoactivation by Excitation in the Spectral Range of the Green Neutral Chromophore

Upon photoconversion the red emission band gains intensity at the expense of the green emission band. Red IrisFP is 30 % less bright than the green form (cG: $\phi_{\mathrm{fl}}\,\varepsilon_c$ =21,800 ± 1,800; cR: $\phi_{\mathrm{fl}}\,\varepsilon_c$ =15,000 ± 2,000). We would therefore expect that the red emission intensity increases by $\sim 70\,\%$ of the emission intensity lost in the green band, if green-to-red photoconversion would be the only cause for the decrease in the green emission band during $\sim$390-nm illumination. However, the increase in red emission effectively observed during this process presents $>1\,\%$ of the expected value. Thus, we have to conclude that the loss in green emission intensity upon excitation in $\mathrm{A_c^G}$ is partially due to off switching, as already suggested in Section 4.3.2. The large difference between expected and experimental value emphasizes that off switching is a much more efficient process than green-to-red photoconversion. Consequently, the green chromophore exists partially in the dark state (tG) during 390-nm illumination. In Section 4.3.1, we have described that excitation in the $\mathrm{A_t^G}$ band (e.g. at $\sim$390 nm) results in recovery of the bright state, cG (on switching). These observations seem to contradict. However, excitation by $\sim$390 nm illumination potentially triggers three different photoreactions (Figure 4.15): (i) off switching by *cis*-to-*trans* isomerization of the green neutral *cis* chromophore (cG → tG), (ii) on switching by *trans*-to-*cis* isomerization of the neutral *trans* chromophore (tG → cG) and (iii) green-to-red photoconversion of the green neutral *cis* chromophore (cG → cR).

Thus, the situation at physiological pH presents itself as the following. The

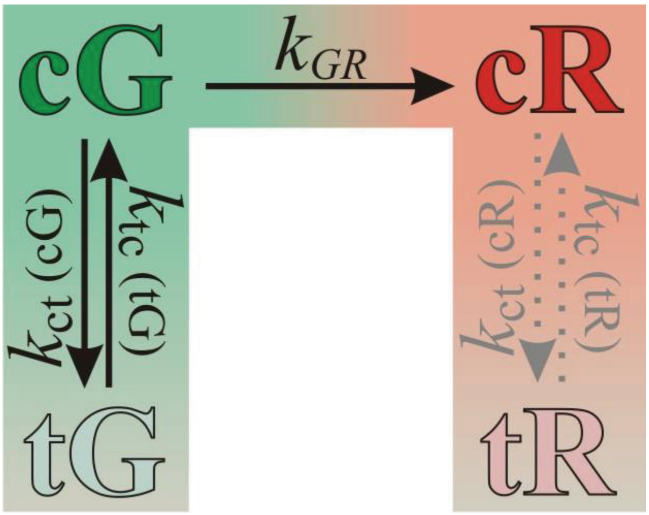

Figure 4.15: Schematic illustration of the photoreaction during 390 nm-illumination. cG (cR) and tG (tR) represent the green (red) chromophore in the *cis* and *trans* conformation, respectively. The rate coefficients for the individual transitions differ significantly. The transitions between cR and tR (gray arrows) do not contribute to the yield of green-to-red photoconversion. The color coding indicates the shift in emission color and intensity.

neutral *cis* chromophore, cG, shows maximum absorption at 390 nm (A_c^G). Its excitation induces reaction (i), *cis*-to-*trans* isomerization to the green dark state, tG, with A_t^G peaking at 388 nm. Simultaneously, 390-nm illumination induces reaction (ii), on switching to the green *cis* state that occurs with a quantum efficiency of 0.5. Since reaction (i) and (ii) are induced concurrently by 390-nm light illumination, these processes converge towards a light-induced equilibrium governed by the rate coefficients of the individual reactions (k_{tc}/k_{ct}). Reaction (iii), green-to-red photoconversion, occurs also by excitation of the green neutral *cis* chromophore ($\phi_{GR} = 1.8 \times 10^{-3}$)[116,120]. During this reaction, the chromophore transforms irreversibly to cR. Thus, cG is depopulated and the light-induced equilibrium between cG and tG has to readjust, resulting in depopulation of tG. Complete photoconversion should therefore be possible upon long-term illumination. However, red anionic IrisFP is also excited by 390-nm illumination (Figure 4.14 a). Thus, even already photoconverted, red IrisFP is due to a photoinduced equilibrium between the bright red *cis* isomer, cR, and the dark red *trans* isomer, tR. Therefore, the red emission intensity may decrease. The photoinduced equilibria between the on- and off-states of the green and the red forms, however, are governed by the respective extinction coefficients of the involved species, and the reaction probabilities upon photoexcitation, i.e., the quantum efficiency of the respective process. We have observed that long-term illumination of IrisFP results also in irreversible damage of the protein (Section 4.13), thus, complete photoconversion to the red state is not possible. Overall, the yield of green-to-red photoconversion is determined by the availability of the reactant of photoconversion, i.e. neutral *cis* chromophore (cG), which is governed by the ratio of the rate coefficients of off (cG → tG) to on switching (tG → cG) upon ~ 390-nm illumination.

4.4 Summary and Conclusions

In EosFP, the mutation of Phe173 to serine is sufficient to introduce the photoisomerization ability. The smaller Ser173 enables reorientation of the Met159 side chain, which creates free space around the chromophore and, thereby, increases its flexibility. However, this additional space is not a strict requirement for photoswitching. In other photoswitchable FPs, e.g., Dronpa[122,127], mTFP0.7[128] and asFP595[49], the chromophore is much more restrained. Even so, the additional space clearly accelerates the photoswitching kinetics, a phenomenon that is also observed in the Dronpa variant Met159Thr[127] and the mEosFP*thermo* variant Met159Cys (unpublished data).

Upon photoisomerization to the *trans* state, we observe concurrent structural rearrangements of several amino acids within the chromophore pocket. Similar rearrangements were observed also for photoisomerization in Dronpa[122,127] and mTFP0.7[128], which have essentially the same amino acids in the chromophore vicinity. Glu212 is a remarkable exception. While this amino acid does not change its conformation in Dronpa and mTFP0.7, it flips ~ 90° around the C_α of the side chain in IrisFP. Glu212 is supposedly involved in the green-to-red photoconversion, acting as an acid-base catalyst[34]. In consequence of the flip of its side chain, the carbonyl group is too far away from the C_β of the His62 side chain for fulfilling this catalytic role. We therefore suggest that the *trans* chromophore is not subject to green-to-red photoconversion upon 400-nm illumination, but rather photoisomerizes to the *cis* state. Furthermore, considering the quantum efficiencies of the individual photoactivation pathways, *trans*-to-*cis* isomerization is much more likely than green-to-red photoconversion. These two reactions compete during 400-nm illumination, resulting in a complete depletion of green *trans* chromophore by recovery of the *cis* state before green-to-red photoconversion of the *trans* chromophore could occur to any appreciable extent.

Owing to the spectral overlap of the different chromophore species in IrisFP, a competition between the different photoactivation reactions is hardly avoidable. However, the different excitation probabilities of the individual chromophore species at a specific wavelength and the different quantum efficiencies of the individual photoreactions permit the preferential selection of one process over the other. Even so, the experimental conditions, e.g. excitation wavelength and power density, have to be considered carefully to achieve maximal efficiency of the selected process.

Despite these challenges, IrisFP is the first protein that combines reversible photoswitching with irreversible green-to-red photoconversion and, therefore, potentially enables a variety of new applications. Applications such as read-only and rewritable optical data storage take advantage of the multiple phototransformations in IrisFP[140]. Furthermore, the recently introduced superresolution imaging techniques will benefit from its multifunctionality by permitting new experimental designs. Unfortunately, IrisFP is a tetrameric protein, which limits its applicability as a fusion tag, since oligomerization of the fusion tag may affect the localization dynamics and function of the target protein and, therefore, give rise to artifacts in the experiment.

Chapter 5

A Genetic Label with Multiple Photoactivation Modes – mIrisFP

5.1 Introduction

Photoactivation enables highlighting of a protein subpopulation within a distinct area of a cell. This phenomenon turned PAFPs into very useful tools for pulse chase experiments, in which the movements of a protein subpopulation is followed over time[141,142], or for superresolution light-microscopy methods, in which highlighting of single molecules allows the diffraction barrier to be surpassed[9,136]. However, photoactivation can be used either for pulse-chase experiments or superresolution imaging. IrisFP combines three different photoactivation modes, irreversible green-to-red photoconversion and reversible photoswitching between a bright fluorescent and a dark state in the green and red forms. Therefore, it potentially allows for combination of pulse chase experiments with superresolution. To avoid problems due to the tetrameric nature of IrisFP, we have generated a monomeric variant, mIrisFP, using a semi-rational engineering approach, which combines knowledge-based site-directed and random mutageneses. The engineering history of mIrisFP, its photophysical properties and its applications are discussed below.

5.2 Semi-rational Engineering of mIrisFP

5.2.1 Molecular Engineering

We started engineering of mIrisFP with a monomeric EosFP variant as a template, mEosFP*thermo*[118]. It was monomerized by substitution of Val123 with a threonine and of Thr158 with a histidine. Previous studies identified the Phe173Ser mutation as crucial for introducing the photoswitching properties into EosFP. We therefore implemented this mutation in mEosFP*thermo* by site-directed mutagenesis, which resulted in the variant mEosFP*thermo* Phe173Ser (mIrisGFP). In bulk experiments, we observed no significant green-to-red photoconversion for this variant, which is described in detail in Chapter 6. To recover the green-to-red photoconversion functionality, we performed error-prone mutagenesis and screened for variants that developed red color during continuous illumination with weak UV-light. The most promising variant exhibited a single additional mutation, Lys145Ile (Figure 5.1).

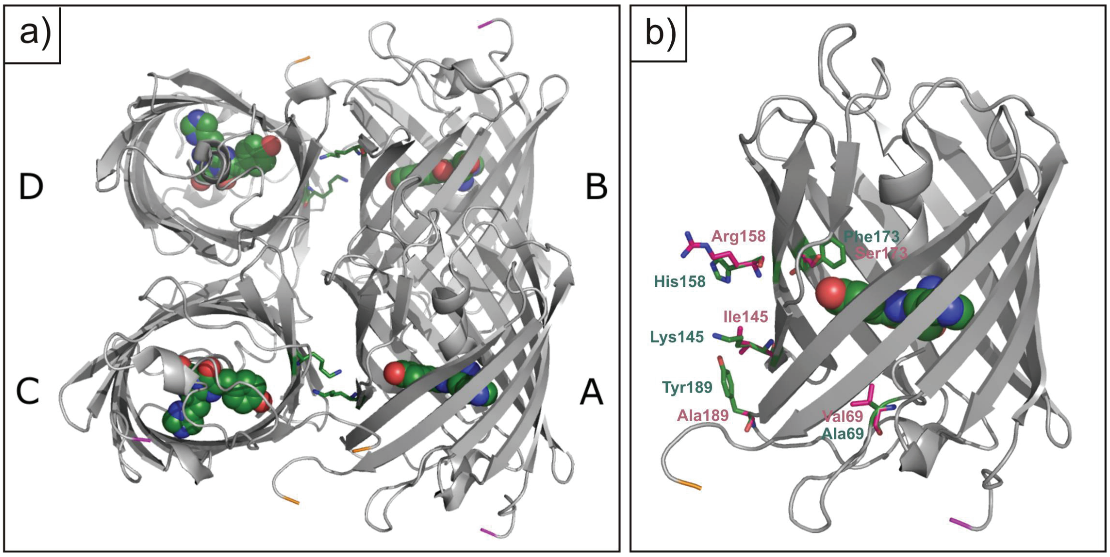

Figure 5.1: Structural changes in mIrisFP. a) Definition of the AB and AC interfaces between the monomer subunits in EosFP. N' and C' termini were colored in orange and purple, respectively, for better orientation. The chromophore is highlighted as spheres. Lys145 is represented by sticks. b) Amino acid substitutions between mEosFP (PDB code: 1ZUX) and mIrisFP are indicated by green and magenta sticks, respectively. In the model, amino acids were exchanged using *PyMOL*$^{\mathrm{TM}}$(DeLano Scientific LLC, 2006) and are shown in the preferred conformation as suggested by the software.

Based on a gel filtration analysis of a 1-µM protein solution of mEosFP*thermo* Lys145Ile, Phe173Ser we determined the molecular mass of this variant as ∼ 48 kDa, which represents a dimer. Dimerization of mEosFP*thermo* Lys145Ile, Phe173Ser is most likely based on the removal of electrostatic repulsion expected between the Lys145 side chains of two interacting protomers in the A/C interface (Figure 5.1).

In previous studies[34], we had identified two different mutations at position 158, which were sufficient to interrupt the A/C interface in EosFP, namely Thr158His and Thr158Arg (Figure 5.1 a). The mEosFP*thermo* template carries the Thr158His mutation. To check if the Thr158Arg mutation has a stronger impact on the A/C interface, we exchanged His158 with an arginine. The molecular mass of the resulting variant, mEosFP*thermo* Lys145Ile, His158Arg, Phe173Ser was estimated as ~ 39 kDa at 1 µM concentration, which indicates a reduced dimerization tendency compared to its predecessor, but that still left room for further improvement.

Sequence alignment of several monomeric FPs, generated from predecessor proteins, which were originally isolated from anthozoa, indicated that the amino acid at position 189 might influence the integrity of the A/C interface. While these monomeric FPs typically feature a small aliphatic amino acid at the specified position, mainly alanine, mEosFP*thermo* Lys145Ile, His158Arg, Phe173Ser exhibits a tyrosine at position 189 instead (Figure 5.2). Consequentially, we exchanged Tyr189 by an alanine and this mutation finally resulted in mIrisFP (mEosFP*thermo* Lys145Ile, Thr158Arg, Phe173Ser, Tyr189Ala).

Size-exclusion chromatography analysis yielded a molecular mass of ~ 23 kDa in a 1 µM protein solution, as expected for a monomer. The monomer-dimer transition occurs with a dissociation coefficient K_D of 32 ± 3 µM and a Hill coefficient of 1.3 ± 0.1, which suggests an increase of the A/B-interface affinity upon dimerization via the A/C interface (Figure 5.3). The K_D is well above the intracellular concentration typical of transgenic protein expression[143]. Hence, mIrisFP is a promising genetically encodable marker, which also features multiple photoactivation pathways and has excellent fluorescence properties, which will be discussed below.

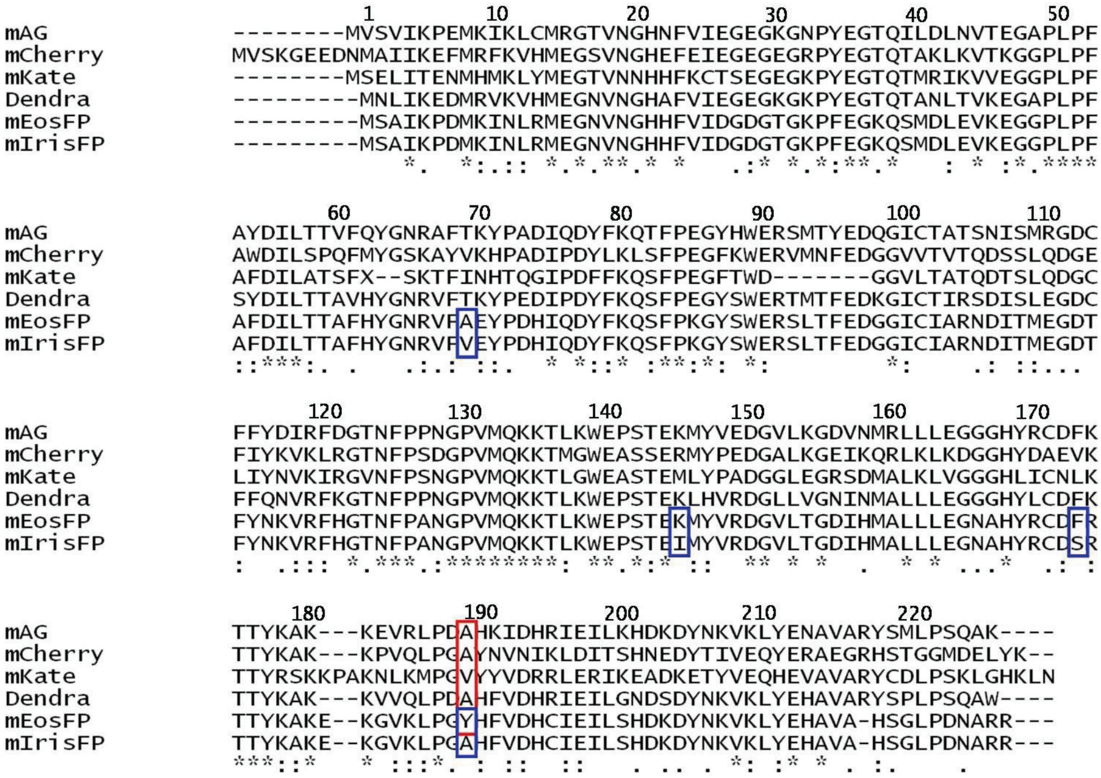

```
                     1       10        20        30        40        50
mAG         --------MVSVIKPEMKIKLCMRGTVNGHNFVIEGEGKGNPYEGTQILDLNVTEGAPLPF
mCherry     MVSKGEEDNMAIIKEFMRFKVHMEGSVNGHEFEIEGEGEGRPYEGTQTAKLKVTKGGPLPF
mKate       --------MSELITENMHMKLYMEGTVNNHHFKCTSEGEGKPYEGTQTMRIKVVEGGPLPF
Dendra      ---------MNLIKEDMRVKVHMEGNVNGHAFVIEGEGKGKPYEGTQTANLTVKEGAPLPF
mEosFP      ---------MSAIKPDMKINLRMEGNVNGHHFVIDGDGTGKPFEGKQSMDLEVKEGGPLPF
mIrisFP     ---------MSAIKPDMKINLRMEGNVNGHHFVIDGDGTGKPFEGKQSMDLEVKEGGPLPF
                        *.  *:.:: *.*.**.* *   .:* *.*:**.*   : * :*.****

                  60        70        80        90       100       110
mAG         AYDILTTVFQYGNRAFTKYPADIQDYFKQTFPEGYHWERSMTYEDQGICTATSNISMRGDC
mCherry     AWDILSPQFMYGSKAYVKHPADIPDYLKLSFPEGFKWERVMNFEDGGVVTVTQDSSLQDGE
mKate       AFDILATSFX--SKTFINHTQGIPDFFKQSFPEGFTWD-------GGVLTATQDTSLQDGC
Dendra      SYDILTTAVHYGNRVFTKYPEDIPDYFKQSFPEGYSWERTMTFEDKGICTIRSDISLEGDC
mEosFP      AFDILTTAFHYGNRVFAEYPDHIQDYFKQSFPKGYSWERSLTFEDGGICIARNDITMEGDT
mIrisFP     AFDILTTAFHYGNRVFVEYPDHIQDYFKQSFPKGYSWERSLTFEDGGICIARNDITMEGDT
            ::***:. .   .:.: ::.  * *::* :**:*: *:        *:    .: ::...

                120       130       140       150       160       170
mAG         FFYDIRFDGTNFPPNGPVMQKKTLKWEPSTEKMYVEDGVLKGDVNMRLLLEGGGHYRCDFK
mCherry     FIYKVKLRGTNFPSDGPVMQKKTMGWEASSERMYPEDGALKGEIKQRLKLKDGGHYDAEVK
mKate       LIYNVKIRGVNFPSNGPVMQKKTLGWEASTEMLYPADGGLEGRSDMALKLVGGGHLICNLK
Dendra      FFQNVRFKGTNFPPNGPVMQKKTLKWEPSTEKLHVRDGLLVGNINMALLLEGGGHYLCDFK
mEosFP      FYNKVRFHGTNFPANGPVMQKKTLKWEPSTEKMYVRDGVLTGDIHMALLLEGNAHYRCDFR
mIrisFP     FYNKVRFHGTNFPANGPVMQKKTLKWEPSTEIMYVRDGVLTGDIHMALLLEGNAHYRCDSR
            :  .::: *.***.:********: **.*:* ::  ** * *  .  * * ...*  .: :

               180       190       200       210       220
mAG         TTYKAK---KEVRLPDAHKIDHRIEILKHDKDYNKVKLYENAVARYSMLPSQAK----
mCherry     TTYKAK---KPVQLPGAYNVNIKLDITSHNEDYTIVEQYERAEGRHSTGGMDELYK--
mKate       TTYRSKKPAKNLKMPGVYYVDRRLERIKEADKETYVEQHEVAVARYCDLPSKLGHKLN
Dendra      TTYKAK---KVVQLPDAHFVDHRIEILGNDSDYNKVKLYEHAVARYSPLPSQAW----
mEosFP      TTYKAKE--KGVKLPGYHFVDHCIEILSHDKDYNKVKLYEHAVA-HSGLPDNARR---
mIrisFP     TTYKAKE--KGVKLPGAHFVDHCIEILSHDKDYNKVKLYEHAVA-HSGLPDNARR---
            ***::*   * :::*. : ::  ::   . .. .  *: :* *  . :.    .
```

Figure 5.2: Amino acid sequence alignment of monomeric Azami Green (mAG), mCherry, mKate, Dendra, mEosFP and mIrisFP. Blue frames indicate the amino acid exchanges between mEosFP and mIrisFP. The red frame highlights position 189, which promotes dimer interface disruption. Sequences are numbered according to mIrisFP, gaps in the sequence are indicated by dashes. '*' indicates sequence identity, ':' strong similarity and '.' weak similarity.

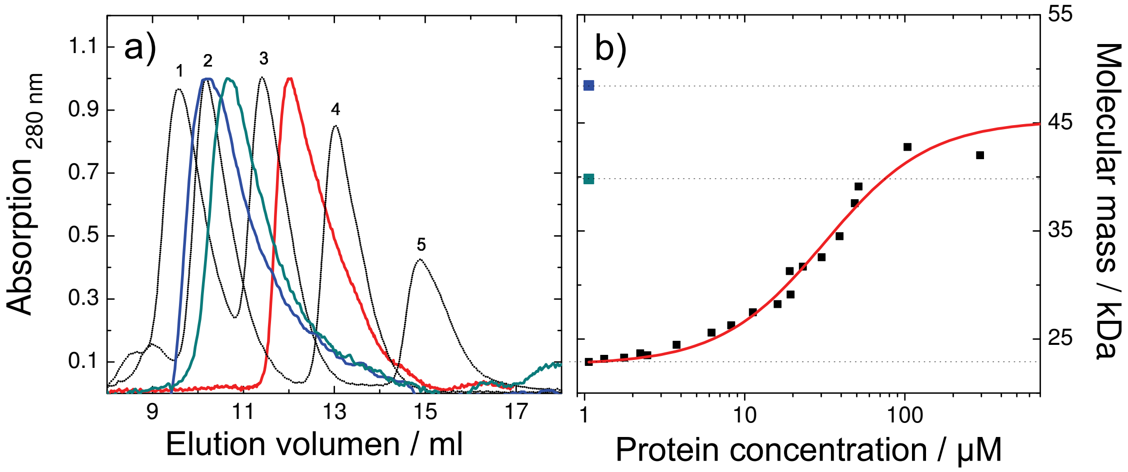

Figure 5.3: Oligomerization of mIrisFP and its predecessors. Size exclusion chromatography of mIrisFP (in 0.1 M sodium phosphate buffer, pH 7) with a Superdex 75 10/300 GL column. (a) Elution profiles of the reference proteins (black), mEosFP*thermo* Lys145Ile, Phe173Ser (blue), mEosFP*thermo* Lys145Ile, His158Arg, Phe173Ser (cyan) and mIrisFP (red). The column was calibrated, using conalbumin (1; 75 kDa), ovalalbumin (2; 43 kDa), carbonic anhydrase (3; 29 kDa), ribonuclease A (4; 13.7 kDa) and aprotinin (5; 6.5 kDa). (b) Molecular mass of mIrisFP (squares), as a function of protein concentration. The equilibrium dissociation coefficient is determined as $K_D = 32 \pm 3$ µM. Details of the procedure are described in Section 2.2.3. The molecular masses of mEosFP*thermo* Lys145Ile, Phe173Ser (blue) and mEosFP*thermo* Lys145Ile, His158Arg, Phe173Ser (cyan) in ~ 1 µM solution is shown for comparison.

5.3 Photophysical Characterization of mIrisFP

The spectral changes induced by photoactivation are very similar for mIrisFP and tetrameric IrisFP (Figure 5.4). Assuming that photoactivation in mIrisFP is based on identical structural changes as in the IrisFP tetramer, we can apply Figure 4.8 to describe its photophysical properties. The individual parameters are compiled in Table 5.1.

Table 5.1: Photophysical properties of IrisFP and mIrisFP[a] [118]

	green IrisFP	green mIrisFP
λ_{max} (Ex/Em), nm	488 / 516	486 / 516
ε_c (λ_{max}), $\mathrm{M}^{-1}\,\mathrm{cm}^{-1}$	$50{,}800 \pm 2{,}000$	$47{,}000 \pm 2{,}700$
ϕ_{fl}	0.43 ± 0.02	0.54 ± 0.04
Brightness	$28{,}600 \pm 2{,}400$	$25{,}500 \pm 3{,}300$
ϕ_{off}	0.014 [b, c]	$(6.9 \pm 0.1) \times 10^{-3}$ [d]
ϕ_{on}	0.5 [b, e]	0.36 ± 0.02 [e]
ϕ_{GR}	1.8×10^{-3} [b, e]	$(0.74 \pm 0.1) \times 10^{-3}$ [e]
τ_{rec}, min	~ 480	~ 80

	red IrisFP	red mIrisFP
λ_{max} (Ex/Em), nm	551 / 580	546 / 578
ε_c (λ_{max}), $\mathrm{M}^{-1}\,\mathrm{cm}^{-1}$	$32{,}000 \pm 2{,}800$	~ 33,000
ϕ_{fl}	0.47 ± 0.02	0.59 ± 0.04
Brightness	$16{,}600 \pm 2{,}200$	~ 19,300
ϕ_{off}	0.002 [b, f]	$(3.1 \pm 0.4) \times 10^{-3}$ [g]
ϕ_{on}	0.047 [b, h]	0.28 ± 0.09 [i]
τ_{rec}, min	~ 280	~ 35

[a] All values were estimated in 20 mM buffer, 150 mM ionic strength.

[b] Standard deviations are estimated as about 25%.

[c] upon 488-nm illumination.

[d] upon 473-nm illumination

[e] upon 405-nm illumination

[f] upon 532-nm illumination

[g] upon 561-nm illumination

[h] upon 440-nm illumination

[i] upon 473-nm illumination

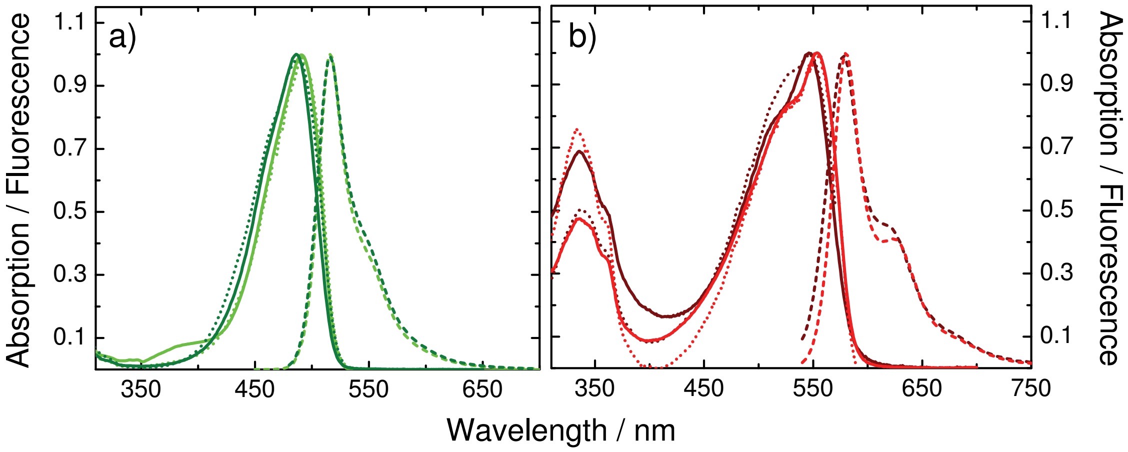

Figure 5.4: Absorption and fluorescence spectra of mIrisFP and IrisFP. Absorption (solid), emission (dashed) and excitation spectra (dotted) are shown for (a) the green and (b) the red form of mIrisFP (dark green (red)) and the IrisFP tetramer (bright green (red)). Spectra of mIrisFP were recorded at pH 10 with emission excited at 470 (530) nm excitation, respectively. Excitation spectra of the green and red forms were detected for emission at 540 (580) nm. Spectra of IrisFP tetramer were monitored at pH 9. Here, emission spectra of the green (red) form were recorded with 440 (530) nm excitation, respectively, whereas excitation spectra were detected for emission at 560 (620) nm.

5.3.1 The Thermally Relaxed Ground State

The thermally relaxed states of (i) green (cG, Figure 4.8) and (ii) red mIrisFP (cR) are subject to a protonation equilibrium, as described previously for IrisFP (Section 4.2). Deprotonation of the green mIrisFP chromophore occurs in two steps with $\mathrm{p}K_{a_1} = 5.0 \pm 0.1$ and $\mathrm{p}K_{a_2} = 6.8 \pm 0.1$ (Figure 5.5 a). The absorption spectrum of green mIrisFP shows a $\mathrm{B}_\mathrm{c}^\mathrm{G}$ band with maximum absorption at 486 nm and an $\mathrm{A}_\mathrm{c}^\mathrm{G}$ band with maximum absorption at 393 nm. The band shapes of both bands are almost identical to those of IrisFP. Green fluorescence of mIrisFP, which is maximal at 516 nm, is basically due to emission of the anionic chromophore, as indicated by the excitation spectrum recorded for emission at 540 nm. The extinction coefficient of the anionic chromophore ($\varepsilon_c\,(486\ \mathrm{nm}) = 47{,}000 \pm 2{,}700\ \mathrm{M}^{-1}\,\mathrm{cm}^{-1}$) and the fluorescence quantum yield ($\phi_\mathrm{fl} = 0.54 \pm 0.04$) demonstrate that the molecular brightness ($\varepsilon_c\,(486\,\mathrm{nm})\,\phi_\mathrm{fl} = 2.5 \times 10^{-3}$) is minimally affected by monomerization (IrisFP: $\varepsilon_c\,(488\,\mathrm{nm})\,\phi_\mathrm{fl} = 2.9 \times 10^{-3}$).

The absorption spectrum of red mIrisFP shows intense $\mathrm{A}_\mathrm{c}^\mathrm{R}$ and $\mathrm{B}_\mathrm{c}^\mathrm{R}$ bands at physiological pH. Chromophore deprotonation occurs in three steps ($\mathrm{p}K_{a_1} = 5.5 \pm 0.2$, $\mathrm{p}K_{a_2} = 7.3 \pm 0.2$, $\mathrm{p}K_{a_3} = 9.3 \pm 0.1$; Figure 5.5 b). The anionic red chromophore shows maximum absorption at 546 nm ($\mathrm{B_c^R}$, $\varepsilon_c\,(546\,\mathrm{nm}) \sim 33{,}000\ \mathrm{M^{-1}\,cm^{-1}}$) and maximum emission at 578 nm ($\phi_{\mathrm{fl}} = 0.59 \pm 0.04$). The absorption of the neutral chromophore peaks at 451 nm ($\mathrm{A_c^R}$, $\varepsilon_c\,(451\,\mathrm{nm}) \sim 24{,}000\ \mathrm{M^{-1}\,cm^{-1}}$); it shows only marginal fluorescence. As was observed previously for the IrisFP tetramer, both the anionic and neutral red chromophores feature an additional absorption band in the UV spectral range, centered on 319 nm and 332 nm, respectively.

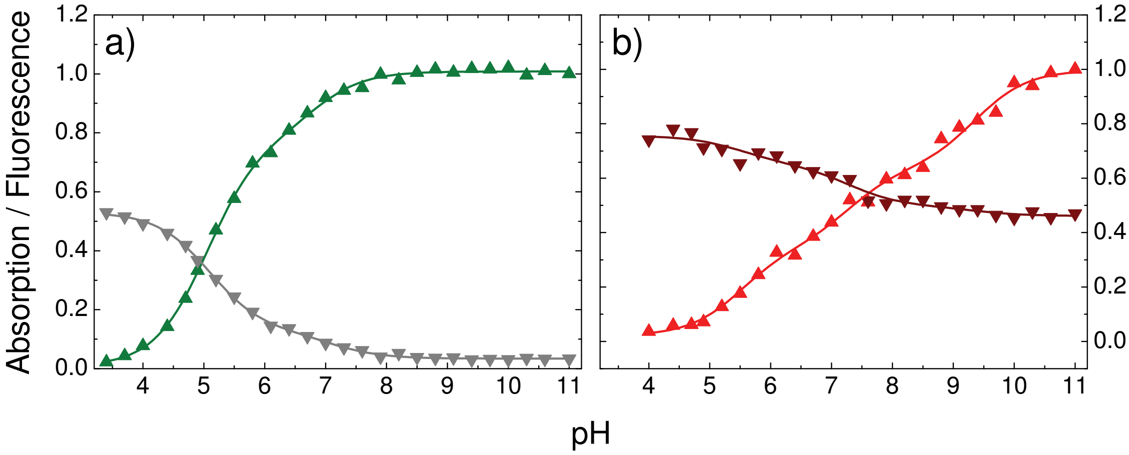

Figure 5.5: pH-dependence of the thermally relaxed mIrisFP. pH-sensitivity of (a) green and (b) red mIrisFP monitored via the relative fractions of neutral and anionic chromophore represented by the intensities of the absorption $\mathrm{A_c^G}$ ($\mathrm{A_c^R}$) (gray (bordeaux)) and $\mathrm{B_c^G}$ ($\mathrm{B_c^R}$) bands (green (red)). The absorption values are normalized relative to the amplitude of the $\mathrm{B_c^G}$ ($\mathrm{B_c^R}$) absorption band at pH 11. Experiments were performed with $\sim 3\,\mu\mathrm{M}$ protein solution at varying pH values. Buffer conditions are specified in Section 3.2.

5.3.2 Photoactivation

In bulk experiments, green-to-red photoconversion in mIrisFP is complicated by concomitant photoswitching. Additionally, we observe irreversible degradation of the protein during continuous illumination with 405-nm light. Time traces of the individual processes are depicted in Figure 5.6. Upon brief term illumination, however, photoconversion in mIrisFP is fast and yields a quantum efficiency of $\phi_{\mathrm{GR}} = 7.4 \times 10^{-4}$. Continuous illumination with 405-nm establishes a light driven equilibrium between green neutral *cis* and green neutral *trans* chromophores, $\mathrm{cG} \rightleftharpoons \mathrm{tG}$, which reduces the concentration of the available photoconverting species (cG). The competition between these two processes was explained in detail in Section 4.3.3 for the IrisFP tetramer. Very low intensities or stepwise photoconversion with longer dark periods, which would allow the protein solution to recover to the *cis* state, might increase the yield of photoconverted red protein.

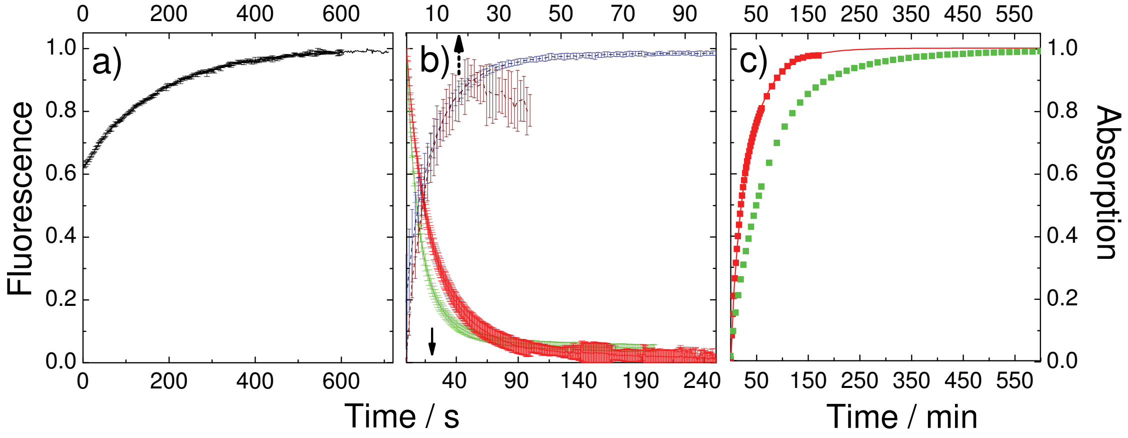

Figure 5.6: Time traces of photoactivation and thermal recovery in mIrisFP. Mean time traces of at least three measurements, performed at ambient temperature at pH 7. (a) Green-to-red photoconversion, induced by 405-nm illumination (60 mW cm^{-2}) via emission at 600 nm. (b) Off and on switching of the green (green (blue)) and red (red (bordeaux)) forms of IrisFP monitored via emission at 520 nm and 580 nm, respectively. Off switching was induced by 30 W cm^{-2} (55 mW cm^{-2}) 473 (561)-nm light, whereas on switching was induced by 0.5 mW cm^{-2} (5 mW cm^{-2}) 405 (473)-nm illumination. (c) Thermal recovery of green (green) and red (red) mIrisFP monitored via absorption at 490 nm and 550 nm, respectively. Time traces are scaled to the maximum values.

Thermally relaxed chromophores of both the green and red forms are in the *cis* conformation[120]. Excitation of either fluorescent species induces isomerization of the chromophore to the non-fluorescent *trans* conformation (cG/cR → tG/tR; $\phi_{\text{off}}^{\text{G}}\,(473\,\text{nm}) = (6.9 \pm 0.1) \times 10^{-3}$, $\phi_{\text{off}}^{\text{R}}\,(561\,\text{nm}) = (3.1 \pm 0.4) \times 10^{-3}$). The green and red *trans* chromophores show maximum absorption at 386 nm and 446 nm, with peak extinction coefficients of ~12,000 M^{-1} cm^{-1} and ~ 21,000 M^{-1} cm^{-1}, respectively (Figure 5.7). The *trans* chromophores are metastable and, therefore, isomerize spontaneously to the fluorescent *cis* form (tG/tR → cG/cR). The lifetimes

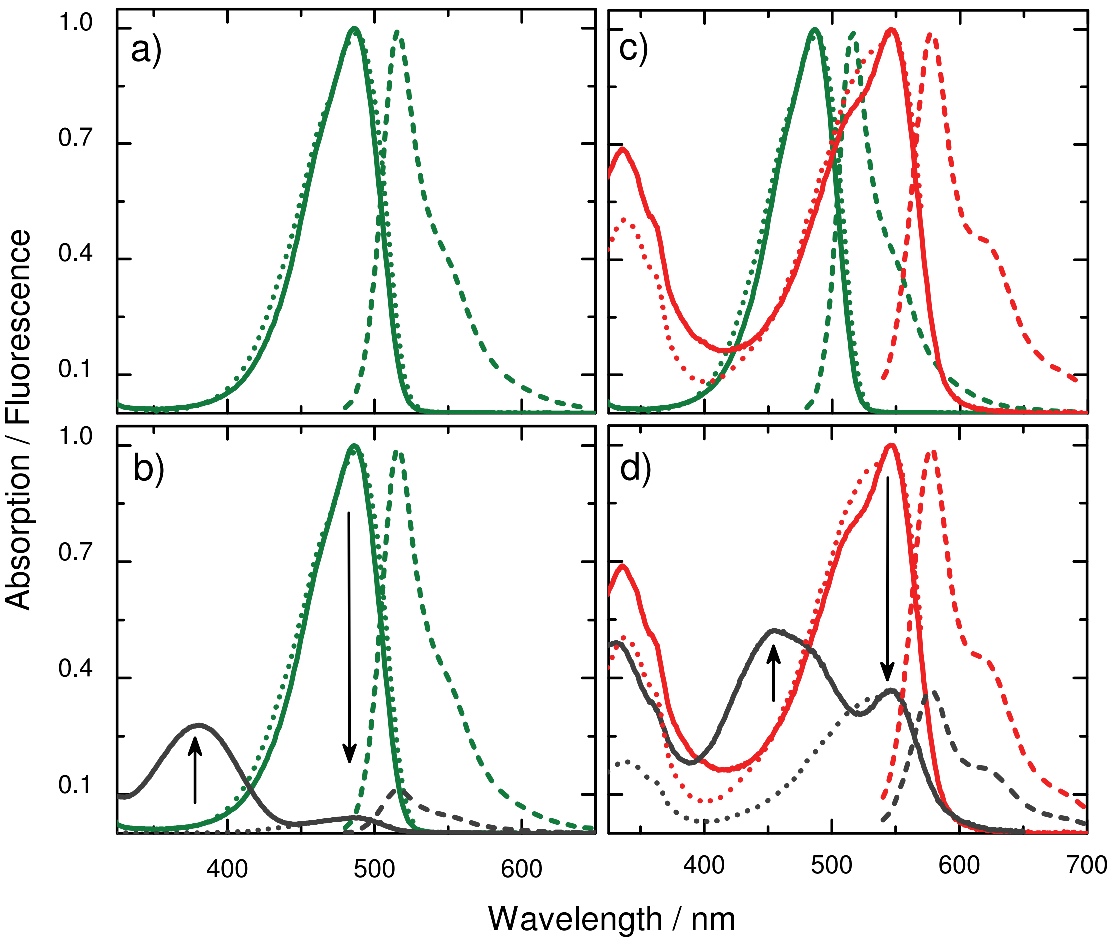

Figure 5.7: Spectral changes upon photoactivation. Absorption, excitation, and emission spectra scaled to equal maximum amplitudes are depicted by solid, dotted, and dashed lines, respectively. Emission spectra of green (red) mIrisFP were obtained by exciting at 473 (532) nm. Excitation spectra of green (red) mIrisFP were obtained by detecting emission at 540 (620) nm. (a) Thermally relaxed green form of mIrisFP. (b) Red mIrisFP (red) after photoconversion of green mIrisFP (green) with 405-nm light. (c) Green mIrisFP before (green lines) and after (gray) illumination with 473-nm light. (d) Red IrisFP before (red) and after (gray) illumination with 532-nm light. Spectra were recorded on solution samples in 20 mM carbonate buffer, 120 mM NaCl, pH 10.

of the green ($\tau_{\text{rec}} \sim 76\,\text{min}$) and red ($\tau_{\text{rec}} \sim 35\,\text{min}$) *trans* chromophores are significantly shorter than those of the IrisFP tetramer, indicating that the *trans* chromophores are less stabilized in the monomer. Previous studies on Dronpa also suggest that an increased structural flexibility of the β-barrel might promote the isomerization of the chromophore. The lack of stabilization of the protein interfaces in the monomeric IrisFP variant might account for a higher flexibility of the β-barrel in mIrisFP and, therefore, explain the reduced stabilization of the *trans* chromophore. Recovery can be accelerated by excitation in the $\mathrm{A}_\mathrm{t}^\mathrm{G}$ and $\mathrm{A}_\mathrm{t}^\mathrm{R}$ bands, respectively (tG/tR → cG/cR; $\phi_\mathrm{on}^\mathrm{G}\,(405\,\mathrm{nm}) = 0.36 \pm 0.02$, $\phi_\mathrm{on}^\mathrm{R}\,(473\,\mathrm{nm}) = 0.28 \pm 0.09$).

5.4 Applications of mIrisFP

Installation of the experimental setup, data acquisition and data evaluation were performed by Jochen Fuchs and Per Niklas Hedde (KIT, Inst. of Applied Physics, Group Prof. Nienhaus). The fusion proteins were constructed by Franz Oswald and Rosi Rittelmann (University of Ulm, Internal Medicine I, Group Prof. Oswald).

5.4.1 mIrisFP as a Genetically Encoded Marker

For the application of mIrisFP as a fusion tag in live-cell imaging studies, it is of importance that the mIrisFP tag does not interfere with the localization and functionality of the target proteins. We investigated the properties of mIrisFP as a fusion tag by transiently transfecting HeLa cells with several pcDNA3-mIrisFP fusion constructs, which all showed the expected expression and localization in widefield images. A functional assay was based on the expression level of a probe enzyme luciferase, which was evaluated by its overall activity. In this assay, the expression of the enzyme is mediated by the transcription factor p65. Tagging p65 to mIrisFP did not affect the expression level, which confirms the functionality of the p65-mIrisFP fusion construct. For more details, see Fuchs *et al.*[118].

5.4.2 Combining Pulse-Chase Experiments and Superresolution Imaging

The multiple photoactivation pathways in mIrisFP offer the possibility to combine pulse-chase experiments with superresolution imaging techniques, e.g., by utilizing PALM (Section 1.16) in living cells. Figure 5.8 illustrates the concept of such an experiment, which is described below in detail.

To demonstrate the advanced properties of mIrisFP, we constructed an α-actinin-mIrisFP fusion protein. α-actinin binds to actin filaments and cross-links them by forming dimers[144]. It also binds to focal adhesion components including integrins. α-actinin thereby transmits the tension of the actin cytoskeleton to the extracellular matrix. We used mIrisFP to observe translocation of α-actinin within a living cell over time. Therefor, we first monitored the initial distribution of the α-actinin-mIrisFP fusion protein by recording superresolution images with the green form of mIrisFP, using 473-nm light for both excitation and off switching. Figure 5.8 f and h illustrate an substantial resolution enhancement in the PALM images in comparison to the corresponding accumulated TIRF (*t*otal *i*nternal *r*eflection *f*luorescence) images. Sequently, we observed the redistribution of α-actinin.

By applying intense 405-nm light to a selected region of the cell we photoconverted mIrisFP molecules within this region to the red-emitting state (Figure 5.8 b). PALM images of the red form were collected using 561-nm light for excitation and off switching and weak 473-nm light to enhance on switching to the fluorescent state (Figure 5.8 c, i, j). During acquisition of the first image after photoconversion, α-actinin-mIrisFP fusion proteins already disperse over the cell, which is schematically indicated by the red dots in the green structures in Figure 5.8 c. Another PALM image at a later time interval showed additional redistribution of red-converted molecules over the entire cell (Figure 5.8 k,l). The kinetics of the distribution of the photoconverted molecules can be obtained by partitioning the total frames into groups, containing a fixed number of frames. The sum of all frames in one of those groups correspond to a particular time interval, which is determined by the acquisition time of one frame. Hence, the time resolution is defined by the number of frames in each group and is limited only by the acquisition time of one frame.

PALM is a quantitative imaging technique, based on the observation of single molecules. The experiment described above is, therefore, capable of monitoring the temporal evolution of the assembly and disassembly of individual structures, e.g., the turnover of paxillin in focal adhesions (Figure 5.9). Paxillin is a multidomain adaptor protein that localizes in focal adhesion protein complexes[145]. It transmits mechanical force and regulatory signals from the interior of the cell to the extracellular matrix. The dynamic turnover of the focal adhesions plays a crucial role in cell migration. They evolve typically over a few hundred seconds, which is a reasonable time frame for the collection of PALM images without blurring (frame times 10-100 s). To quantify the migration of paxillin during the disassembly of an adhesion point, we utilized a paxillin-mIrisFP fusion construct and assumed that the number of detected single molecules is proportional to the overall number of paxillin molecules in the adhesion site. Thus, the migration process can be tracked by analyzing the number of molecules that were registered per second in this adhesion point, with progressing time (Figure 5.9 a - e). First, we acquired an image of the initial state, detecting green mIrisFP molecules at a rate of $15\,\mathrm{s}^{-1}$. After photoconversion, red mIrisFP molecules were detected at a rate of $10\,\mathrm{s}^{-1}$. Subsequently,

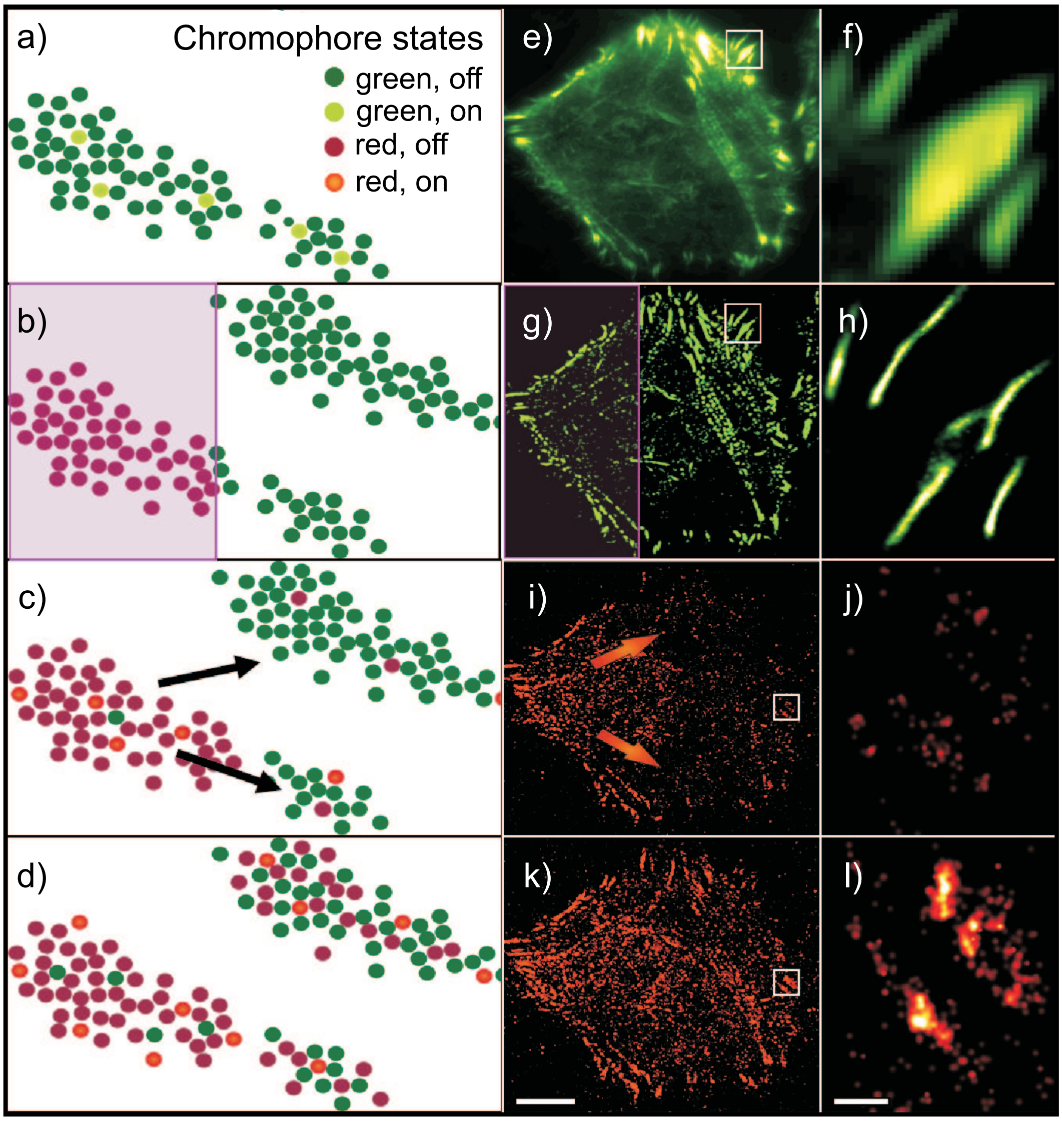

Figure 5.8: Combined pulse-chase experiments and superresolution imaging utilizing mIrisFP. (a - d) A PALM image is first acquired using off-on switching of green mIrisFP (a). A subpopulation of mIrisFP molecules in a region of the cell (violet) is photoconverted to the red form (b). These molecules migrate to other parts of the cell (c), which can be observed with PALM using off-on switching of red mIrisFP (d). (e - h) TIRF (e,f) and PALM (g,h) images of a HeLa cell expressing-α-actinin-mIrisFP. Closeups of the white boxed areas in e and g are shown in f and h. Fluorescence from green mIrisFP molecules was monitored (90 s total exposure). The violet box in g marks the irradiated region (405-nm laser light, 20 s). (i - l) PALM images detecting red-converted mIrisFP over the intervals 0 - 37.5 (s,i,j) and 100 - 300 s (k,l) after the end of photoconversion. Close-ups of boxed areas in i and k are shown in j and l. Scale bars, 10 µm (e,g,i,k) and 1 µm (f,h,j,l). The figure and caption are reproduced from Fuchs *et al.*[118].

they disappeared within ∼300 s, which indicates that paxillin-mIrisFP molecules migrated out of the observed adhesion site (Figure 5.9 e). Images calculated from the first and second 300-s time intervals after photoactivation confirm the disassembly of the adhesion point. In the 100 s after imaging of the red molecules, green molecules were not detected either, which verifies the complete disappearance of the adhesion point (Figure 5.9 d,e). Simultaneously, we observed the migration of photoconverted paxillin-mIrisFP molecules into an adhesion site during its maturation (Figure 5.9 f-j). Initially, we observed only a few molecules in the observed region. After photoconversion, the rate of detected red molecules remained constant for about 100 s and subsequently increased for ∼300 s. The comparison with the previously observed rate for the disassembly of an adhesion point indicates that assembly and disassembly occurred on the same time scales (Figure 5.9 e, j). The plateau at later times indicates stable adhesions. During the growth of an adhesion point, both green and red paxillin-mIrisFP were assembled, which is evident from the green image taken in the interval 600 - 700 s after photoconversion (Figure 5.9 i). Incorporation of red paxillin-mIrisFP molecules may be due to exchange of green fusion proteins with the pool of red ones or because of net growth. The only possibility to distinguish the two cases is to keep track of both species on a single molecule level, which requires monitoring of two different photoactivatable states and, therefore, can only be realized using mIrisFP.

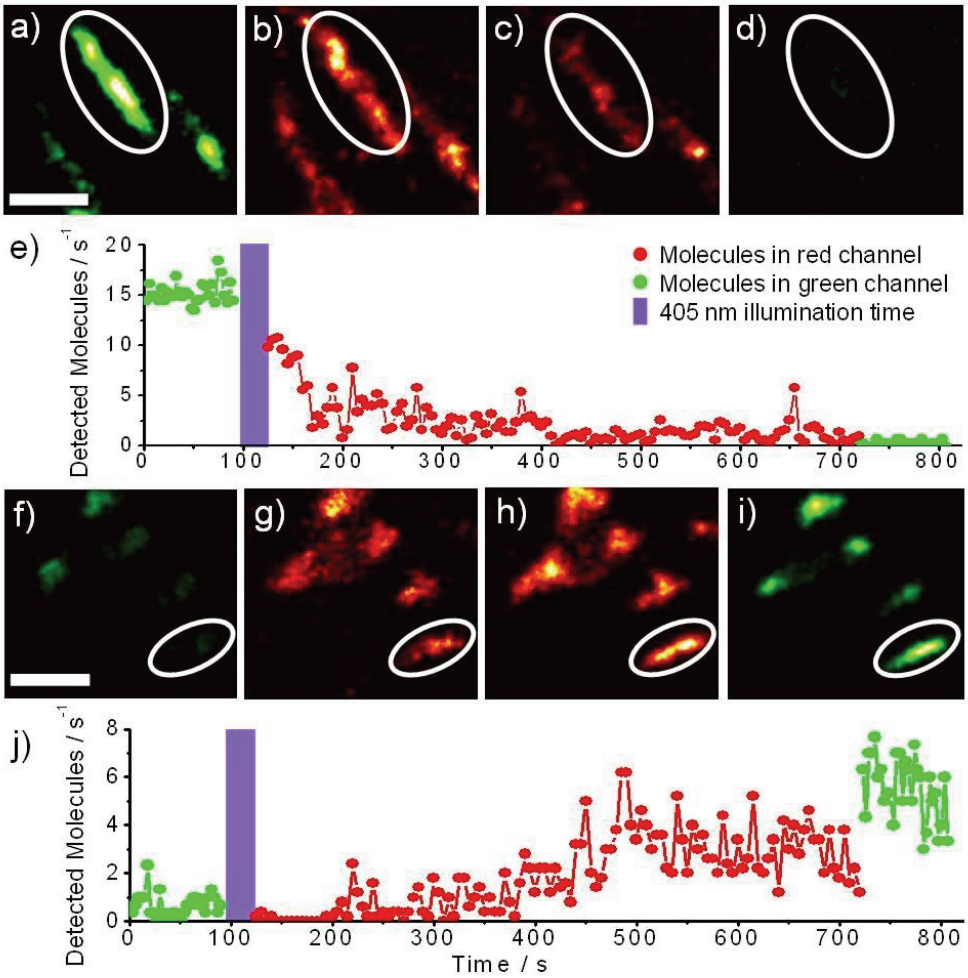

Figure 5.9: Focal adhesion dynamics in a live HeLa cell expressing paxillin-mIrisFP. (a-j) To monitor dynamics of a disappearing (a - e) or appearing (f-j) focal adhesion, PALM images were taken by excitation of green mIrisFP molecules for 90 s (a,f). After photoconversion, PALM images were acquired by exciting red mIrisFP, covering the intervals 0-300 s (b,g) and 300-600 s (c,h) after photoconversion. Finally, PALM images of the green form of mIrisFP at 600 s after photoconversion were collected (d,i). Scale bars, 1 µm. (e,j) Single molecules registered per second in individual adhesion sites (ellipses in a-d and f-i, respectively), plotted as a function of time. Each data point represents an average of over 100 image frames. We set the imaging parameters such that the rate of molecules detected in the green and the red channels differed only slightly. The figure and caption are reproduced from Fuchs *et al.*[118].

5.5 Summary and Conclusion

By insertion of the crucial mutation Phe173Ser into mEosFP*thermo* and by several further mutagenesis steps, we generated a monomeric version of IrisFP, mIrisFP, which essentially features the same photophysical properties as the tetrameric prototype. mIrisFP performs excellently in chimeric protein fusions, without compromising the localization properties or functionality of paxillin and α-actinin. Its multiple photoactivation functionalities render mIrisFP a useful extension of the FP toolbox, especially with regard to advanced light microscopy methods. The combination of reversible photoswitching and irreversible green-to-red photoconversion enables pulse-chase imaging experiments with superresolution. The competition between the individual photoactivation pathways does not hamper the performance of mIrisFP in PALM applications. Actually, both forms, green and red, match other monomeric PAFPs in the number of photons emitted per molecule[118]. Even through achieving best-possible results requires careful adjustment of the experimental parameters, considering the photophysical properties of the individual mIrisFP species.

Chapter 6

Investigation of Photoswitching Using mIrisGFP

6.1 mIrisGFP – a Model System

In the previous chapters, the experimental challenges have been discussed that arise due to the coexistence of reversible and irreversible photoactivation pathways. Handling mIrisFP will benefit from a detailed understanding of the underlying photoactivation mechanisms, which may also lead to the development of improved PAFPs. However, despite extensive experimental and theoretical studies, the mechanistic details are still under debate. Therefore, we used a non-photoconvertible variant of mIrisFP, called mIrisGFP (mEosFP*thermo* Phe173Ser), as a model system for the investigation of the reversible switching reactions. It efficiently and reversibly switches between a bright, green-fluorescent and a dark non-fluorescent state, but shows only marginal green-to-red photoconversion in bulk solution experiments. Its systematic photophysical characterization allowed us to propose a model including the various interconversions of chromophore species.

6.2 Spectroscopic Characterization of mIrisGFP

The spectroscopic features of mIrisGFP are similar to those of green mIrisFP and green tetrameric IrisFP (Table 6.1). The assignment of spectral bands to structural properties is based on X-ray data of tetrameric IrisFP, assuming structural agreement between tetramer and monomer (Section 4.1.1). Accordingly, the absorption spectrum in the visible region of thermally relaxed mIrisGFP is assigned to the *cis* chromophore (Figure 6.6, green lines). The *cis* chromophore features a neutral absorption band, A_c^G, centered on 389 nm ($\varepsilon_c = (24{,}000 \pm 2{,}000)\ \mathrm{M}^{-1}\,\mathrm{cm}^{-1}$, pH 4.5) and an anionic one, B_c^G, which is maximal at 488 nm ($\varepsilon_c = (47{,}000 \pm 2{,}000)\ \mathrm{M}^{-1}\,\mathrm{cm}^{-1}$).

The excitation spectrum, recorded for 540-nm emission, spectrally matches the absorption spectrum in the B_c^G band, but not the A_c^G band, which indicates that the anionic *cis* chromophore, C^-, is the dominant fluorescent species (Figure 6.6, dotted lines). It has a quantum yield of $\phi_{\text{fl}} = 0.63 \pm 0.06$, which is slightly higher than that of mIrisFP ($\phi_{\text{fl}} = 0.54 \pm 0.04$). The emission maximum is centered on 515 nm (Figure 6.6). The neutral chromophore is weakly fluorescent ($\phi_{\text{fl}} < 0.03$; Figure 6.6) with its emission maximal at 450 nm and featuring a substantial shoulder at $\sim$ 433 nm. The photophysical properties of mIrisGFP are compiled in Table 6.1.

Table 6.1: Spectral properties of mIrisGFP and its analogues[a].

	mIrisGFP	green IrisFP [120]	green mIrisFP [118]
ANIONIC CHROMOPHORE			
$\lambda_{\max}$ (Ex/Em), nm	488 / 516	488 / 516	486 / 516
ε_c ($\lambda_{\max}$), $\mathrm{M}^{-1}\,\mathrm{cm}^{-1}$	47,000 ± 2,000	50,800 ± 2,000	47,000 ± 2,700
ϕ_{fl}	0.63 ± 0.06	0.43 ± 0.02	0.54 ± 0.04
NEUTRAL CHROMOPHORE			
$\lambda_{\max}$ (Ex/Em), nm	n.d.	380 / 455	n.d.
ε_c ($\lambda_{\max}$), $\mathrm{M}^{-1}\,\mathrm{cm}^{-1}$	24,000 ± 2,000	22,000 ± 2,300	26,000 ± 1,200
ϕ_{fl}	< 0.03	0.027 ± 0.007	n.d.

[a] all values were estimated in 20 mM buffer, 150 mM ionic strength.

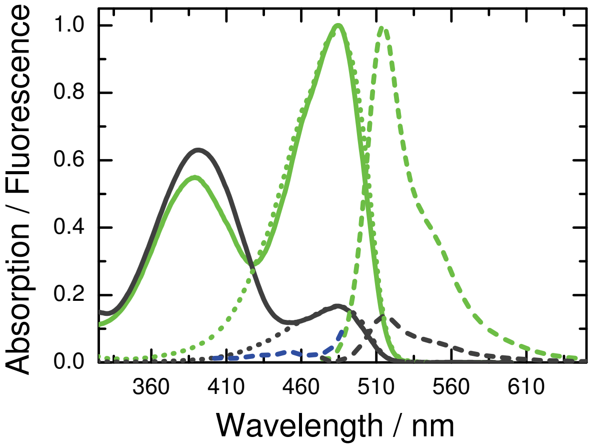

Figure 6.1: Spectral properties of mIrisGFP. Absorption (solid), excitation (dotted) and emission spectra (dashed) of mIrisGFP at pH 6.4 before (green) and after 473-nm illumination (gray). Excitation (emission) spectra were obtained by monitoring emission (excitation) at 540 (470) nm. The emission of thermally relaxed neutral mIrisGFP (blue dashed line) was excited at 390 nm.

6.3 Effect of pH on the Thermal Equilibrium of the mIrisGFP Chromophore

6.3.1 Protonation Equilibrium of the *Cis* Chromophore

To analyze the pH dependence of the interconversion between neutral and anionic *cis* chromophores, we recorded UV/Vis absorption spectra of mIrisGFP at different pH-values. A few selected spectra are plotted in Figure 6.2 a. Figure 6.3 a shows the relative fractions of neutral and anionic chromophore species, determined from the relative amplitudes of the $\mathrm{A}_\mathrm{c}^\mathrm{G}$ and $\mathrm{B}_\mathrm{c}^\mathrm{G}$ bands, as a function of pH (see Section 3.2 for details). The increase in green fluorescence intensity from pH 4 to 8 matches the increase in the fraction of anionic chromophores (Figure 6.3 a, open symbols). Deprotonation occurs in two steps, with $\mathrm{p}K_{a_1} = 5.3 \pm 0.1$ and $\mathrm{p}K_{a_2} = 6.5 \pm 0.4$, yielding a Gibbs free energy difference between the two protonation states, ΔG ($\mathrm{C}^H \rightarrow \mathrm{C}^-$), of 6.4 ± 0.4 $\mathrm{kJ\,mol^{-1}}$ at pH 7. The amplitude of the $\mathrm{B}_\mathrm{c}^\mathrm{G}$ band increases in yet another step with $\mathrm{p}K_a = 9.4 \pm 0.4$. This third $\mathrm{p}K_a$ value is neither observed for the amplitude of the $\mathrm{A}_\mathrm{c}^\mathrm{G}$ band nor does it result in a further increase in fluorescence, implying that it is not related to the deprotonation of the chromophore. Instead, this increase in the $\mathrm{B}_\mathrm{c}^\mathrm{G}$ band amplitude might be due to an increasing extinction coefficient. CD spectra of mIrisGFP show a comparable response to pH variation (Figure 6.2 b). The pH dependent intensity exchange between the $\mathrm{A}_\mathrm{c}^\mathrm{G}$ and $\mathrm{B}_\mathrm{c}^\mathrm{G}$ signals seen in the CD spectra confirms the results obtained via absorption spectroscopy (Figure 6.2 a). A $\mathrm{B}_\mathrm{c}^\mathrm{G}$-signal shift could not be resolved.

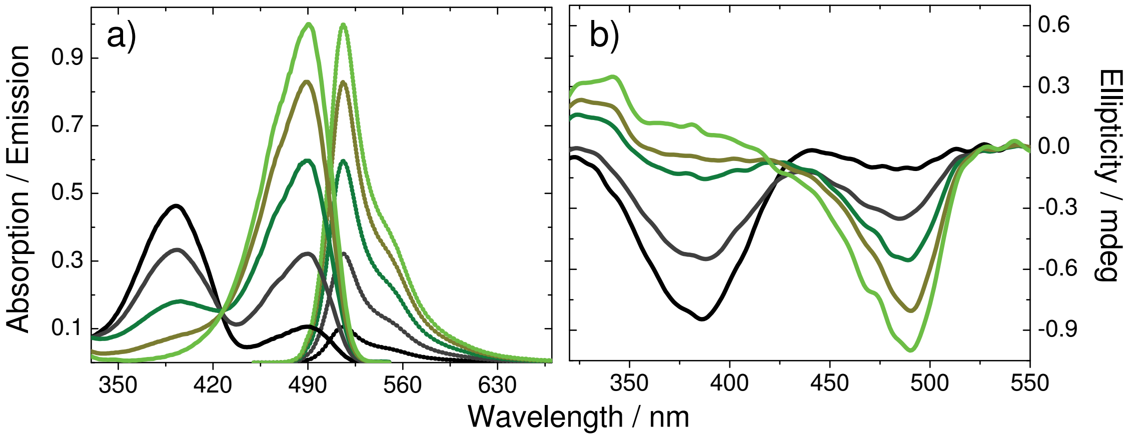

Figure 6.2: pH dependence of optical spectra of mIrisGFP in thermal equilibrium. a) Absorption (solid), emission (dashed) and b) CD spectra at pH 4.5 (black), 5.0 (gray), 6.0 (dark green), 7.0 (dark yellow) and pH 9 (light green). Emission was excited at 440 nm. The spectra were monitored in 20-mM buffer systems with 150-mM ionic strength, adjusted with sodium chloride.

The two-step protonation behavior observed for mIrisGFP is typical of mEosFP variants (data not shown). A similar behavior of cmFP512 has been interpreted earlier by a four-state model, in which the protonation of the chromophore was coupled to the pH equilibrium of a near-by amino acid (Section 1.2.2, Figure 1.5)[90]. The model assumes that protonation of the chromophore ($C^- \rightarrow C^H$) in the vicinity of a deprotonated amino acid X^- has a different pK_a than the protonation of the chromophore next to a protonated residue, X^H. Analogously, protonation of the amino acid is influenced by the protonation state of the chromophore. Protonation of X^- next to the neutral chromophore C^H could generate a shift of the A_c^G band. Such a shift was not measurable. Likewise, protonation of the amino acid X^- next to an anionic chromophore C^- might produce in a shift of the B_c^G band. Figure 6.3 b shows that the position of the B_c^G band shifts in three steps as a function of pH. The presence of multiple transitions in the position of the B_c^G band indicates the involvement of more than one titratable residue. The first step (blue shift from 486.7 to 486.3 nm) is described by p$K_a = 5.4 \pm 0.4$; the second step (red-shift from 486.3 to 486.7 nm) is described by p$K_a = 6.9 \pm 0.6$. The third shift of the B_c^G band occurs only after complete deprotonation of the chromophore, with p$K_a = 9.2 \pm 0.2$ (red shift from 486.7 to 488.6 nm) and, therefore, is not associated with the protonation equilibrium itself.

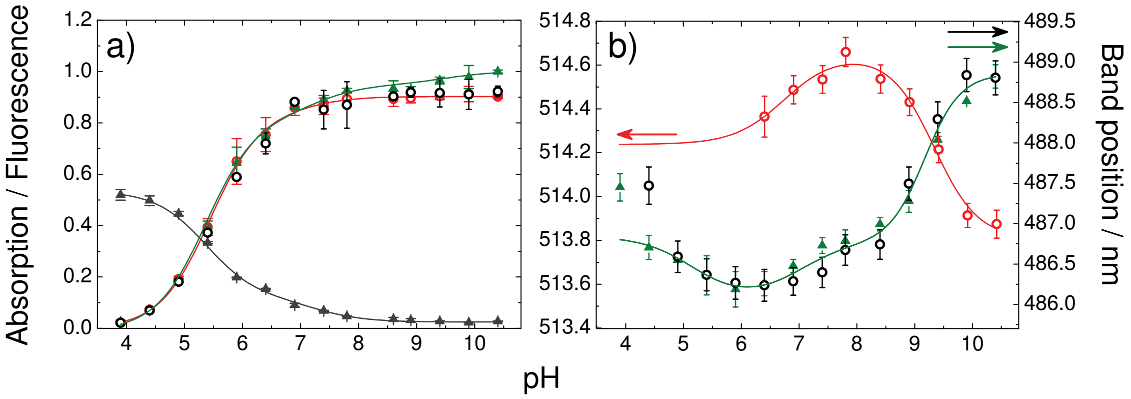

Figure 6.3: pH-dependence of optical band intensities and positions of the thermally relaxed mIrisGFP chromophore. (a) Development of the relative fractions of neutral and anionic chromophore represented by the intensities of the absorption A_c^G (gray triangles) and B_c^G bands (green triangles), and the intensity of the fluorescence excitation (black circles) and emission bands (red circles). The absorption was normalized relative to the maximum value of the absorption spectrum at pH 10.4. Intensities of the fluorescence bands were normalized to match the absorption B_c^G-band intensity between pH 4 and pH 7. Emission spectra were recorded with excitation at 470 nm; excitation spectra were recorded with emission at 540 nm. Fluorescence intensities were calculated from the integrated areas of the bands, corrected for protein concentration, as determined from the respective absorption spectra. (b) Position of the B_c^G-band absorption (green triangles), the excitation band maximum (black circles) and the emission band maximum (red circles). The data were globally fitted with multiple Henderson-Hasselbalch equations. The resulting curves (solid lines) are presented in the same colors as the respective symbols. Experiments were performed with $\sim 2\,\mu$M protein solution at varying pH values. Buffer conditions are specified in Section 3.2.

The relation between the deprotonation reactions of the adjacent amino acid side chain X and the mIrisGFP chromophore is illustrated in Figure 6.4. The protonation equilibrium of the chromophore is proposed to be directly affected by the protonation equilibrium of the adjacent amino acid side chain X. Since the free energy of the overall deprotonation reaction is independent of the sequence of the individual deprotonation steps, the respective pK_a values are related to each other by $pK_{a_1} + pK_{a_3} = pK_{a_2} + pK_{a_4}$. According to this relation, a shift in the A_c^G band is expected with a pK_{a_4} value of 4.2. Acid induced denaturation of mIrisGFP below pH 4 prevents measuring of reliable absorption spectra of the protein below this pH value.

The first two steps in the B_c^G-band shift are described by essentially the same pK_a values as the deprotonation of the chromophore, which implies that the chromophore and the adjacent amino acid X are in a protonation equilibrium, 'sharing' the proton. We suggest that amino acid X is subject to a similar equilibrium with a second amino acid Y, causing a multiple-step deprotonation of X (pK_{a_3}, pK_{a_5} and pK_{a_6}). Based on the protein structure we may tentatively assign X to His194 and Y to Glu212 (Figure 6.4).

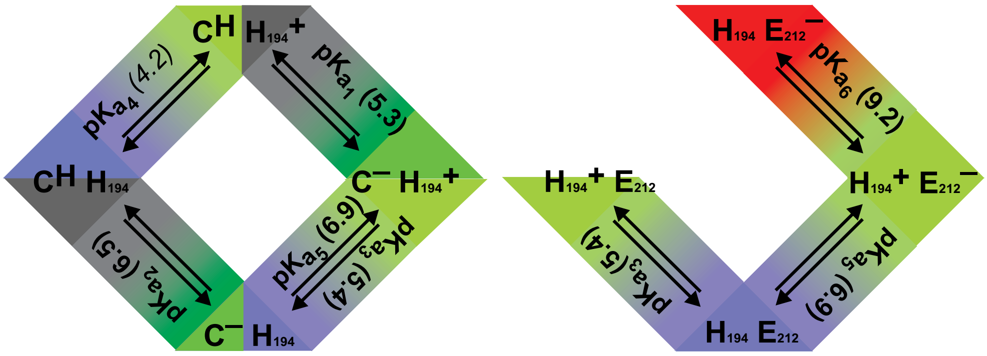

Figure 6.4: Schematic illustration of the protonation equilibrium of mIrisGFP in interaction with adjacent amino acid side chains. C^H and C^- represent the chromophore in the neutral (gray) and anionic (green) states, respectively. H194 and E212 represent the amino acid side chains of His194 and Glu212, respectively. The superscript '+' and '–' indicates their respective protonation states. The color gradients illustrate shifts in the spectral bands of the chromophore and their direction. Numbering of the pK_a values determined from the fits are given in parentheses.

The first step of chromophore deprotonation (pK_{a_1}, B_c^G-band amplitude) occurs simultaneously with deprotonation of the doubly protonated His194, neighboring the neutral Glu212 side chain (pK_{a_3}, blue shift of the B_c^G band; Figure 6.5). A neutral His194 might hydrogen bond to the neutral Glu212 via the free electron pair of the N_δ of its imidazole side chain. The second step (pK_{a_2}, B_c^G-band amplitude) may be caused by deprotonation of Glu212 (pK_{a_5}, red shift of the B_c^G band). Energetically, the anionic Glu212 side chain is preferentially stabilized by a salt bridge to a doubly protonated, cationic His194[146]. The energetic gain may increase the pK_a of His194, causing a reprotonation of the imidazole side chain. The third step (pK_{a_6}, red shift of the B_c^G band) may indicate a final deprotonation of His194 next to the deprotonated Glu212.

The mIrisGFP variant Glu212Gln does not show the second step in the shift of the absorption bands, suggesting that pK_{a_5} is directly related to Glu212. Instead, it shows a two-step shift described by pK_a 4.9 ± 0.1 and 9.1 ± 0.1, which are similar to pK_{a_3} and pK_{a_6} in mIrisGFP (Figure 6.4). The existence of these pK_as does not support the hypothesis that the third step in the absorption band shift might be related to the deprotonation of a reprotonated His194.

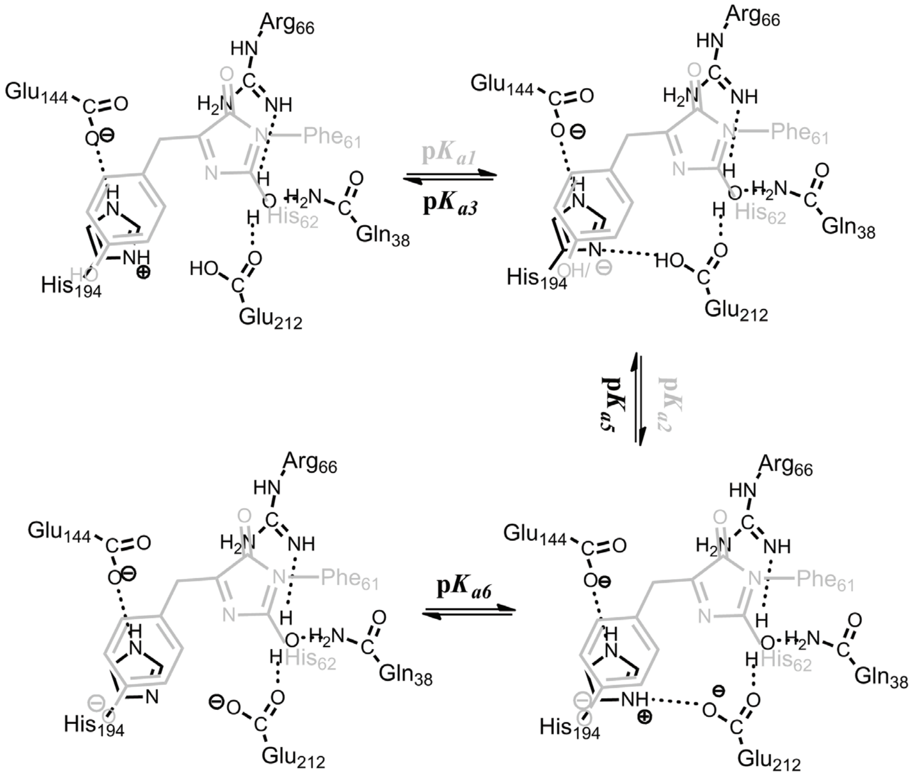

Figure 6.5: Schematic illustration of the hydrogen bonding network below the chromophore upon pH change. The chromophore in its respective protonation states in depicted in gray, whereas amino acid side chains and water are illustrated in black. pK_a values correspond to Figure 6.4.

The shift of the B_c^G band position is mirrored by a shift of the excitation spectrum (Figure 6.3). The third step in the B_c^G band position shift ($pK_a = 9.3 \pm 0.2$) is also observed as a blue shift of the emission band and in an increase of the B_c^G band amplitude. The latter is accompanied neither by a loss of neutral chromophores nor by an increase of the integrated fluorescence intensity of the emission and excitation spectra. However, emission and excitation spectra were recorded at each pH for the same excitation (470 nm) and emission wavelength (540 nm), respectively. The red shift of the absorption / excitation band results in a reduced extinction coefficient at the excitation wavelength (470 nm), which reduces the molecular brightness (ε_c (470 nm) $* \phi_{\text{fl}}$) and, therefore, the integrated fluorescence intensity. A

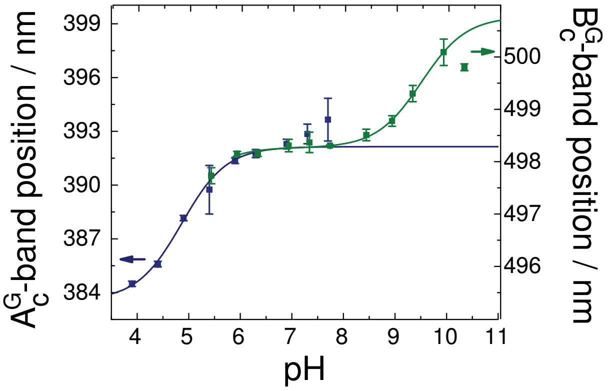

Figure 6.6: Shift of mIrisGFP Glu212Gln absorption bands. Both the A_c^G (blue) and the B_c^G (green) bands shift in a single step with $pK_a = 4.9 \pm 0.04$ and $pK_a = 9.1 \pm 0.13$, respectively.

similar effect is observed for the integrated fluorescence intensity of the excitation spectrum. Owing to the blue shift of the emission band, the absolute intensity observed at 540 nm decreases with increasing pH with $pK_a = 9.3 \pm 0.1$. Overall, the increase of the extinction coefficient from (43,000 ± 2,500) $M^{-1}\,cm^{-1}$ at pH 7 to (47,000 ± 3,500) $M^{-1}\,cm^{-1}$ at pH 10 is canceled by the effects due to the respective shifts in the fluorescence bands. Hence, despite the increase in the amplitude of the B_c^G band, no gain in the integrated fluorescence intensity is observable.

6.3.2 Protonation Equilibrium of the *Trans* Chromophore

To obtain information on the deprotonation behavior of the neutral *trans* chromophore, we measured CD spectra of the light-induced species as a function of pH. As it takes about 10 min to collect a single CD spectrum, it is likely that a certain fraction of *trans* chromophores may have relaxed back to the *cis* state during data collection. As a result, the spectra of the fractions of *cis* and *trans* chromophores are superimposed, presumably in different ratios, depending on pH. Thus, it was not possible to determine the exact pK_a for deprotonation of the neutral *trans* chromophore. However, as the A_t^G signal of the *trans* chromophore dominates the CD spectrum even at pH 10, we suggest a $pK_a > 10$ (Figure 6.7). Comparably high pK_a values of the *trans* chromophore have been found also for photoactivatable variants of GFP[147].

Although the amplitude of the A_t^G signal amplitude did not vary noticeably, we could clearly observe a blue shift from 396.8 to 384.3 nm between pH 5 and 10 (Figure 6.8 a). The corresponding CD signal shifts from 401.0 to 384.6 nm (Figure 6.8 b). Both shifts can be modeled with a pK_a of 7.8 ± 0.1, indicating protonation of an amino acid next to the neutral *trans* chromophore (Figure 6.8 c).

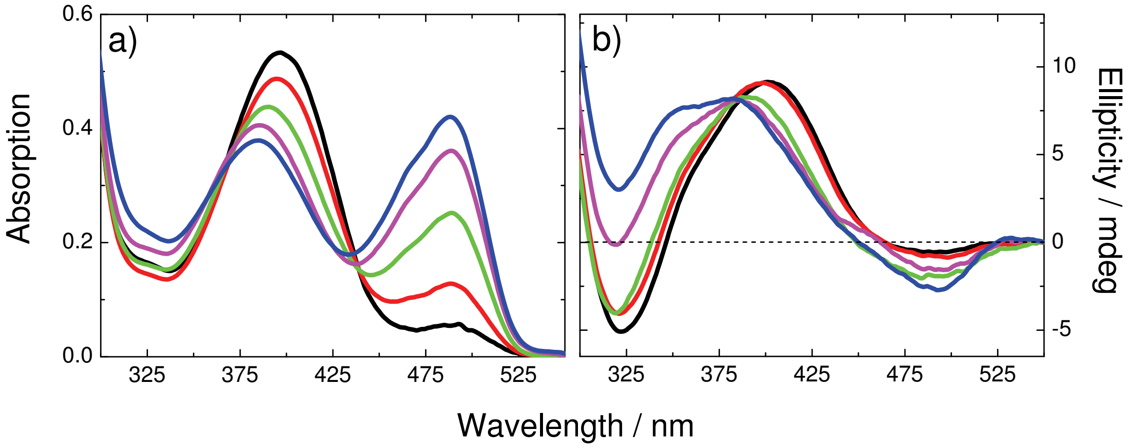

Figure 6.7: pH-dependent optical spectra of the mIrisGFP chromophore in the *trans* state. (a) Absorption and (b) CD spectra at pH 5.0 (black), 7.0 (red), 8.0 (green), 9.0 (magenta) and 10.0 (blue). Spectra are normalized to equal protein concentrations.

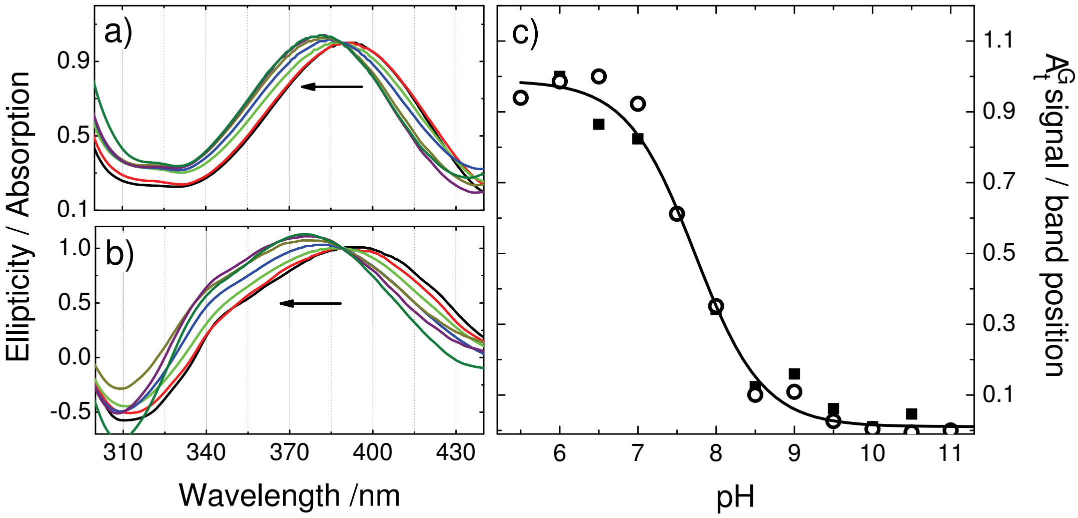

Figure 6.8: Shift of the *trans* chromophore bands with pH. The sample was illuminated with 473-nm light until the green color of the protein solution faded. Afterwards, (a) absorption and (b) CD spectra were recorded. Increasing pH is indicated by arrows. The spectra are normalized to the maximum value at pH 7, at 389 nm. (c) Shift of the *trans* absorption bands, normalized between 0 and 1. It shifts about 16 nm in ellipticity (filled squares) and 12 nm in absorption (open circles). Samples contained about 30 µM protein in several buffers with pH varying between 5.5 and 11 (for details see Section 3.2).

6.3.3 Structural Interpretation of the Protonation Equilibrium Shift upon *Cis-Trans* Isomerization of the Chromophore

The different pH dependencies of the protonation reactions of the *cis* and the *trans* chromophores are related to their interactions with neighboring amino acids. X-ray diffraction data of on-state IrisFP have shown that Arg66 interacts with the carbonyl oxygen of the imidazolinone moiety of the *cis* chromophore, which decreases the electron density of the heterocycle and results in a low $\mathrm{p}K_a$[120]. The phenyl moiety of the anionic *cis* chromophore is stabilized by hydrogen bonds to Ser142 and two water molecules. Upon photoswitching, Glu212 flips by $\sim 90°$ and, thereby, approaches the imidazolinone nitrogen atom of the *trans* chromophore (*cis*: 3.4 Å, *trans*: 2.8 Å). Arg66 rearranges below the chromophore such that its side chain no longer interacts with the carbonyl oxygen of the imidazolinone ring. Instead, the imidazolinone oxygen is in hydrogen bonding distance to a water molecule. The concomitantly enhanced charge density on the phenyl moiety is expected to cause stronger binding of the proton. Hence, chromophore deprotonation is markedly disfavored, raising the $\mathrm{p}K_a$ value. Furthermore, the neutral *trans* chromophore is stabilized by a hydrogen bond from the hydroxyphenyl moiety to the negatively charged Glu144.

6.4 Chromophore Interconversion in mIrisGFP at the Macroscopic Level

As discussed in the previous section, *cis-trans* photoisomerization occurs concomitantly with the alteration in the chromophore protonation state, in good agreement with previous studies on Dronpa[148,149]. Hence, at least four ground state chromophore species have to be considered, i.e., the neutral and anionic *cis* and *trans* states. Upon light activation, the corresponding excited-state species have to be taken into account, too. The resulting eight-state model is depicted in Figure 6.9.

6.4.1 Wavelength Dependence of Photoswitching

In previous reports, off switching was assumed to occur upon excitation of the anionic fluorescent species, i.e., with wavelengths in the spectral range of the chromophore $\mathrm{B}_\mathrm{c}^\mathrm{G}$ band[123,148–150]. The actual relevance of the chromophore protonation

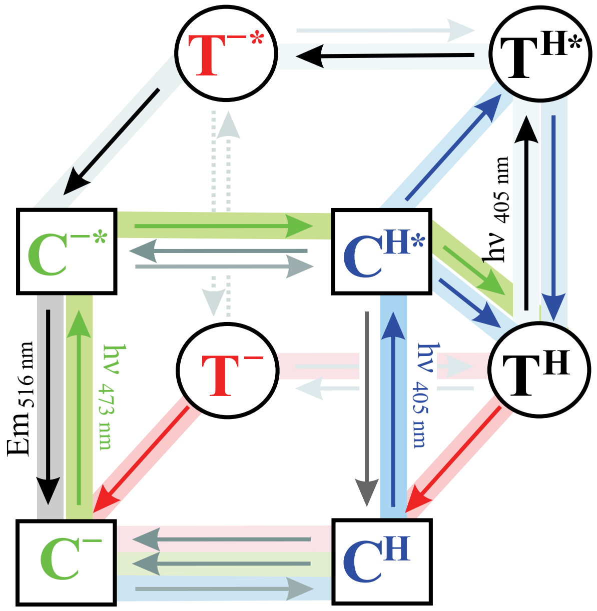

Figure 6.9: Eight-state model comprising the possible chromophore species of mIrisGFP. (C = *cis*; T = *trans*; '–' = anionic; H = neutral; '*' = excited state). Arrows are color coded to guide the eye from the reactant to the product.

states for photoinduced isomerization was investigated using mIrisGFP samples at pH 5.3, which contain approximately equal fractions of neutral and anionic chromophores. During the experiment, the samples were excited for 300 s at different wavelengths ranging from 330 to 550 nm. The relative loss in fluorescence at 520 nm (540 nm for excitation wavelengths of 490 - 530 nm) was corrected for differences in light intensities and excitation photon energies and plotted against the excitation wavelength to yield the off switching action spectrum.

In Figure 6.10, the action spectrum is compared with the absorption spectrum of mIrisGFP at pH 5.3. After scaling its amplitude to the A_c^G band, the relative amplitudes deviate significantly in the B_c^G bands, which suggests that off switching by exciting the anionic *cis* chromophore is less efficient than by exciting the neutral one. The excitation spectrum indicates that the neutral *cis* chromophore does not directly contribute to the fluorescence at 520 nm, which was monitored for recording the action spectrum (Figure 6.10). However, the loss in neutral *cis* chromophores due to isomerization leads to a readjustment of the ground state equilibrium between neutral and anionic *cis* chromophores. According to the pK_a values, the fraction of anionic *cis* chromophores decreases concomitantly with that of neutral *cis* chro-

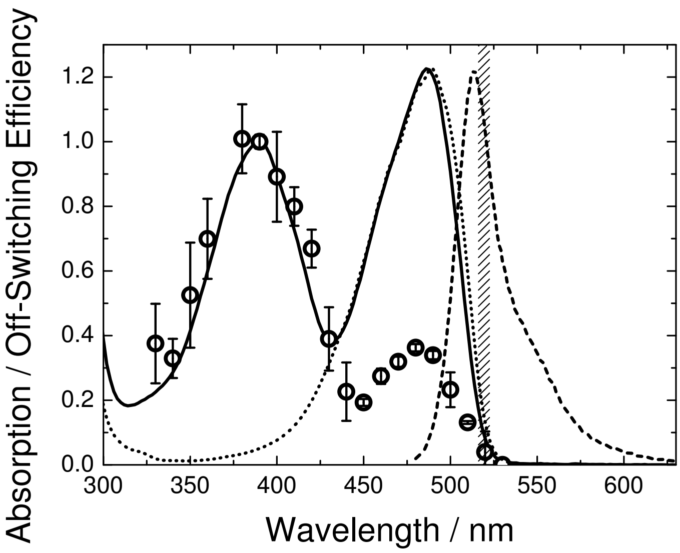

Figure 6.10: Wavelength dependence of the off switching in mIrisGFP. The decrease of the fluorescence intensity (symbols) upon illumination with light of a particular wavelength is plotted together with the absorption (solid line), excitation (dotted line), and emission (dashed line) spectra at pH 5.3. Illumination was performed for 300 s, while monitoring the fluorescence decrease at 520 nm (hatched bar). Emission (excited at 470 nm) and excitation spectra (recorded for emission at 540 nm) were adjusted to match the maximum absorption at 488 nm, which represents the fluorescent species. The amplitude of the action spectrum was scaled to match the peak maximum of the A_c^G band of the absorption spectrum.

mophores. As a result, the fluorescence signal loses intensity. The reversibility of the observed loss in emission intensity was controlled by comparing the absorption spectra before illumination with 405-nm light and after thermal recovery in the dark for 62 h at room temperature (Figure 6.11). They are essentially identical which implies full recovery of the sample and thus only negligible irreversible photobleaching. The minor difference is accounted for by the incomplete recovery within the given time (τ_{rec} (pH 5) = 18 h). Similarly long recovery times have been reported for Dronpa[150,119].

6.4.2 Exciting the Anionic Chromophore

The differences in the A_c^G and B_c^G band amplitudes of the action spectrum suggest that different molecular mechanisms with different efficiencies are involved in off switching via the neutral and anionic *cis* chromophores. Off switching upon excitation of the anionic *cis* chromophore was investigated by applying 473-nm light

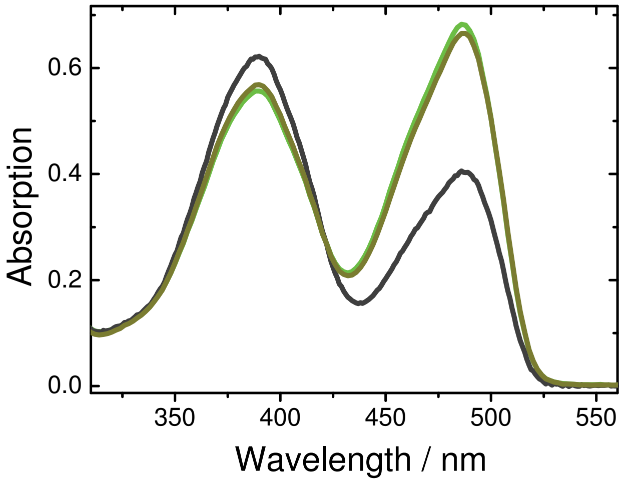

Figure 6.11: Off switching by excitation within the neutral chromophore band. Absorption spectra of an mIrisGFP sample at pH 5.3 recorded before (green) and after (gray) illumination with 405-nm light. A third absorption spectrum of the sample (brown) was recorded after ∼ 62 h recovery in the dark at room temperature.

('green' pathway, Figure 6.9) and monitoring the loss of emission intensity at 520 nm (Section 3.4). Comparison of the mIrisGFP absorption spectra at pH 6, monitored before and after 473-nm illumination, reveals that a new chromophore band, A_t^G, with an absorption peak at 391 nm gains intensity at the expense of the B_c^G band (Figure 6.12 a). The peak position of A_t^G is similar to that of the A_c^G band of the neutral *cis* chromophore ($\lambda_{max} = 389$ nm), suggesting that both A_c^G and A_t^G represent a neutral chromophore. Different molecular structures of the corresponding chromophores may be responsible for the changes of the CD spectrum (Figure 6.12 b). The CD spectrum of a non-illuminated sample shows a signal with negative ellipticity over the whole spectral range of the A_c^G and B_c^G bands (Figure 6.12 b, green line). After 473-nm illumination, these signals are almost depleted, whereas a new signal with a positive ellipticity arises in the spectral range of the A_t^G band (Figure 6.12 b, gray line). X-ray diffraction and spectroscopy studies have assigned these bands to the neutral *trans* chromophore (Section 4.1.1, 4.2)[120]. Owing to the protonation equilibrium of the *cis* chromophore, indicated by the gray arrows between C^- and C^H in Figure 6.9, the neutral *cis* chromophore, C^H, and the anionic *cis* chromophore, C^-, are depleted simultaneously while the fraction of neutral *trans* chromophores, T^H, increases upon 473-nm illumination. There is no clear experimental indication of an anionic *trans* chromophore, T^- (absorption band or CD signal, Figure 6.7). The most probable explanation is that the *trans* chromophore has a very high pK_a value. Recently, pK_a values above 9 have also been reported for the *trans* chromophores of several GFP mutants[147]. The high proton affinity of the *trans* chromophore in mIrisGFP can be explained by its proximity to Glu144, which is likely to be negatively charged at physiological pH and, therefore, impedes deprotonation of the *trans* chromophore. Results of spectroscopic and crystallographic analyses of Dronpa are similar to those of green IrisFP and mIrisGFP[119,127]. There, two different neutral species, A1 (acid-induced) and A2 (photoswitched) were identified[149]. Both X-ray diffraction[119,127] and theoretical studies[151,152] have identified A2 as the neutral *trans* form, T^H. In Dronpa, A2 (A_t^G) is generated upon excitation of the anionic *cis* chromophore.

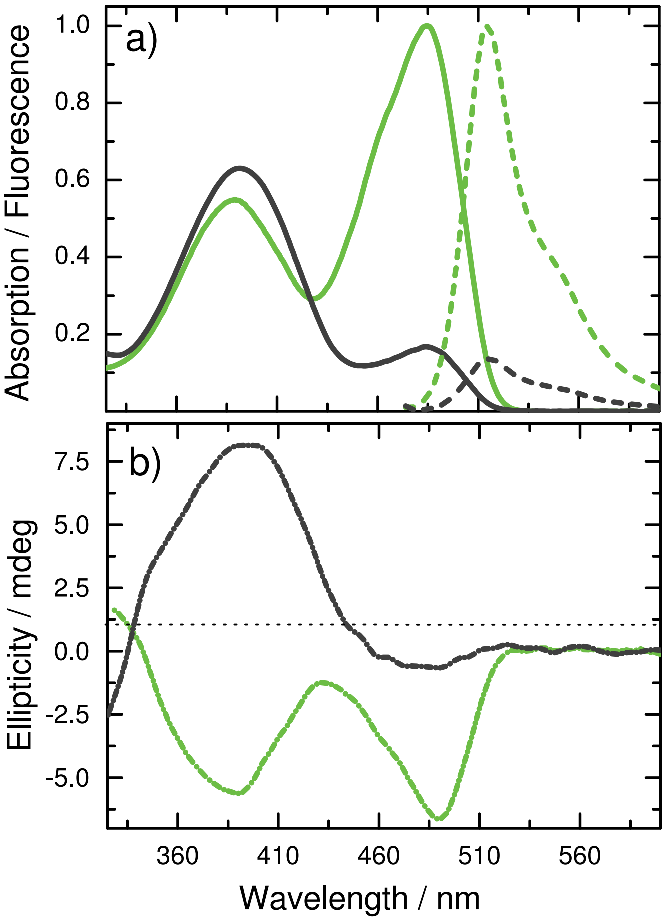

Figure 6.12: UV/visible spectra of mIrisGFP, pH 6, before and after illumination with 473-nm light. (a) Absorption (solid) and emission (dashed) and (b) CD spectra in the on/*cis* (green) and off/*trans* (gray) states.

pH Sensitivity of the Off Switching Process by Exciting the Anionic *Cis* Chromophore

The apparent rate coefficient of the $C^- \rightarrow T^H$ transition, k_{off}, is pH-dependent. The reaction accelerates with increasing pH ~3-fold between pH 5 ($k_{\text{off}} = (0.024 \pm 0.004)\,\text{s}^{-1}$) and pH 9.5 ($k_{\text{off}} = (0.06 \pm 0.001)\,\text{s}^{-1}$) for 473-nm illumination ($24\,\text{mW}\,\text{cm}^{-2}$). The increase of k_{off} has the same pH dependence as the deprotonation of the *cis* chromophore. Since changes in the extinction coefficient, ε_c, are negligible in the observed pH range, the rate coefficient k_{off} is directly related to the quantum efficiency of the off switching reaction (Equation 3.11). Thus, the quantum efficiency of the off switching ($\phi_{\text{off}} \propto \frac{k_{\text{off}}}{\varepsilon_c}$, Equation 3.11) is directly proportional to the fraction of anionic chromophores (Figure 6.13), which implies that the reaction rate coefficient is governed by the supply of reactant, i.e., the anionic *cis* chromophore, C^-. The concentration of anionic chromophores is determined by (i) the pH, according to the pK_a values of mIrisGFP, and the (ii) rate coefficient of the readjustment of the ground state equilibrium between the neutral and the anionic forms, $C^- + H^+ \rightleftharpoons C^H$. The deprotonation of neutral chromophores occurs presumably within microseconds to milliseconds[147], which matches the corresponding observed apparent rate coefficients, k_{off}.

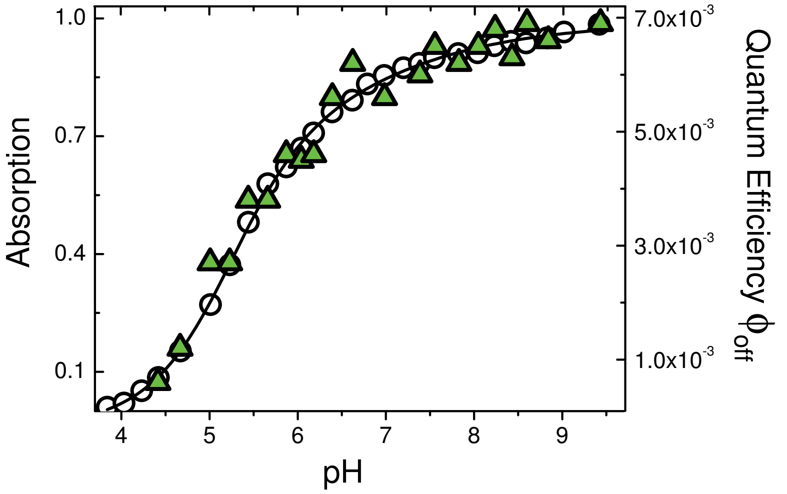

Figure 6.13: pH dependence of the off switching quantum efficiency, ϕ_{off}. pH dependence of the quantum efficiency for off switching with 473-nm light at $24\,\text{mW}\,\text{cm}^{-2}$, ϕ_{off} (green symbols), compared to the relative fraction of anionic *cis* chromophores (open circles).

Competition Between Off Switching and Recovery Processes

473-nm light triggers off switching, which results in a decrease of the emission intensity but not in a total loss. The residual fluorescence decreases exponentially with increasing excitation power (Figure 6.14). It reaches a minimum value of 4.3 % of the original fluorescence at pH 7 and room temperature. The residual fluorescence might be due to thermal recovery of the *cis* chromophore. In this case, the residual fluorescence would directly depend on the thermal recovery rate, k_{rec}, according to:

$$K\,(473\,\text{nm}) = \frac{[orginal]-[residual]}{[residual]} = \frac{[\text{T}^H]}{[\text{C}^-]} = \frac{k_{\text{off}}(473\,\text{nm})}{k_{\text{rec}}} = 22.3 \tag{6.1}$$

where the equilibrium coefficient $K\,(473\,\text{nm})$ describes the equilibrium between anionic *cis* and neutral *trans* chromophores upon 473-nm illumination, $\text{C}^- \rightleftharpoons \text{T}^H$.

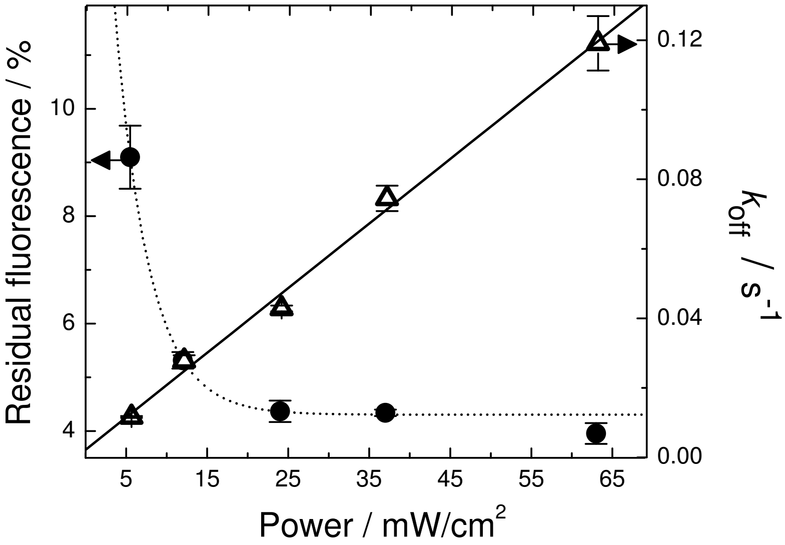

Figure 6.14: Off switching using different excitation powers. Residual fluorescence (in percent of the initial fluorescence) after off switching of mIrisGFP at pH 7 upon 473-nm illumination with various laser powers (circles) and the corresponding exponential fit (dotted line). The rate coefficient k_{off} shows a linear dependence on the excitation power (triangles).

The thermal recovery rate, k_{rec}, was determined as $(1.8 \pm 0.05) \times 10^{-4}$ s^{-1} at 290 K and pH 7. Thus, the maximal rate coefficient of the off switching, describing only *cis*-to-*trans* isomerization, k_{ct}, is calculated as $(4.01 \pm 0.22) \times 10^{-3}$ s^{-1} according to Equation 6.1. At the maximum power used here (P = 63 mW cm^{-2}), the observed rate coefficient ($k_{\text{off}} = 0.12 \pm 0.01$ s^{-1}) is significantly higher than the calculated one. However, the experimental, apparent rate coefficient, k_{off}, is expected to be even lower than the calculated value of the rate coefficient for the process, k_{ct}, because it describes the sum of the rate coefficients of the photoinduced off switching process, thermal recovery of C$^-$, deexcitation via fluorescence and additional relaxation pathways, which do not involve chromophore isomerization. Thus, thermal recovery is too slow to explain the observed $K\,(473\,\text{nm})$. The discrepancy might be explained by photoinduced acceleration of the recovery process by 473-nm light, which would imply that the neutral *trans* chromophore, T^H, shows absorption at this wavelength. To confirm this hypothesis, the off switching experiment was repeated at different wavelengths. The $\mathrm{A}_{\mathrm{t}}^{\mathrm{G}}$ and the $\mathrm{B}_{\mathrm{c}}^{\mathrm{G}}$ bands overlap in the range between 430 and ~490 nm. In this range, the extinction coefficient of the $\mathrm{B}_{\mathrm{c}}^{\mathrm{G}}$ band increases with increasing wavelength, while the extinction coefficient of the $\mathrm{A}_{\mathrm{t}}^{\mathrm{G}}$ band decreases. Thus, direct excitation of the neutral *trans* chromophore becomes less likely at higher wavelengths and, therefore, the residual fluorescence should decrease (Figure 6.12). Off switching by 460-, 470- and 480-nm light indeed shows the expected behavior. Normalized to the yield in residual fluorescence upon 460-nm illumination, this parameter decreases from 100 % to 33 % and 25 % with increasing excitation wavelength. These results confirm that a light-driven recovery process opposes off switching, $\mathrm{T}^H \rightleftharpoons \mathrm{C}^-$ (Figure 6.9, gray marked arrows). Overall, the residual fluorescence is determined by the ratio of the extinction coefficients of the chromophore species C$^-$ and T^H at the excitation wavelength.

6.4.3 Thermal Recovery of the *Cis* Chromophore

When 473-nm illumination is switched off, the $\mathrm{A}_{\mathrm{t}}^{\mathrm{G}}$ band exchanges back into the $\mathrm{B}_{\mathrm{c}}^{\mathrm{G}}$ absorption band over time (Figure 6.15), which demonstrates the metastable nature of the neutral *trans* chromophore. Thermal recovery of the *cis* chromophore was monitored via the amplitude gain of the $\mathrm{B}_{\mathrm{c}}^{\mathrm{G}}$ band at 489 nm. The absorption band of the anionic *cis* chromophore $\mathrm{B}_{\mathrm{c}}^{\mathrm{G}}$ band overlaps spectroscopically only marginally with that of the neutral *trans* chromophore species, $\mathrm{A}_{\mathrm{t}}^{\mathrm{G}}$. Monitoring the recovery by observing the population of neutral *cis* chromophores is not possible because the corresponding absorption band, $\mathrm{A}_{\mathrm{c}}^{\mathrm{G}}$, overlaps almost entirely with the absorption band of the neutral *trans* chromophore, $\mathrm{A}_{\mathrm{t}}^{\mathrm{G}}$. The resulting time trace would, therefore, be a superposition of two processes, the increase of $\mathrm{A}_{\mathrm{c}}^{\mathrm{G}}$ and the decay of $\mathrm{A}_{\mathrm{t}}^{\mathrm{G}}$.

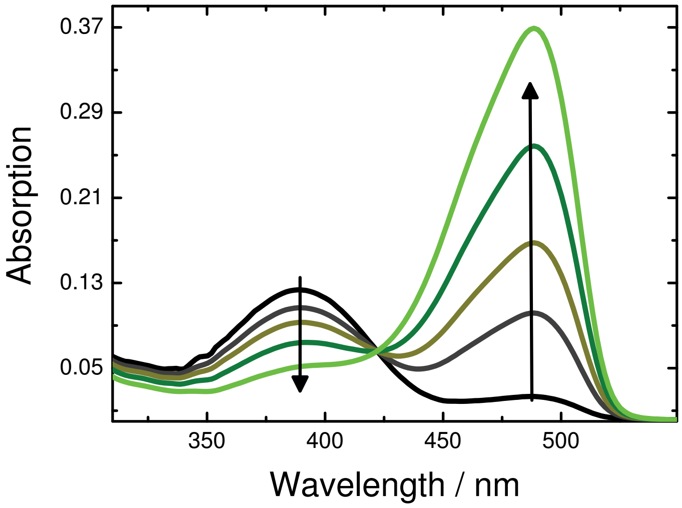

Figure 6.15: Absorption spectra collected during thermal recovery of mIrisGFP at pH 7, 310 K. Absorption spectra obtained 0 (black), 3.6 (gray), 7 (dark yellow), 15 (green) and 40 minutes (bright green) after off switching. Arrows indicate the time sequence.

At pH 7 and 290 K, the lifetime of the *trans* chromophore is on the order of 86 min. The recovery reaction accelerates with temperature; at 310 K, the lifetime decreases to 19 min. Thermal recovery to the anionic *cis* state is also influenced by pH. Between pH 5.5 and 10.5, the rate coefficient, k_{rec}, increases about 40-fold, from $(0.9 \pm 0.03) \times 10^{-2}\,\mathrm{s}^{-1}$ to $(40.26 \pm 1.8) \times 10^{-2}\,\mathrm{s}^{-1}$ at 310 K, described by two distinct steps with pK values of 7.8 ± 0.4 and 9.5 ± 0.6 (Figure 6.16 a). The pK_{rec_1} value of 7.8 is not observed in the mutant Glu212Gln, which suggests that, in mIrisGFP, deprotonation of Glu212 contributes to the destabilization of the *trans* chromophore (Figure 6.16 a, black squares). Presumably, the Glu212 side chain is neutral and establishes a hydrogen bond to the imidazolinone nitrogen of the *trans* chromophore (Figure 4.4) [120]. His194 is fixed almost perpendicular to the chromophore plane by hydrogen bonds to Ser142 and a water molecule, which might sterically hamper *trans*-to-*cis* relaxation (Figure 6.17 a). We suggest that deprotonation of Glu212 leads to an electrostatic repulsion between the free electron pair on the chromophore imidazolinone nitrogen and the negatively charged carboxyl group. This induces a rotation of ~ 90° around the β-carbon of the glutamate side chain. The rotation of the glutamate side chain may promote reorientation of the presumably positively charged His194 side chain, away from Ser142 toward the deprotonated, negatively charged Glu212 to establish a quadrupole network of salt bridges and hydrogen bonding interactions, which also involves Arg66, Glu144 and a water molecule (Figure 6.17 b). We have observed a similar structural arrangement below the *cis* chromophore (Figure 4.4). In this conformation, *trans*-to-*cis* isomerization is favored because the steric restriction due to the perpendicular conformation of the His194 side chain is no longer present. Moreover, the *cis* isomer may be stabilized by π-stacking between the His194 side chain and the chromophore hydroxyphenyl moiety.

We emphasize that the pK_a of ~ 7.8 refers to deprotonation of Glu212 next to the *trans* chromophore, whereas in Section 6.3.1 we have discussed the deprotonation of Glu212 next to the *cis* chromophore (p$K_a = 6.9 \pm 0.6$).

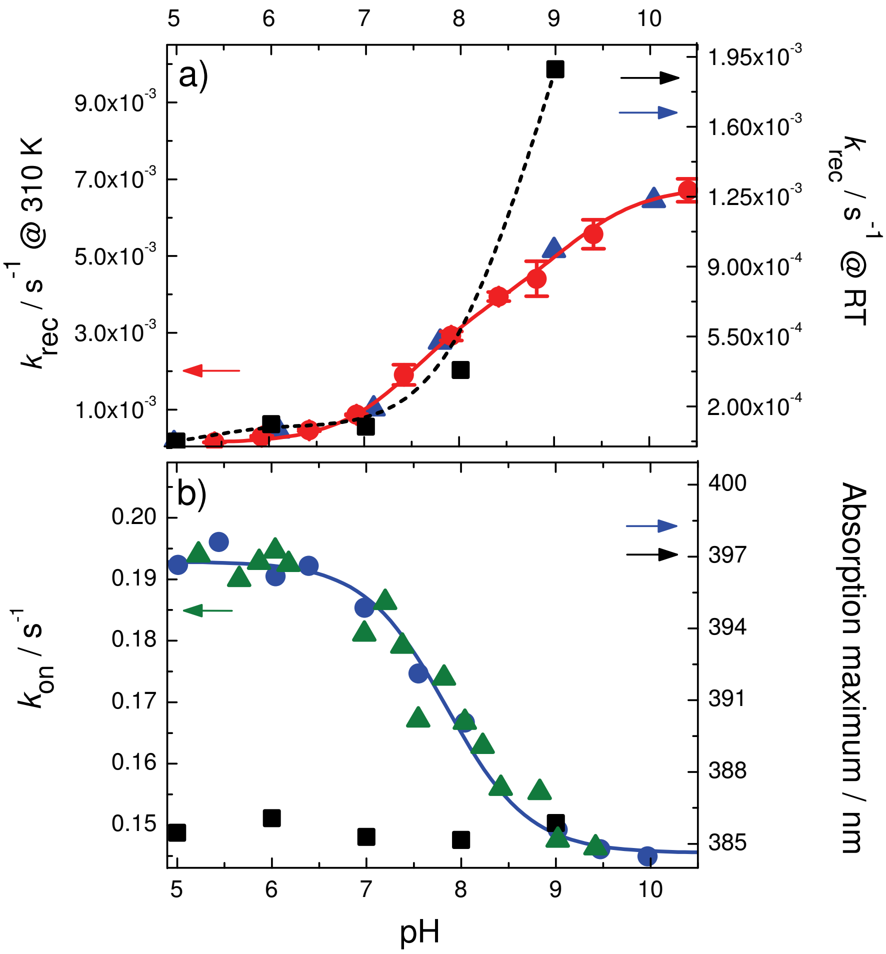

Figure 6.16: pH dependence of the *trans*-to-*cis* isomerization. (a) Thermal recovery: recovery rate coefficient k_{rec} at 290 K (blue triangles) and at 310 K (red circles). The recovery rate coefficient of mIrisGFP E212Q at 310 K is represented by black rectangles. (b) Rate coefficients k_{on} for on switching induced by 405-nm light for $\mathrm{P}_{405} = 13\ \mathrm{mW\,cm^{-2}}$ (green triangles) compared to the peak maximum of $\mathrm{A_t^G}$ of mIrisGFP (blue circles) and mIrisGFP E212Q (black squares).

During the isomerization reaction, $\mathrm{T}^H \rightarrow \mathrm{C}^H$, the $\mathrm{B_c^G}$ band increases, indicating that chromophore deprotonation accompanies *trans*-to-*cis* isomerization, $\mathrm{C}^H \rightarrow \mathrm{C}^-$

(Figure 6.9, gray arrow, marked in red). Because of the high pK_a of the *trans* chromophore, deprotonation prior to isomerization is very unlikely at pH <9 (Section 6.3.2). However, pK_a values >9 have been reported for the *trans* chromophore deprotonation in photoactivatable variants of GFP[147]. This value is comparable to the pK_a of the second step in acceleration of thermal recovery (p$K_\mathrm{a} = 9.5 \pm 0.6$). Thus, the second step is likely due to the actual deprotonation of the *trans* chromophore, which leads to an electrostatic repulsion between the negatively charged phenyl moiety of the *trans* chromophore and the negatively charged Glu144 side chain (Figure 6.17 c). This repulsion promotes chromophore isomerization to the *cis* conformation, which is stabilized by a hydrogen bond to the neutral Ser142 side chain.

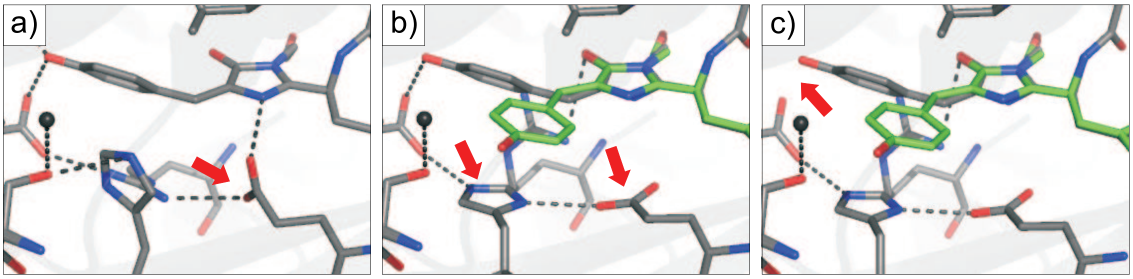

Figure 6.17: Structural rearrangements around the *trans* chromophore upon pH changes. Structural conditions assumed at (a) pH 5, (b) pH 7.8 and (c) pH 9.5. Red arrows indicate structural rearrangements. The structures are reconstructed from green IrisFP in the on- (PDB code: 1VVH) and in the off-state (PDB code: 1VVHI).

Apart from temperature and pH, chromophore isomerization also benefits from a higher flexibility of the quadrupole network[110,153], which might explain the much more drastic acceleration of the thermal recovery at pH >9 in the mIrisGFP Glu212Gln. The higher flexibility of the quadrupole network in this variant is also suggested by its low fluorescence quantum yield, $\phi_\mathrm{fl} = 0.26 \pm 0.01$, given that the quantum yield correlates with the conformational freedom of the chromophore.

6.4.4 Excitation of the Neutral Chromophore

Photoinduced Recovery — On Switching

Recovery of the anionic *cis* chromophore is accelerated by 405-nm illumination. This process, the on switching ($\mathrm{T}^H \rightarrow \mathrm{C}^-$), is about three orders of magnitude faster than thermal relaxation, with $k_\mathrm{on} = (0.17 \pm 0.02)\ \mathrm{s}^{-1}$ ($\mathrm{P}\,(405\,\mathrm{nm}) = 13.3\ \mathrm{mW\,cm}^{-2}$) and $k_\mathrm{rec} = (5.3 \pm 0.1) \times 10^{-4}\ \mathrm{s}^{-1}$ (pH $= 7.8$; Figure 6.16). To facilitate the investigation of on switching, the reactant T^H was populated to the maximum possible level by 473-nm illumination, as described above in Section 6.4.2 (Figure 6.9, green arrows). Subsequently, the sample was exposed to 405-nm light (within the $\mathrm{A}_\mathrm{t}^\mathrm{G}$ band) and the increase in fluorescence at 520 nm was monitored, which is proportional to the amount of anionic *cis* chromophores, C^- (Figure 3.5, Figure 6.9, black arrows, shaded in gray).

Similar to thermal recovery, on switching is a pH-dependent process. The rate coefficient of the photoinduced recovery reaction, k_on, decreases in a single step with $\mathrm{p}K_\mathrm{a} = 7.8 \pm 0.1$. This change is opposite to the previously observed acceleration of thermal recovery with increasing pH, clearly indicating that different reaction pathways exists for thermal relaxation and light-driven on switching, $\mathrm{T}^H \rightarrow \mathrm{C}^-$ (Figure 6.9, black and red arrows). The on switching process is governed by the excitation probability of the neutral *trans* chromophore, $\mathrm{T}^H \rightarrow \mathrm{T}^{H^*}$ (Figure 6.9, black arrows shaded in gray) and, therefore, depends on the extinction coefficient of the neutral *trans* chromophore ε_t ($\mathrm{A}_\mathrm{t}^\mathrm{G}$ band). However, ε_t varies with pH due to a shift of the $\mathrm{A}_\mathrm{t}^\mathrm{G}$ peak position. This shift from 396.8 nm at pH 5 to 384.3 nm at pH 10 can also be described by $\mathrm{p}K_a = 7.8 \pm 0.1$ (Figure 6.16 b), a value that has been associated with deprotonation of Glu212 (Section 6.4.3). Changes in the band position are a result of a coupling of the delocalized π-electron system of the chromophore to changes in the electrostatic environment, such as deprotonation of Glu212. The absorption spectra of the neutral *trans* chromophore in the mIrisGFP variant Glu212Gln show no shift in the $\mathrm{A}_\mathrm{t}^\mathrm{G}$ band, which supports the assignment of $\mathrm{p}K_a$ 7.8 to deprotonation of Glu212. Using Equation 3.11, the quantum yield of on switching is calculated as $\phi_\mathrm{on} = 0.15 \pm 0.01$. It is constant within the pH range 4.5 - 9. Direct deexcitation by photon emission has not been observed, indicating that deexcitation occurs preferentially via non-radiative pathways, which include deprotonation and isomerization. Non-radiative relaxation is possibly favored because the *trans* chromophore is non-planar (Section 4.1.1).

Consequences of the Spectral Overlap Between the Neutral *Cis* and the *Trans* Chromophore Bands

Because of spectral overlap of the absorption bands of the neutral *cis*, C^H, and the neutral *trans* chromophores, T^H ($\lambda_\mathrm{max}(\mathrm{C}^H) = 389$ nm; $\lambda_\mathrm{max}(\mathrm{T}^H) = 391$ nm at pH 7), 405-nm illumination leads to excitation of both neutral chromophore isomers to C^{H^*} and T^{H^*}. Therefore, two competitive reactions are observed upon 405-nm illumination (Figure 6.9). (i) Exciting the non-fluorescent neutral *cis* chromophore leads to a decrease in emission intensity (off switching). (ii) Exciting the non-fluorescent neutral *trans* chromophore, T^H, leads to an increase in the emission intensity (on switching).

According to Figure 6.9, excitation of the neutral *cis* chromophore, $C^H \rightarrow C^{H^*}$, triggers isomerization to yield the *trans* chromophore (reaction (i)). Due to the pH equilibrium of the *cis* chromophore, $C^- + H^+ \rightleftharpoons C^H$, the fluorescent anionic *cis* chromophore, C^-, is depleted concomitantly and, therefore, the emission intensity decreases (off switching; Figure 6.9, blue arrows). The *cis*-*trans* transition upon 405-nm illumination is also visible in changes of the absorption spectrum (Figure 6.18). The depletion of the anionic *cis* chromophore results in a loss in the B_c^G-band amplitude. As neutral *trans* chromophore is formed, an increase in the neutral chromophore band is expected. However, the neutral chromophore band represents a superposition of the increasing A_t^G and the decreasing A_c^G bands. Thus, the net change in the amplitude of the neutral chromophore band is the sum of the individual amplitude changes in A_t^G and A_c^G, representing the changes in the fractions of C^H and T^H corresponding to their respective extinction coefficients ($\varepsilon_t\,(405\,\mathrm{nm}) = (12{,}000 \pm 1{,}600)\ \mathrm{M}^{-1}\,\mathrm{cm}^{-1}$; $\varepsilon_c\,(405\,\mathrm{nm}) = (20{,}700 \pm 2{,}000)\ \mathrm{M}^{-1}\,\mathrm{cm}^{-1}$).

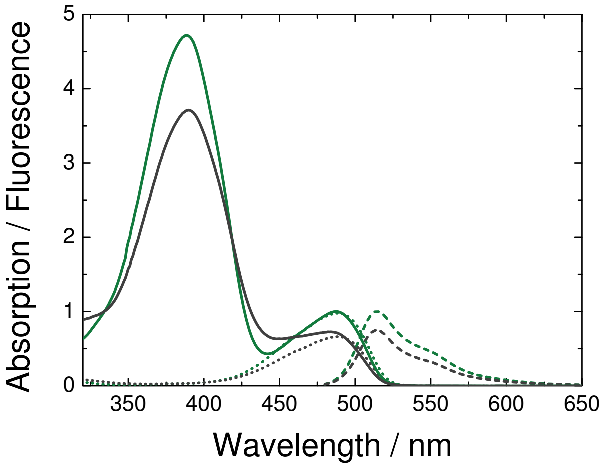

Figure 6.18: Spectral changes upon off switching with 405-nm light. Absorption (solid), emission (dashed; excited at 470 nm) and excitation (dotted; recorded for emission at 540 nm) spectra of mIrisGFP at pH 4.6 were recorded before (green) and after (gray) 405-nm illumination (20 s, 20 mW cm^{-2}).

Excitation of the neutral *trans* chromophore induces *trans*-to-*cis* isomerization (reaction (ii)) (Figure 6.9, black arrows in gray), as described previously (Section 6.4.4). This reaction is governed by the excitation probability of the neutral *trans* chromophore, T^H, as was demonstrated by the impact of the extinction coefficient on the on switching kinetics (Section 6.4.4).

The simultaneous activation of both reactions (i and ii, Figure 6.9 blue and gray marked arrows) upon 405-nm illumination leads to a photoinduced equilibrium

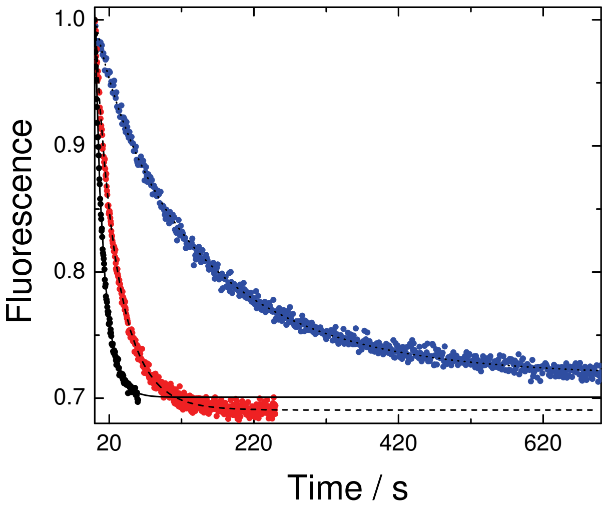

Figure 6.19: Time traces of the emission intensity during off switching with 405-nm light. Time traces recorded during illumination of mIrisGFP (pH 5.3, ionic strength 150 mM) with 405-nm light of 0.9 mW cm^{-2} (blue), 8 mW cm^{-2} (red), and 20 mW cm^{-2} (black).

between the neutral chromophores ($C^H \rightleftharpoons T^H$; Figure 6.19). This equilibrium is determined by the ratio of the respective reaction rate:

$$C^{H} \underset{k_{tc}}{\overset{k_{ct}}{\rightleftharpoons}} T^{H} \tag{6.2}$$

whereas $k = \phi\,\varepsilon$.

As described in Section 6.4.2, the equilibrium coefficient is related to the residual fluorescence upon continuous illumination and is given by the ratio of the rate coefficients for the forward and backward reactions, k_{ct}/k_{tc} (Equation 6.2). For 405-nm illumination at pH 5.3 the fluorescence decreases to $\sim 70\,\%$. Since the rate coefficient of the forward reaction k_{ct} (405 nm), and, therefore, the quantum efficiency, ϕ_{ct}, is coupled to the pH equilibrium of the *cis* chromophore (Section 6.4.2), an apparent equilibrium constant K (405 nm) is observed. The experimental conditions for the $C^H \rightarrow T^H$ and the $T^H \rightarrow C^H$ transitions are identical as they occur simultaneously. Thus, the same power density P is driving both reactions and, therefore, Equation 3.10 reduces to $k = \phi\,\varepsilon\,\text{const.}$ and the equilibrium constant K (405 nm) can be described by

$$K\,(405\,\text{nm}) = \frac{k_{ct}}{k_{tc}} = \frac{\phi_{ct}\,\varepsilon_c}{\phi_{tc}\,\varepsilon_t} = \frac{[T^H]}{[C^H]} = \frac{[30\,\%]}{[70\,\%]} = 0.41 \pm 0.05 \tag{6.3}$$

The off switching quantum efficiency of C^H, ϕ_{ct} (405 nm), is then given by

$$\phi_{\mathrm{ct}} \;=\; \phi_{\mathrm{tc}}\, K\,(405\,\mathrm{nm})\, \frac{\varepsilon_t}{\varepsilon_c} \tag{6.4}$$

Assuming that *cis*-to-*trans* isomerization can be neglected during on switching, $\phi_{\mathrm{on}} \sim \phi_{\mathrm{tc}} = 0.15 \pm 0.01$ (Section 6.4.4). The extinction coefficients of T^H and C^H have been determined for 405 nm with $\varepsilon_t = (12{,}000 \pm 1{,}600)\ \mathrm{M}^{-1}\,\mathrm{cm}^{-1}$ and $\varepsilon_c = (20{,}700 \pm 2{,}000)\ \mathrm{M}^{-1}\,\mathrm{cm}^{-1}$, respectively. Therefore, the quantum efficiency ϕ_{ct} (405 nm) is calculated with 0.036 ± 0.008, suggesting that off switching via the anionic chromophore C^- (ϕ_{off} (473 nm) ~ 0.003) is 10-fold less efficient than off switching via the neutral chromophore C^H at pH 5.3.

6.5 Energetic Interpretation: Interconversion of the Chromophore Species on the Microscopic Level

Up to now, photoswitching has been discussed with the main focus on the outcome of a particular photoactivation pathway. To get insight into the details of photoswitching, the chromophore transitions are discussed in the following from the energetic point of view. To this end, Figure 6.9 has been rearranged to match the energy levels of the respective chromophore states (Figure 6.20). Nomenclature and color coding of Figure 6.20 are identical to those in Figure 6.9. The relative energy levels of the ground state species are based on the pK_a values of the chromophore protonation reactions. The levels of the excited states with respect to the ground states are based on the absorption maxima of the individual species. The absorption spectrum of the anionic *trans* chromophore could not be extracted with the experimental methods used here. However, pH-jump experiments with photoswitchable mutants of GFP[147], femtosecond time-resolved spectroscopic studies with asFP595[154] and MD simulations[124] indicate that the absorption of the *trans* isomer is slightly blue shifted compared to that of the *cis* isomer. This slight blue shift is therefore assumed for the arrangement of T^- in Figure 6.20, which translates into a slightly larger S_0-S_1 energy difference for the anionic *trans* chromophore than for the anionic *cis* chromophore.

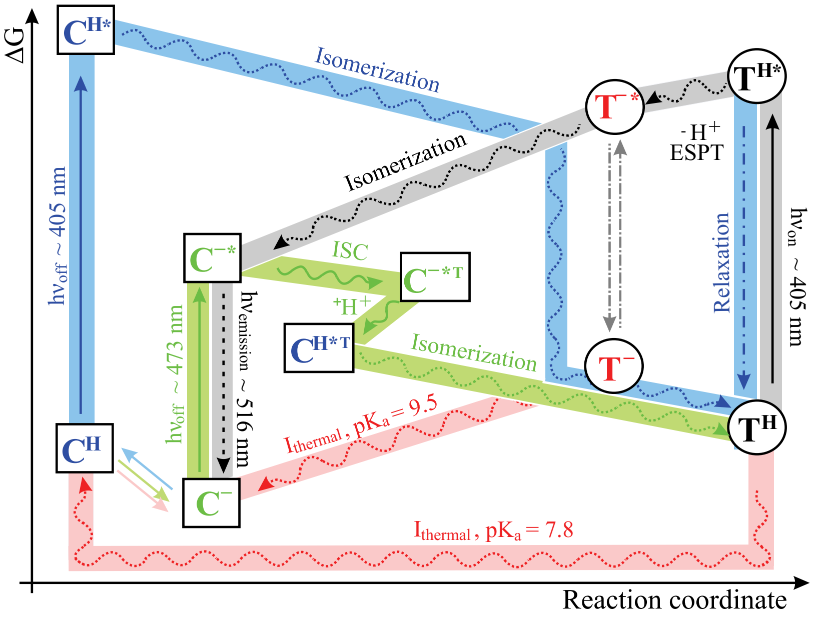
ΔG
C^{H*}
Isomerization
T^{H*}
T^{-*}
Isomerization
-H+
ESPT
$h\nu_{off}$ ~ 405 nm
C^{-*}
ISC
C^{-*T}
+H+
C^{H*T}
Isomerization
T^-
Relaxation
$h\nu_{on}$ ~ 405 nm
$h\nu_{off}$ ~ 473 nm
$h\nu_{emission}$ ~ 516 nm
$I_{thermal}$, pK_a = 9.5
T^H
C^H
C^-
$I_{thermal}$, pK_a = 7.8
Reaction coordinate

Figure 6.20: Isomerization/protonation pathways in mIrisGFP from the energetic point of view. Excitation (solid), isomerization (dotted), non-radiative relaxation (dash-dotted) and fluorescence (dashed) transitions are illustrated by arrows. The color coding is in accordance with Figure 6.9. Intersystem crossing is abbreviated by ISC; excited state proton transfer by ESPT.

6.5.1 Exciting the Anionic *Cis* Chromophore - Along the 'Green Pathway'

Studies of *cis*-to-*trans* isomerization upon 473-nm illumination of mIrisGFP have shown that the reaction efficiency is determined by the concentration of the reactants and by the ratio of the excitation probabilities (ε (473 nm)) of the chromophore species present (Section 6.4.2). For thermally relaxed mIrisGFP at physiological pH, 473-nm illumination leads primarily to excitation of the anionic *cis* chromophore, C^-, to its excited state, C^{-*}. The high emission quantum yield, $\phi_{fl} = 0.63 \pm 0.06$, indicates that relaxation of the anionic *cis* chromophore occurs predominantly by emitting a photon. However, $C^{-*} \rightarrow C^-$ does not affect the concentration of the reactant of the off switching, C^-. Non-radiative relaxation may occur by chromophore isomerization. As described in Section 6.4.2, the *cis*-to-*trans* photoswitching at physiological pH is accompanied by chromophore protonation, $C^- \rightarrow T^H$. Based on the previous assumptions, C^{-*} is energetically lower-lying than C^{H*} (Figure 6.20). Thus, protonation of C^{-*} would involve an 'uphill transition', which would also hold true for the isomerization to T^{-*}. Additionally, quantum-chemical calculations predicted a high barrier for isomerization of the anionic *cis* *p*-HBI chromophore by rotation around the C_α-C_β bond *in vacuo*[98]. Instead, Weber *et al.* suggested a non-adiabatic crossing (NAC) for isomerization in proteins. In mIrisGFP, off switching is temperature dependent. It accelerates from $k_{\mathrm{off}} = (3.2 \pm 0.6) \times 10^{-2}\ \mathrm{s}^{-1}$ at 275 K to $k_{\mathrm{off}} = (6.8 \pm 0.04) \times 10^{-2}\ \mathrm{s}^{-1}$ at 306 K, measured with 38 mW cm^{-2} (Figure 6.21) and involves crossing an activation energy barrier, E_A, of 15.5 ± 1.5 kJ/mol. This barrier might indicate that the S_0 and S_1 energy surfaces approach each other at the energy maximum of both potentials such that a barrier has to be crossed for NAC. Alternatively, NAC might involve intersystem crossing to the first triplet state, C^{-*T}. The triplet state C^{-*T} has a higher proton affinity[155,156] so that protonation might occur. Isomerization and deexcitation would then result in the neutral *trans* chromophore, T^H. This hypothesis may also explain the low off switching quantum efficiency, ϕ_{off} (473 nm, pH 7) $= (4.5 \pm 0.4) \times 10^{-3}$. This conclusion is in agreement with models previously proposed for Dronpa[157].

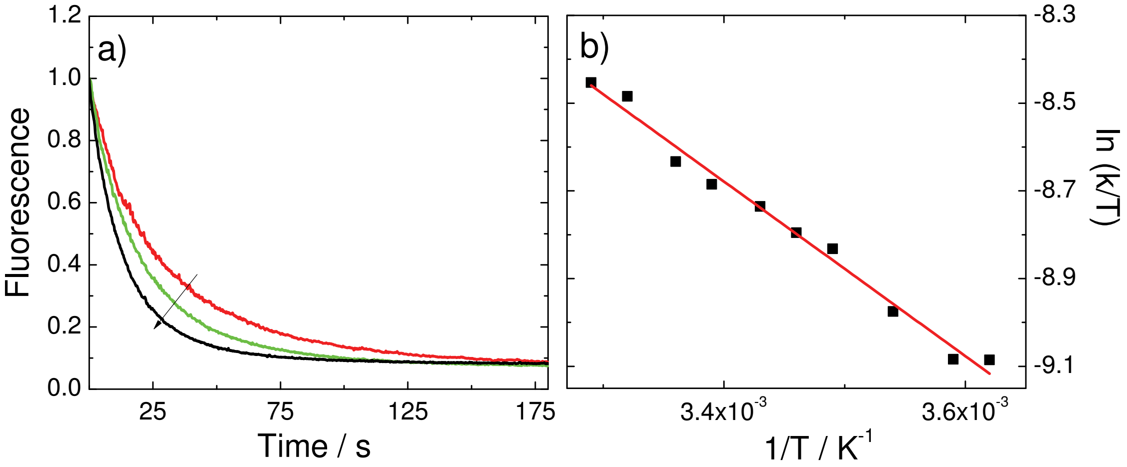

Figure 6.21: Temperature sensitivity of the off switching. (a) Fluorescence intensity at 520 nm during 473-nm illumination (38 mW cm^{-2}) was recorded at 275 (red), 287 (green) and 306 K (black), respectively. The arrow indicates increasing temperature. (b) Eyring plot for 275 K to 303 K ($P_{473} = 38$ mW cm^{-2}).

Chasing the Triplet State

To provide evidence for the previously discussed hypothesis we tried to trap the triplet state. An mIrisGFP solution was cooled to 15 K in buffer containing 75 % glycerol as a cryoprotectant, to inhibit non-radiative relaxation. Excitation with

473-nm light did not yield an additional emission band associated with triplet emission (Figure 6.22).

According to our assumption, the triplet state should feature a lower pK_a value and, therefore, protonate to C^{H*} (T_1)[155]. Triplet emission of C^{-*} (T_1) might be very weak and potentially overlap with the emission of the anionic *cis* chromophore, C^{-}. Faro *et al.* monitored the spectral evolution of the absorption of tetrameric green IrisFP upon continuous 488-nm illumination (356 $\mathrm{W\,cm^{-2}}$) at 100 K[158]. The low temperature prevents chromophore isomerization to the *trans* state. Even so, a neutral chromophore band arises. We suggest that it originates from the accumulated triplet state of the *cis* chromophore in its protonated form.

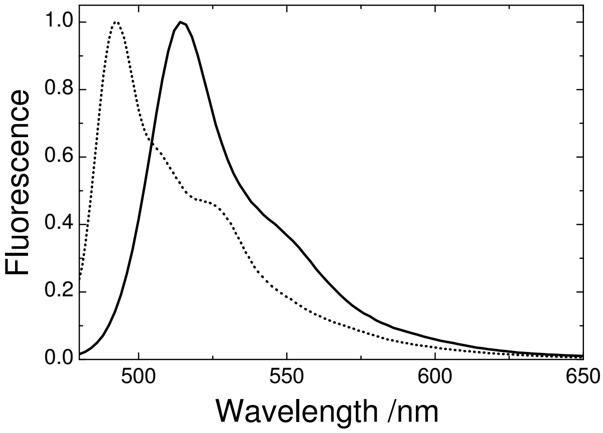

Figure 6.22: Temperature dependence of the emission spectrum. Emission spectra were recorded at 290 K (solid) and 15 K (dotted) by excitation at 470 nm. The protein was diluted in 20 mM pH 7 buffer, containing 75 % glycerol.

Fluorescence correlation spectroscopy yielded an autocorrelation curve that clearly showed a fast decay time in the microsecond time range (Figure 6.23). However, this decay cannot be assigned explicitly to the triplet state kinetics because a chemical chromophore photoconversion, i.e. *cis*-to-*trans* isomerization, could have the same effect on the autocorrelation curve. Dedecker *et al.* have shown for Dronpa that the microsecond phase observed in the autocorrelation function represents the survival time of the fluorescent chromophore species[150].

For the triplet state of chromophores in GFP-like fluorescent proteins, lifetimes in the micro- to millisecond range have been reported[150]. Since the interaction with oxygen facilitates the generation of the triple state dynamically the triplet state increasingly accumulates with rising temperature[155]. We measured the off switching kinetics with and without oxygen present in the buffer solution at 290 and 310 K. Essentially no effect was seen at 290 K (k_{off} (aerob) $= 0.045 \pm 0.002\,\mathrm{s^{-1}}$, k_{off} (anaerob) $= 0.041 \pm 0.002\,\mathrm{s^{-1}}$, $\mathrm{P}_{473} = 10\ \mathrm{mW\,cm^{-2}}$). However, a significant ef-

Figure 6.23: Autocorrelation curve of mIrisGFP. Mean correlation of 12 traces integrated over 15 s, respectively. The curves were measured on a ~30 nm protein solution at pH 7 under 3 µW 488-nm illumination using a 60×/1.2w water immersion objective.

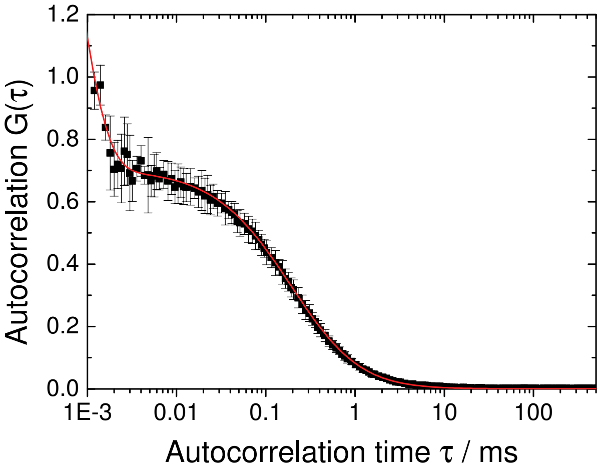

fect was not expected since the probability for intersystem crossing from the excited singlet state to the triplet state is typically $<0.1\,\%$ at 290 K[125]. At higher temperatures, the collision probability between oxygen and the chromophore increases, which may enhance the net transition probability for $S^1 \rightarrow T^1$. Thus, the experiment was repeated at 310 K, which yielded an increase of the off switching rate coefficient in the presence of oxygen (k_{off} (aerob) $= 0.063 \pm 0.002$ s^{-1}), while the off switching rate in the absence of oxygen was not affected by the temperature (k_{off} (anaerob)$= 0.041 \pm 0.002$ s^{-1}). This result supports the hypothesis that the triplet state is visited during off switching. The possibility of intersystem crossings in EosFP variants such as mIrisGFP is also supported by excited-state QC/MM simulations. Lelimousin *et al.* have recently proposed that two intersystem crossings (ISC) occur in EosFP during irreversible photoconversion from the green to the red fluorescent state[112]. The intriguing possibility that protonation of the *cis* chromophore occurs in the triplet state was already mentioned by Mizuno and coworkers[125], referring to a single-molecule study of Dronpa[148].

6.5.2 Thermal Recovery of the *Cis* Chromophore - Along the 'Red Pathway'

Thermal recovery of the anionic *cis* chromophore, C^-, (6.20, red arrows) is a rather slow process (Section 6.4.3). Overall, the reaction becomes faster with increasing pH because the *trans* conformation is destabilized by (i) deprotonation of Glu212 (p$K_a = 7.8$) and (ii) deprotonation of the chromophore phenyl ring (p$K_a \sim 9.5$). The neutral *trans* chromophore, T^H, is stabilized by a hydrogen bond to Glu144. Its

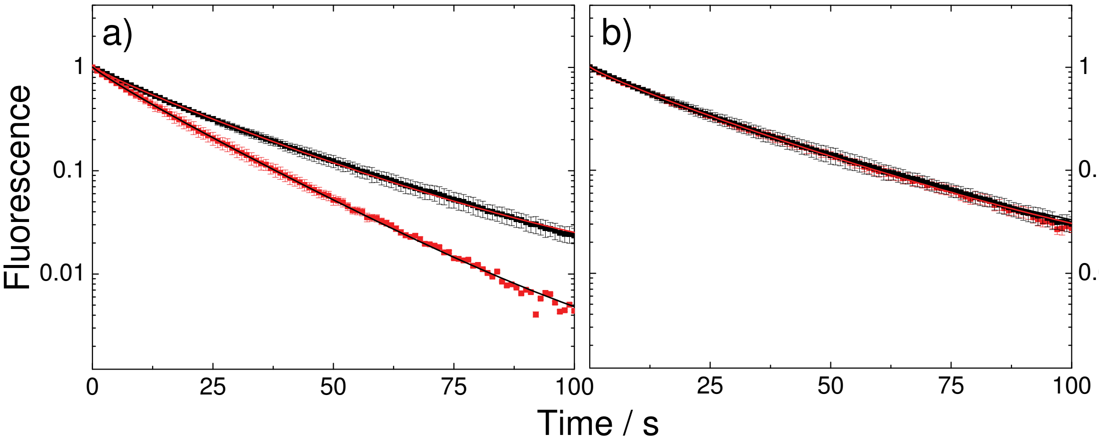

Figure 6.24: Off switching in the presence and absence of molecular oxygen. Off switching was recorded in pH 7 buffer solution at 290 K (black) and at 310 K (red) (a) in the presence and (b) in the absence of oxygen. Average of 6 independent measurements are represented by symbols; the respective standard deviations are indicated by error bars. Oxygen was removed by purging 500 µl of the dilute protein solution with nitrogen for 15 min. The data were fitted with a stretched exponential function (red (black) line).

thermal recovery is expected to take longer than the recovery of the anionic *trans* chromophore, T^-, which is destabilized by electrostatic repulsion of the negatively charged Glu144. Therefore, we assume different relaxation pathways for anionic and neutral *trans* chromophores, as indicated by red arrows in Figure 6.20.

6.5.3 Exciting the Neutral *Cis* Chromophore - Along the 'Blue Pathway'

Excitation of the neutral *cis* chromophore, $C^H \rightarrow C^{H*}$, is achieved by 405-nm illumination. Relaxation of C^{H*} occurs only rarely by emitting a photon ($\phi_{\text{fl}} < 0.03$). Even though it may seem energetically favorable (Figure 6.20), deexcitation by ESPT is also negligible, since the excitation spectrum presents essentially no signal within the spectral range of the neutral band of the *cis* chromophore, A_c^G (Figure 6.6). Furthermore, the minor emission in the anionic band at 516 nm observed upon excitation within the A_c^G band decreases upon lowering the pH, indicating that no anionic emission is induced by excitation of the neutral *cis* chromophore and subsequent ESPT. Apparently, there is no proton acceptor available when the chromophore is in the *cis* conformation. Therefore, we suggest that relaxation of the excited neutral *cis* chromophore occurs preferentially by non-radiative pathways such as internal conversion or isomerization. *Cis-trans* isomerization of the excited neutral p-HBI chromophore is associated with a stabilization by $\sim 84\,\mathrm{kJ/mol}$[98]. In proteins, this process might occur in the excited state, $\mathrm{C}^{H^*} \rightarrow \mathrm{T}^{H^*}$, or via NAC to the *trans* ground state, $\mathrm{C}^{H^*} \rightarrow \mathrm{T}^{H}$, being more likely according to quantum chemical calculations[98]. For exited-state isomerization, $\mathrm{C}^{H^*} \rightarrow \mathrm{T}^{H^*}$, the following situation has to be considered. T^{H^*} may relax by ESPT to T^{-^*} and subsequently isomerize to C^{-*}. Emission of a photon would yield the *cis* anionic ground state, C^{-} (Figure 6.20, gray arrows). However, the net fluorescence would not change as the total fraction of *cis* chromophores remains constant. Relaxation of the excited neutral *trans* chromophore to the ground state, $\mathrm{T}^{H^*} \rightarrow \mathrm{T}^{H}$, results in depopulation of the neutral *cis* chromophore. Because of the ground state pH-equilibrium of the *cis* isomer, $\mathrm{C}^{H} \rightleftharpoons \mathrm{C}^{-}$, the fraction of anionic *cis* chromophores is reduced concomitantly with that of the neutral ones. As a result, the fluorescence decreases (off switching). The higher quantum yield of off switching via the neutral *cis* chromophore, $\phi_{\mathrm{off}}\ (405\,\mathrm{nm}) = 0.036 \pm 0.008$, as compared to off switching via the anionic *cis* chromophore, $\phi_{\mathrm{off}}\ (405\,\mathrm{nm}) \sim 0.003$, might be based on the higher probability for NAC of $\mathrm{S}_1\ (\mathrm{C}^{H^*}) \rightarrow \mathrm{S}_0\ (\mathrm{T}^{H})$ compared to NAC of $\mathrm{S}_1\ (\mathrm{C}^{-^*}) \rightarrow \mathrm{S}_0\ (\mathrm{T}^{H})$ or $\mathrm{S}_1\ (\mathrm{C}^{-^*}) \rightarrow \mathrm{T}_1\ (\mathrm{C}^{-^*})$, respectively, as suggested by an activation barrier (Figure 6.21) and Weber *et. al*[98].

6.5.4 Exciting the Neutral *Trans* Chromophore - Along the 'Gray Pathway'

Relaxation of the neutral *trans* chromophore, T^{H}, to the *cis* chromophore can be accelerated markedly by exciting the neutral *trans* chromophore, e.g., by illumination with 405-nm light (Section 6.4.4, Figure 6.12). Direct isomerization from T^{H*} to C^{H*}, is energetically not favorable (Figure 6.20). We therefore suggest that the excited neutral *trans* chromophore undergoes ESPT, $\mathrm{T}^{H*} \rightarrow \mathrm{T}^{-^*}$, followed by isomerization to the anionic *cis* chromophore, C^{-*} and subsequent deexcitation to the C^{-} ground state via photon emission (on switching; Figure 6.20, gray arrows). The most likely proton acceptor in mIrisGFP is Glu144, which is initially deprotonated and hydrogen-bonded to the *trans* chromophore hydroxyphenyl ring. In ultrafast transient absorption experiments on Dronpa, ESPT has also been identified as the first step of photoinduced on switching from the non-fluorescent to the fluorescent state, $\mathrm{T}^{H} \rightarrow \mathrm{C}^{-}$ (according to the nomenclature used here)[157]. In these studies, an intermediate state, I, has been introduced in the resulting mechanistic model of Dronpa. This intermediate state, I, might be identical to the T^{-*} state.

6.6 Summary and Conclusions

mIrisGFP exhibits three different photoreactions. Exciting the anionic and the neutral *cis* chromophore results in off switching, while excitation of the neutral *trans* chromophore reverses the reaction (on switching). The anionic *trans* chromophore is only marginally populated below pH 9, hence, on switching by exciting the anionic *trans* chromophore could not be observed. We have described the relation between the individual photoreactions in an eight-state model (Figure 6.9). It illustrates the extensive interdependence of the individual photoreactions caused by the ground state equilibria. Considering, in addition, the spectral overlap of the absorption bands of the individual chromophore species, the model demonstrates that excitation with wavelengths in a wide interval of the violet-green spectrum induces more than one photoreaction. The efficiency of a particular photoreaction is determined by the relative probabilities of exciting the involved chromophore species at the respective excitation wavelength and the ratio of the rate coefficients for the respective process. Both parameters depend on the $\mathrm{p}K_a$ values of the *cis* and *trans* chromophores and the relative extinction coefficients.

Even though mIrisGFP lacks the fourth pathway, namely the on switching via the anionic *trans* chromophore, $\mathrm{T}^- \rightarrow \mathrm{C}^-$, this transition is quite common in photoswitchable FPs with positive switching mode (Section 1.3.2)[131,124]. Here, mainly the non-fluorescent anionic *trans* chromophore, T^-, is stabilized in thermal equilibrium. Its excitation triggers isomerization to the *cis* state, which is brightly fluorescent in its anionic form.

In summary, we believe that, with adjustments of the relative energy levels in Figure 6.20 according to the biophysical properties of a particular protein, this simplified model might be generally applicable to describe reversible photoactivation in FPs.

The homology between mIrisGFP and mIrisFP suggests that the results, shown here, are directly applicable to mIrisFP. For example, the various photoequilibria in mIrisGFP emphasize the importance of the excitation wavelength for the off switching efficiency. The latter could be significantly increased by using a 488-nm laser line instead of a 473-nm laser. The lack of photoinduced recovery at 488 nm might require much lower laser intensities in PALM applications than for experiments with a 473-nm laser. Other parameters to modulate the level of fluorescent molecules are temperature and pH. This implies that imaging of the same sample at different temperatures or in different cellular compartments of the cells might require adjustment of the experimental parameters, such as the laser intensities. For experiments that do not require a certain temperature, cooling the sample will increase the level of molecules in the off-state, which again will allow application of lower laser intensities and, therefore, may increase the number of photons emitted per molecule.

Summary

In this work, we have presented a new PAFP, which combines several photoactivation modes and, thereby, allows combination of pulse chase experiments and superresolution imaging. Derived from EosFP by substitution of two amino acids, Phe191Leu and Phe173Ser, this variant utilizes three different photoactivation pathways: irreversible green-to-red photoconversion, and reversible photoswitching between a bright and a dark state, both in the green and the red forms.

Off switching of the green form is achieved by 488-nm illumination. Recovery of the bright state occurs thermally, but can also be significantly accelerated by 405-nm illumination (on switching). Continuous illumination with high-intensity 405-nm light leads to green-to-red photoconversion. Off switching of the red form can be achieved by 532-nm illumination and reversed by 440-nm light.

The two pathways available upon illumination of the green form with 405-nm light, on switching of the green form and green-to-red photoconversion, are individually controllable. This control results from differences in the efficiencies and rates of the two reaction pathways. Off switching occurs concomitantly with *cis*-to-*trans* isomerization of the chromophore and other extensive structural rearrangements of several amino acid chains in the chromophore vicinity. Among those, there is a flip of the Glu212 side chain by $\sim 90°$. Glu212 supposedly acts as an acid-base catalyst in green-to-red photoconversion[34], a function that is prohibited by a conformational change. As a result, the probability of green-to-red photoconversion is very low. Perhaps more significant for practical applications is the fact that the quantum efficiency of the on switching reaction of the green form is two orders of magnitude higher than that for green-to-red photoconversion. Hence, on switching occurs efficiently even at very low laser intensities, while green-to-red photoconversion will not happen to any significant extent under these conditions. This inefficiency forms the basis of the control, as irreversible green-to-red photoconversion can be achieved under very high intensities.

The presence of three photoactivation pathways in IrisFP enables novel applications, including pulse-chase experiments with superresolution. However, the tetrameric oligomerization state of the protein may adversely affect the performance of chimeric fusion proteins. The formation of oligomers of the IrisFP-fusion tag may influence the dynamics and localization of the target protein, potentially invalidating the results. Therefore, we generated a monomeric version of this protein, mIrisFP, by a combined approach of random and site directed mutagenesis, based on a monomeric template of EosFP, mEosFP*thermo*. The resultant protein, mIrisFP, features basically the same photophysical properties as the tetrameric version. The maximum absorption and emission of the green form occurs at 486 and 516 nm, respectively. Its molecular brightness is comparable to other green photoswitchable FPs and even achieves $\sim 80\,\%$ of the molecular brightness reported for EGFP (molecular brightness: mIrisFP $\sim 25.5 \times 10^3$, EGFP $\sim 33.0 \times 10^3$) [81]. Compared to the green form, the spectra of red mIrisFP are ~ 20 nm bathochromically shifted, featuring maximum absorption and emission at 546 and 578 nm, respectively. Its molecular brightness is $\sim 40\%$ lower than that of the red form of mEos2; yet, it almost matches the molecular brightness of the brightest red photoswitchable FP, PATagRFP (molecular brightness: mIrisFP $\sim 19.3 \times 10^3$, mEos2 $\sim 30.4 \times 10^3$, PATagRFP $\sim 25.1 \times 10^3$) [81]. The individual pathways of photoactivation are identical for IrisFP and mIrisFP. mIrisFP performs excellently as a genetically encoded marker in protein fusions.

In PALM experiments, the number of photons per molecule collected from mIrisFP in both the green and red forms is comparable with other monomeric PAFPs [118]. Still, the performance of mIrisFP may yet be further improved by a deeper understanding of the photophysics of the individual photoreaction. To this end, we performed a detailed photophysical characterization of the photoactivation in a mIrisFP analogue, which is only marginally photoconvertible in solution, mIrisGFP. The experiments demonstrate that several reactions must be considered for a full examination of the photoswitching process. We summarized the chromophore species involved in each state, and the transitions between them in an 8-state-model, which demonstrates the extensive interdependence of the photoreactions on the ground state equilibria. Off switching occurs by excitation of either the neutral or the anionic *cis* chromophore (bright state). The rate of this reaction is governed by the adjustment of the equilibrium between the two species. We did not observe a protonation equilibrium of the *trans* chromophore (dark state), indicating a very high pK_a value for this species. Excitation of the neutral *trans* chromophore accelerates the recovery of the *cis* state. The absorption bands of individual chromophore species overlap significantly. Consequently, illumination with a particular wavelength simultaneously induces photoreactions in both directions. However, the efficiency of the individual photoreactions varies, depending on the relative probabilities to excite the involved chromophore species at the respective excitation wavelength and the ratio of the rate coefficients of the respective process. Both parameters are affected by the ground-state pH equilibrium.

Owing to the homology between mIrisGFP and mIrisFP, these results may be directly applicable to the improvement of mIrisFP for PALM experiments. For example, occurrence of simultaneous off- and on switching can be minimized by avoiding an off switching excitation wavelength in the range of the overlap between neutral *trans* and anionic *cis* chromophore. Off switching of the green (red) form of mIrisFP could be enhanced using wavelengths $> 480\,\mathrm{nm}$ ($> 560\,\mathrm{nm}$). This approach may significantly reduce the laser powers required for depleting emission at the single molecule level in PALM. While the laser power will have only a marginal effect on the fraction of molecules in the bright state if utilizing the appropriate excitation wavelength (without spectral overlap between anionic *cis* and neutral *trans* chromophore), the fraction of bright molecules is significantly affected by temperature and pH. Hence, imaging of structures in different cellular compartments of the same sample at different temperatures or imaging different cellular compartments might require adjustment of the experimental parameters.

The improved understanding of the photophysical mechanisms involved in photoactivation may guide the engineering of enhanced PAFPs and help to improve the spatial resolution in superresolution experiments, approaching the theoretical limit of the size of the labeling tag.

Zusammenfassung

Die Anfärbung intrazellulärer Strukturen in lebenden Zellen mit fluoreszenten Proteinen (FPs) erlaubt höchste Markierungspräzision und erfordert nur minimale Eingriffe in die Physiologie der Zelle. Im letzten Jahrzehnt gewann eine Gruppe FPs zunehmend an Bedeutung, deren Fluoreszenzeigenschaften mit Hilfe von Licht reguliert werden können. Durch Beleuchtung mit Licht einer bestimmten Wellenlänge ändern diese Proteine beispielweise ihre Farbe (Photokonversion) oder wechseln zwischen einem hell fluoreszierenden An- und einem dunklen Aus-Zustand (*Photoswitching*). Auf diese Weise kann ein Teil einer Molekülpopulation selektiv hervorgehoben werden, beispielsweise um deren Verhalten über einen bestimmten Zeitraum zu untersuchen (*Pulse-Chase* Analyse)[7,8]. Die Photoaktivierung einzelner Moleküle wird auch für hochauflösende Fluoreszenz-Bildgebungsverfahren verwendet, mit deren Hilfe selbst Strukturen kleiner 100 nm aufgelöst werden können[9–13]. Jedes einzelne dieser Experimente erfordert bereits mindestens zwei optisch unterscheidbare Zustände. Die Kombination aus *Pulse-Chase* Analyse und hochauflösender Bildgebung ist daher nur möglich, wenn MEHR als zwei Zustände des Proteins photoinduzierbar sind. Das Ziel dieser Arbeit war es daher, ein Protein zu entwickeln, das mehrere Photoreaktionen zeigt, die jeweils zu unterschiedlichen Emissionszuständen führen. Eine Zufallsmutante von EosFP, IrisFP (EosFP Phe173Ser, Phe191Leu), zeigt drei verschiedene Photoreaktionen: irreversible Photokonversion einer grün emittierenden in eine rot emittierende Form und reversibles *Photoswitching*, sowohl der grünen als auch der roten Form[120]. Die Kombination mehrerer Photoaktivierungswege in IrisFP ermöglicht die Untersuchung dynamischer Prozesse mit nanoskalarer Auflösung. Allerdings kann der tetramere Oligomerisierungszustand von IrisFP die Funktionalität eines chimären Fusionsproteins beeinträchtigen. Es wurde daher eine monomere Variante generiert, mIrisFP, die grundsätzlich die gleichen photophysikalischen Eigenschaften zeigt wie tetrameres IrisFP. Die grüne Form erreicht 80% der molekularen Helligkeit von EGFP und auch die rote Form reicht in der Helligkeit an andere rot-fluoreszierende photoaktivierbare FPs heran[81]. Außerdem eignet sich mIrisFP hervorragend als Fusionspartner in Proteinchimären und erreicht in PALM-Experimenten sowohl in der grünen als auch in der roten Form Photonenausbeuten, die mit denen anderer monomerer photoaktivierbarer FPs vergleichbar ist[118].

Ein besseres Verständnis der zugrunde liegenden Photoaktivierungsreaktionen könnte zur weiteren Verbesserung der Experimente mit mIrisFP beitragen. Deshalb wurde eine detaillierte photophysikalische Charakterisierung eines mIrisFP Analogon, mIrisGFP, durchgeführt. Aus diesen Untersuchungen geht hervor, dass die Beleuchtung mit einer bestimmten Wellenlänge gleichzeitig die Umschaltung des An- und des Aus-Zustandes induziert, was zu einer Überlagerung von Fluoreszenzzu- und abnahme führt. Die Nettoreaktion hängt dabei von den relativen Anregungswahrscheinlichkeiten der beteiligten Chromophorspezies und der Quanteneffizienz der jeweiligen Prozesse ab, wobei beide Parameter von Grundzustandsgleichgewichten beeinflusst werden. Aufgrund der Homologie zwischen mIrisGFP und mIrisFP können diese Ergebnisse direkt für die Verbesserung von PALM-Experimenten mit mIrisFP angewandt werden, beispielsweise zur Minimierung der notwendigen Laserleistung durch Auswahl geeigneter Anregungswellenlängen.

Die vorliegenden Ergebnisse liefern ein detailliertes Bild der photophysikalischen Prozesse während der Photoaktivierung, das einen entscheidenden Beitrag zur Optimierung von photoaktivierbaren FPs und zur Weiterentwicklung von FP basierten hochauflösenden Fluoreszenz-Bildgebungsverfahren leisten kann.

Bibliography

[1] D.M. Chudakov, M.V. Matz, S. Lukyanov, and K.A. Lukyanov. Fluorescent proteins and their applications in imaging living cells and tissues. *Physiol. Rev.*, 90(3):1103–1163, 2010.

[2] D.M. Chudakov, S. Lukyanov, and K.A. Lukyanov. Fluorescent proteins as a toolkit for in vivo imaging. *Trends Biotechnol.*, 23(12):605–613, 2005.

[3] T. Nagai, S. Yamada, T. Tominaga, M. Ichikawa, and A. Miyawaki. Expanded dynamic range of fluorescent indicators for Ca^{2+} by circularly permuted yellow fluorescent proteins. *Proc. Natl. Acad. Sci. U. S. A.*, 101(29):10554–10559, 2004.

[4] N. Heim and O. Griesbeck. Genetically encoded indicators of cellular calcium dynamics based on troponin C and green fluorescent protein. *J. Biol. Chem.*, 279(14):14280–14286, 2004.

[5] G.T. Hanson, T.B. McAnaney, E.S. Park, M.E.P. Rendell, D.K. Yarbrough, S. Chu, L. Xi, S.G. Boxer, M.H. Montrose, and S.J. Remington. Green fluorescent protein variants as ratiometric dual emission pH sensors. 1. Structural characterization and preliminary application. *Biochemistry*, 41(52):15477–15488, 2002.

[6] G. Guerrero, M.S. Siegel, B. Roska, E. Loots, and E.Y. Isacoff. Tuning FlaSh: redesign of the dynamics, voltage range, and color of the genetically encoded optical sensor of membrane potential. *Biophys. J.*, 83(6):3607–3618, 2002.

[7] R. Ando, H. Mizuno, and A. Miyawaki. Regulated fast nucleocytoplasmic shuttling observed by reversible protein highlighting. *Science*, 306(5700):1370–1373, 2004.

[8] G.H. Patterson and J. Lippincott-Schwartz. A photoactivatable GFP for selective photolabeling of proteins and cells. *Science*, 297(5588):1873–1877, 2002.

[9] E. Betzig, G.H. Patterson, R. Sougrat, O.W. Lindwasser, S. Olenych, J.S. Bonifacino, M.W. Davidson, J. Lippincott-Schwartz, and H.F. Hess. Imaging intracellular fluorescent proteins at nanometer resolution. *Science*, 131(5793):1642–1645, 2006.

[10] S.T. Hess, T.P.K. Girirajan, and M.D. Mason. Ultra-high resolution imaging by fluorescence photoactivation localization microscopy. *Biophys. J.*, 91(11):4258–4272, 2006.

[11] M. Bates, B. Huang, G.T. Dempsey, and X. Zhuang. Multicolor super-resolution imaging with photo-switchable fluorescent probes. *Science*, 317(5845):1749–1753, 2007.

[12] S.W. Hell. Microscopy and its focal switch. *Nat. Methods*, 6(1):24–32, 2008.

[13] P.N. Hedde, J. Fuchs, F. Oswald, J. Wiedenmann, and G.U. Nienhaus. Online image analysis software for photoactivation localization microscopy. *Nat. Methods*, 6(10):689–690, 2009.

[14] O. Shimomura, F.H. Johnson, and Y. Saiga. Extraction, purification and properties of aequorin, a bioluminescent protein from the luminous hydromedusan, Aequorea. *J. Cell. Comp. Physiol.*, 59(3):223–239, 1962.

[15] O. Shimomura. Structure of the chromophore of Aequorea green fluorescent protein. *FEBS Lett.*, 140:220–222, 1979.

[16] D.C. Prasher, V.K. Eckenrode, W.W. Ward, F.G. Prendergast, and M.J. Cormier. Primary structure of the Aequorea victoria green-fluorescent protein. *Gene*, 111(2):229–233, 1992.

[17] M. Chalfie, Y. Tu, G. Euskirchen, W.W. Ward, and D.C. Prasher. Green fluorescent protein as a marker for gene expression. *Science*, 263(5148):802, 1994.

[18] G.U. Nienhaus. The green fluorescent protein: a key tool to study chemical processes in living cells. *Angew. Chem., Int. Ed.*, 47(47):8992–8994, 2008.

[19] O. Shimomura, M. Chalfie, and R.Y. Tsien. Constructing and exploiting the fluorescent protein paintbox (Nobel Lecture). *Angew. Chem., Int. Ed.*, 48(31):5612–5626, 2009.

[20] N.C. Shaner, G.H. Patterson, and M.W. Davidson. Advances in fluorescent protein technology. *J. Cell Sci.*, 120(24):4247–4260, 2007.

[21] M.V. Matz, A.F. Fradkov, Y.A. Labas, A.P. Savitsky, A.G. Zaraisky, M.L. Markelov, and S.A. Lukyanov. Fluorescent proteins from nonbioluminescent Anthozoa species. *Nat. Biotechnol.*, 17(10):969–973, 1999.

[22] D.A. Shagin, E.V. Barsova, Y.G. Yanushevich, A.F. Fradkov, K.A. Lukyanov, Y.A. Labas, T.N. Semenova, J.A. Ugalde, A. Meyers, J.M. Nunez, et al. GFP-like proteins as ubiquitous metazoan superfamily: evolution of functional features and structural complexity. *Mol. Biol. Evol.*, 21(5):841, 2004.

[23] S.H.D. Haddock, N. Mastroianni, and L.M. Christianson. A photoactivatable green-fluorescent protein from the phylum Ctenophora. *Proc. R. Soc. B*, 277(1685):1155, 2010.

[24] D.D. Deheyn, K. Kubokawa, J.K. McCarthy, A. Murakami, M. Porrachia, G.W. Rouse, and N.D. Holland. Endogenous green fluorescent protein (GFP) in amphioxus. *Biol. Bull.*, 213(2):95, 2007.

[25] M. Ormö, A.B. Cubitt, K. Kallio, L.A. Gross, R.Y. Tsien, and S.J. Remington. Crystal structure of the Aequorea victoria green fluorescent protein. *Science*, 273(5280):1392, 1996.

[26] F. Yang, L.G. Moss, and G.N. Jr. Phillips. The molecular structure of green fluorescent protein. *Nat. Biotechnol.*, 14(10):1246–1251, 1996.

[27] G.U. Nienhaus and J. Wiedenmann. Structure, dynamics and optical properties of fluorescent proteins: perspectives for marker development. *Chem. Phys. Chem.*, 10(9-10):1369–1379, 2009.

[28] R.Y. Tsien. The green fluorescent protein. *Annu. Rev. Biochem.*, 67(1):509–544, 1998.

[29] A.M. Loening, T.D. Fenn, and S.S. Gambhir. Crystal structures of the luciferase and green fluorescent protein from Renilla reniformis. *J. Mol. Biol.*, 374(4):1017–1028, 2007.

[30] G.S. Baird, D.A. Zacharias, and R.Y. Tsien. Biochemistry, mutagenesis, and oligomerization of DsRed, a red fluorescent protein from coral. *Proc. Natl. Acad. Sci. U. S. A.*, 97(22):11984, 2000.

[31] P.V. Vrzheshch, N.A. Akovbian, S.D. Varfolomeyev, and V.V. Verkhusha. Denaturation and partial renaturation of a tightly tetramerized DsRed protein under mildly acidic conditions. *FEBS Lett.*, 487(2):203–208, 2000.

[32] M.A. Wall, M. Socolich, and R. Ranganathan. The structural basis for red fluorescence in the tetrameric GFP homolog DsRed. *Nat. Struct. Mol. Biol.*, 7(12):1133–1138, 2000.

[33] D. Yarbrough, R.M. Wachter, K. Kallio, M.V. Matz, and S.J. Remington. Refined crystal structure of DsRed, a red fluorescent protein from coral, at 2.0-Å resolution. *Proc. Natl. Acad. Sci. U. S. A.*, 98(2):462, 2001.

[34] G.U. Nienhaus, K. Nienhaus, A. Hölzle, S. Ivanchenko, F. Renzi, F. Oswald, M. Wolff, F. Schmitt, C. Röcker, B. Vallone, W. Weidemann, R. Heilker, H. Nar, and J. Wiedenmann. Photoconvertible fluorescent protein EosFP: biophysical properties and cell biology applications. *Photochem. Photobiol.*, 82(2):351–358, 2006.

[35] V.V. Verkhusha and K.A. Lukyanov. The molecular properties and applications of Anthozoa fluorescent proteins and chromoproteins. *Nat. Biotechnol.*, 22(3):289–296, 2004.

[36] T.F. Schwede, J. Rétey, and G.E. Schulz. Crystal structure of histidine ammonia-lyase revealing a novel polypeptide modification as the catalytic electrophile. *Biochemistry*, 38(17):5355–5361, 1999.

[37] M. Donnelly, F. Fedeles, M. Wirstam, P.E. Siegbahn, and M. Zimmer. Computational analysis of the autocatalytic posttranslational cyclization observed in histidine ammonia-lyase. A comparison with green fluorescent protein. *J. Am. Chem. Soc.*, 123(20):4679–4686, 2001.

[38] B.R. Branchini, J.O. Lusins, and M. Zimmer. A molecular mechanics and database analysis of the structural preorganization and activation of the chromophore-containing hexapeptide fragment in green fluorescent protein. *J. Biomol. Struct. Dyn.*, 14(4):441, 1997.

[39] R.M. Wachter. Chromogenic cross-link formation in green fluorescent protein. *Acc. Chem. Res.*, 40(2):120–127, 2007.

[40] D.P. Barondeau, C.D. Putnam, C.J. Kassmann, J.A. Tainer, and E.D. Getzoff. Mechanism and energetics of green fluorescent protein chromophore synthesis

revealed by trapped intermediate structures. *Proc. Natl. Acad. Sci. U. S. A.*, 100(21):12111, 2003.

[41] L.J. Pouwels, L. Zhang, N.H. Chan, P.C. Dorrestein, and R.M. Wachter. Kinetic Isotope Effect Studies on the de Novo Rate of Chromophore Formation in Fast-and Slow-Maturing GFP Variants. *Biochemistry*, 47(38):10111–10122, 2008.

[42] L.A. Gross, G.S. Baird, R.C. Hoffman, K.K. Baldridge, and R.Y. Tsien. The structure of the chromophore within DsRed, a red fluorescent protein from coral. *Proc. Natl. Acad. Sci. U. S. A.*, 97(22):11990, 2000.

[43] J. Wiedenmann, A. Schenk, C. Röcker, A. Girod, K.D. Spindler, and G.U. Nienhaus. A far-red fluorescent protein with fast maturation and reduced oligomerization tendency from Entacmaea quadricolor (Anthozoa, Actinaria). *Proc. Natl. Acad. Sci. U. S. A.*, 99(18):11646, 2002.

[44] X. Shu, N.C. Shaner, C.A. Yarbrough, R.Y. Tsien, and S.J. Remington. Novel chromophores and buried charges control color in mFruits. *Biochemistry*, 45(32):9639–9647, 2006.

[45] S.J. Remington, R.M. Wachter, D.K. Yarbrough, B. Branchaud, DC Anderson, K. Kallio, and K.A. Lukyanov. zFP538, a yellow-fluorescent protein from Zoanthus, contains a novel three-ring chromophore. *Biochemistry*, 44(1):202–212, 2005.

[46] K.A. Lukyanov, A.F. Fradkov, N.G. Gurskaya, M.V. Matz, Y.A. Labas, A.P. Savitsky, M.L. Markelov, A.G. Zaraisky, X. Zhao, Y. Fang, et al. Natural animal coloration can be determined by a nonfluorescent green fluorescent protein homolog. *J. Biol. Chem.*, 275(34):25879, 2000.

[47] M.L. Quillin, D.M. Anstrom, X. Shu, S. O'Leary, K. Kallio, D.M. Chudakov, and S.J. Remington. Kindling fluorescent protein from Anemonia sulcata: dark-state structure at 1.38 Å resolution. *Biochemistry*, 44(15):5774–5787, 2005.

[48] P.G. Wilmann, J. Petersen, R.J. Devenish, M. Prescott, and J. Rossjohn. Variations on the GFP chromophore: a polypeptide fragmentation within the chromophore revealed in the 2.1-Å crystal structure of a nonfluorescent chromoprotein from Anemonia sulcata. *J. Biol. Chem.*, 280(4):2401, 2005.

[49] M. Andresen, M.C. Wahl, A.C. Stiel, F. Gräter, L.V. Schäfer, S. Trowitzsch, G. Weber, C. Eggeling, H. Grubmüller, S.W. Hell, and S. Jakobs. Structure and mechanism of the reversible photoswitch of a fluorescent protein. *Proc. Natl. Acad. Sci. U. S. A.*, 102(37):13070–13074, 2005.

[50] W. Tomosugi, T. Matsuda, T. Tani, T. Nemoto, I. Kotera, K. Saito, K. Horikawa, and T. Nagai. An ultramarine fluorescent protein with increased photostability and pH insensitivity. *Nat. Methods*, 6(5):351–353, 2009.

[51] R. Heim and R.Y. Tsien. Engineering green fluorescent protein for improved brightness, longer wavelengths and fluorescence resonance energy transfer. *Curr. Biol.*, 6(2):178–182, 1996.

[52] T.T. Yang, P. Sinai, G. Green, P.A. Kitts, Y.T. Chen, L. Lybarger, R. Chervenak, G.H. Patterson, D.W. Piston, and S.R. Kain. Improved fluorescence and dual color detection with enhanced blue and green variants of the green fluorescent protein. *J. Biol. Chem.*, 273(14):8212, 1998.

[53] G.J. Kremers, J. Goedhart, D.J. van den Heuvel, H.C. Gerritsen, and T.W.J. Gadella Jr. Improved green and blue fluorescent proteins for expression in bacteria and mammalian cells. *Biochemistry*, 46(12):3775–3783, 2007.

[54] M.A. Mena, T.P. Treynor, S.L. Mayo, and P.S. Daugherty. Blue fluorescent proteins with enhanced brightness and photostability from a structurally targeted library. *Nat. Biotechnol.*, 24(12):1569–1571, 2006.

[55] H. Ai, N.C. Shaner, Z. Cheng, R.Y. Tsien, and R.E. Campbell. Exploration of new chromophore structures leads to the identification of improved blue fluorescent proteins. *Biochemistry*, 46(20):5904–5910, 2007.

[56] O.M. Subach, I.S. Gundorov, M. Yoshimura, F.V. Subach, J. Zhang, D. Grünwald, E.A. Souslova, D.M. Chudakov, and V.V. Verkhusha. Conversion of red fluorescent protein into a bright blue probe. *Chem. Biol.*, 15(10):1116–1124, 2008.

[57] R. Heim, D.C. Prasher, and R.Y. Tsien. Wavelength mutations and posttranslational autoxidation of green fluorescent protein. *Proc. Natl. Acad. Sci. U. S. A.*, 91(26):12501–12504, 1994.

[58] M.A. Rizzo, G.H. Springer, B. Granada, and D.W. Piston. An improved cyan fluorescent protein variant useful for FRET. *Nat. Biotechnol.*, 22(4):445–449, 2004.

[59] G.J. Kremers, J. Goedhart, E.B. van Munster, and T.W.J. Gadella Jr. Cyan and yellow super fluorescent proteins with improved brightness, protein folding, and FRET Förster radius. *Biochemistry*, 45(21):6570–6580, 2006.

[60] J. Goedhart, L. Van Weeren, M.A. Hink, N.O.E. Vischer, K. Jalink, and T.W.J. Gadella. Bright cyan fluorescent protein variants identified by fluorescence lifetime screening. *Nat. Methods*, 7(2):137–139, 2010.

[61] H. Ai, J.N. Henderson, S.J. Remington, and R.E. Campbell. Directed evolution of a monomeric, bright and photostable version of Clavularia cyan fluorescent protein: structural characterization and applications in fluorescence imaging. *Biochem. J.*, 400(3):531–540, 2006.

[62] R. Heim, A.B. Cubitt, and R.Y. Tsien. Improvement of green fluorescent protein by site-directed mutations. *Nature*, 373(23):663–664, 1995.

[63] H. Ai, S.G. Olenych, P. Wong, M.W. Davidson, and R.E. Campbell. Hue-shifted monomeric variants of Clavularia cyan fluorescent protein: identification of the molecular determinants of color and applications in fluorescence imaging. *BMC Biol.*, 6(1):13, 2008.

[64] J.D. Pédelacq, S. Cabantous, T. Tran, T.C. Terwilliger, and G.S. Waldo. Engineering and characterization of a superfolder green fluorescent protein. *Nat. Biotechnol.*, 24(1):79–88, 2005.

[65] A.B. Cubitt, R. Heim, S.R. Adams, A.E. Boyd, L.A. Gross, and R.Y. Tsien. Understanding, improving and using green fluorescent proteins. *Trends Biochem. Sci.*, 20(11):448–455, 1995.

[66] O. Griesbeck, G.S. Baird, R.E. Campbell, D.A. Zacharias, and R.Y. Tsien. Reducing the environmental sensitivity of yellow fluorescent protein. *J. Biol. Chem.*, 276(31):29188, 2001.

[67] T. Nagai, K. Ibata, E.S. Park, M. Kubota, K. Mikoshiba, and A. Miyawaki. A variant of yellow fluorescent protein with fast and efficient maturation for cell-biological applications. *Nat. Biotechnol.*, 20(1):87–90, 2002.

[68] A.B. Cubitt, L.A. Woollenweber, and R. Heim. Understanding Structure-Function Relationships in the Aequorea victoria Green Fluorescent Protein. *Methods Cell Biol.*, 58:19–30, 1998.

[69] D. Shcherbo, E.A. Souslova, J. Goedhart, T.V. Chepurnykh, A. Gaintzeva, I.I. Shemiakina, T.W.J. Gadella, S. Lukyanov, and D.M. Chudakov. Practical and reliable FRET/FLIM pair of fluorescent proteins. *BMC Biotechnol.*, 9(1):24, 2009.

[70] S. Karasawa, T. Araki, T. Nagai, H. Mizuno, and A. Miyawaki. Cyan-emitting and orange-emitting fluorescent proteins as a donor/acceptor pair for fluorescence resonance energy transfer. *Biochem. J.*, 381(1):307, 2004.

[71] N.C. Shaner, R.E. Campbell, P.A. Steinbach, B.N.G. Giepmans, A.E. Palmer, and R.Y. Tsien. Improved monomeric red, orange and yellow fluorescent proteins derived from Discosoma sp. red fluorescent protein. *Nat. Biotechnol.*, 22(12):1567–1572, 2004.

[72] E.M. Merzlyak, J. Goedhart, D. Shcherbo, M.E. Bulina, A.S. Shcheglov, A.F. Fradkov, A. Gaintzeva, K.A. Lukyanov, S. Lukyanov, T.W.J. Gadella, et al. Bright monomeric red fluorescent protein with an extended fluorescence lifetime. *Nat. Methods*, 4(7):555–557, 2007.

[73] N.C. Shaner, M.Z. Lin, M.R. McKeown, P.A. Steinbach, K.L. Hazelwood, M.W. Davidson, and R.Y. Tsien. Improving the photostability of bright monomeric orange and red fluorescent proteins. *Nat. Methods*, 5(6):545–551, 2008.

[74] S. Kredel, F. Oswald, K. Nienhaus, K. Deuschle, C. Röcker, M. Wolff, R. Heilker, G.U. Nienhaus, and J. Wiedenmann. mRuby, a bright monomeric red fluorescent protein for labeling of subcellular structures. *PLoS One*, 4(2):e4391, 2009.

[75] T. Kogure, H. Kawano, Y. Abe, and A. Miyawaki. Fluorescence imaging using a fluorescent protein with a large Stokes shift. *Methods*, 45(3):223–226, 2008.

[76] T. Kogure, S. Karasawa, T. Araki, K. Saito, M. Kinjo, and A. Miyawaki. A fluorescent variant of a protein from the stony coral Montipora facilitates dual-color single-laser fluorescence cross-correlation spectroscopy. *Nat. Biotechnol.*, 24(5):577–581, 2006.

[77] L. Wang, W.C. Jackson, P.A. Steinbach, and R.Y. Tsien. Evolution of new nonantibody proteins via iterative somatic hypermutation. *Proc. Natl. Acad. Sci. U. S. A.*, 101(48):16745–16749, 2004.

[78] D. Shcherbo, C.S. Murphy, G.V. Ermakova, E.A. Solovieva, T.V. Chepurnykh, A.S. Shcheglov, V.V. Verkhusha, V.Z. Pletnev, K.L. Hazelwood, P.M. Roche, S. Lukyanov, A.G. Zaraisky, M.W. Davidson, and D.M. Chudakov. Far-red fluorescent tags for protein imaging in living tissues. *Biochem. J.*, 418(3):567–574, 2009.

[79] M.Z. Lin, M.R. McKeown, H.L. Ng, T.A. Aguilera, N.C. Shaner, R.E. Campbell, S.R. Adams, L.A. Gross, W. Ma, T. Alber, et al. Autofluorescent proteins with excitation in the optical window for intravital imaging in mammals. *Chem. Biol.*, 16(11):1169–1179, 2009.

[80] D. Shcherbo, I.I. Shemiakina, A.V. Ryabova, K.E. Luker, B.T. Schmidt, E.A. Souslova, T.V. Gorodnicheva, L. Strukova, K.M. Shidlovskiy, and Zaraisky A.G. Lukyanov K.L. Loschenov V.B. Luker G.D. Chudakov D.M. Britanova, O.V. Near-infrared fluorescent proteins. *Nature Methods*, 7(10):827–829, 2010.

[81] S. Gayda, P.N. Hedde, K. Nienhaus, and G.U. Nienhaus. *Springer Series on Fluorescence: Far-Field Optical Nanoscopy 3D.* Springer, submitted.

[82] K. Brejc, T.K. Sixma, P.A. Kitts, S.R. Kain, R.Y. Tsien, M. Ormö, and S.J. Remington. Structural basis for dual excitation and photoisomerization of the Aequorea victoria green fluorescent protein. *Proc. Natl. Acad. Sci. U. S. A.*, 94(6):2306–2311, 1997.

[83] J.J. van Thor, A.J. Pierik, I. Nugteren-Roodzant, A. Xie, and K.J. Hellingwerf. Characterization of the photoconversion of green fluorescent protein with FTIR spectroscopy. *Biochemistry*, 37(48):16915–16921, 1998.

[84] M.A. Elsliger, R.M. Wachter, G.T. Hanson, K. Kallio, and S.J. Remington. Structural and spectral response of green fluorescent protein variants to changes in pH. *Biochemistry*, 38(17):5296–5301, 1999.

[85] M. Chattoraj, B.A. King, G.U. Bublitz, and S.G. Boxer. Ultra-fast excited state dynamics in green fluorescent protein: multiple states and proton transfer. *Proc. Natl. Acad. Sci. U. S. A.*, 93(16):8362–8367, 1996.

[86] A. Sawano and A. Miyawaki. Directed evolution of green fluorescent protein by a new versatile PCR strategy for site-directed and semi-random mutagenesis. *Nucleic Acids Res.*, 28(16):e78, 2000.

[87] K. Nienhaus, F. Renzi, B. Vallone, J. Wiedenmann, and G.U. Nienhaus. Chromophore-protein interactions in the anthozoan green fluorescent protein asFP499. *Biophys. J.*, 91(11):4210–4220, 2006.

[88] U. Haupts, S. Maiti, P. Schwille, and W.W. Webb. Dynamics of fluorescence fluctuations in green fluorescent protein observed by fluorescence correlation spectroscopy. *Proc. Natl. Acad. Sci. U. S. A.*, 95(23):13573–13578, 1998.

[89] C. Scharnagl, R. Raupp-Kossmann, and S.F. Fischer. Molecular basis for pH sensitivity and proton transfer in green fluorescent protein: protonation and conformational substates from electrostatic calculations. *Biophys. J.*, 77(4):1839–1857, 1999.

[90] K. Nienhaus, F. Renzi, B. Vallone, J. Wiedenmann, and G.U. Nienhaus. Exploring chromophore-protein interactions in fluorescent protein cmFP512 from Cerianthus membranaceus: X-ray structure analysis and optical spectroscopy. *Biochemistry*, 45(43):12942–12953, 2006.

[91] C. Fang, R.R. Frontiera, R. Tran, and R.A. Mathies. Mapping GFP structure evolution during proton transfer with femtosecond Raman spectroscopy. *Nature*, 462(7270):200–204, 2009.

[92] S. Olsen, K. Lamothe, and T.J. Martinez. Protonic gating of excited-state twisting and charge localization in GFP chromophores: a mechanistic hypothesis for reversible photoswitching. *J. Am. Chem. Soc.*, 132(4):1192–1193, 2010.

[93] R.M. Dickson, A.B. Cubitt, R.Y. Tsien, and W.E. Moerner. On/off blinking and switching behaviour of single molecules of green fluorescent protein. *Nature*, 388(6640):355–358, 1997.

[94] E.J.G. Peterman, S. Brasselet, and W.E. Moerner. The fluorescence dynamics of single molecules of green fluorescent protein. *J. Phys. Chem. A*, 103(49):10553–10560, 1999.

[95] M.F. Garcia-Parajo, G.M.J. Segers-Nolten, J.A. Veerman, J. Greve, and N.F. Van Hulst. Real-time light-driven dynamics of the fluorescence emission in

single green fluorescent protein molecules. *Proc. Natl. Acad. Sci. U. S. A.*, 97(13):7237–7242, 2000.

[96] G. Jung, C. Bräuchle, and A. Zumbusch. Two-color fluorescence correlation spectroscopy of one chromophore: Application to the E222Q mutant of the green fluorescent protein. *J. Chem. Phys.*, 114(7):3149–3156, 2001.

[97] Y. Liu, H.R. Kim, and A.A. Heikal. Structural basis of fluorescence fluctuation dynamics of green fluorescent proteins in acidic environments. *J. Phys. Chem. B*, 110(47):24138–24146, 2006.

[98] W. Weber, V. Helms, J.A. McCammon, and P.W. Langhoff. Shedding light on the dark and weakly fluorescent states of green fluorescent proteins. *Proc. Natl. Acad. Sci. U. S. A.*, 96(11):6177–6182, 1999.

[99] M.B. Elowitz, M.G. Surette, P.E. Wolf, J. Stock, and S. Leibler. Photoactivation turns green fluorescent protein red. *Curr. Biol.*, 7(10):809–812, 1997.

[100] G.J. Kremers, K.L. Hazelwood, C.S. Murphy, M.W. Davidson, and D.W. Piston. Photoconversion in orange and red fluorescent proteins. *Nat. Methods*, 6(5):355–358, 2009.

[101] J.J. van Thor, T. Gensch, K.J. Hellingwerf, and L.N. Johnson. Phototransformation of green fluorescent protein with UV and visible light leads to decarboxylation of glutamate 222. *Nat. Struct. Mol. Biol.*, 9(1):37–41, 2001.

[102] A.F. Bell, D. Stoner-Ma, R.M. Wachter, and P.J. Tonge. Light-driven decarboxylation of wild-type green fluorescent protein. *J. Am. Chem. Soc.*, 125(23):6919–6926, 2003.

[103] T.M.H. Creemers, A.J. Lock, V. Subramaniam, T.M. Jovin, and S. Völker. Three photoconvertible forms of green fluorescent protein identified by spectral hole-burning. *Nat. Struct. Biol.*, 6:557–559, 1999.

[104] H. Yokoe and T. Meyer. Spatial dynamics of GFP-tagged proteins investigated by local fluorescence enhancement. *Nat. Biotechnol.*, 14(10):1252–1256, 1996.

[105] D.M. Chudakov, V.V. Verkhusha, D.B. Staroverov, E.A. Souslova, S. Lukyanov, and K.A. Lukyanov. Photoswitchable cyan fluorescent protein for protein tracking. *Nat. Biotechnol.*, 22(11):1435–1439, 2004.

[106] F.V. Subach, V.N. Malashkevich, W.D. Zencheck, H. Xiao, G.S. Filonov, S.C. Almo, and V.V. Verkhusha. Photoactivation mechanism of PAmCherry based on crystal structures of the protein in the dark and fluorescent states. *Proc. Natl. Acad. Sci U.S.A.*, 106(50):21097–21102, 2009.

[107] F.V. Subach, G.H. Patterson, M. Renz, J. Lippincott-Schwartz, and V.V. Verkhusha. Bright monomeric photoactivatable red fluorescent protein for two-color super-resolution sptPALM of live cells. *J. Am. Chem. Soc.*, 132(18):6481–6491, 2010.

[108] H. Mizuno, T.K. Mal, K.I. Tong, R. Ando, T. Furuta, M. Ikura, and A. Miyawaki. Photo-induced peptide cleavage in the green-to-red conversion of a fluorescent protein. *Mol. Cell*, 12(4):1051–1058, 2003.

[109] K. Nienhaus, G.U. Nienhaus, J. Wiedenmann, and H. Nar. Structural basis for photo-induced protein cleavage and green-to-red conversion of fluorescent protein EosFP. *Proc. Natl. Acad. Sci. U. S. A.*, 102(26):9156–9159, 2005.

[110] X. Li, L.W. Chung, H. Mizuno, A. Miyawaki, and K. Morokuma. Competitive Mechanistic Pathways for Green-to-Red Photoconversion in the Fluorescent Protein Kaede: A Computational Study. *J. Phys. Chem. B*, 114(49):16666–16675, 2010.

[111] I. Hayashi, H. Mizuno, K.I. Tong, T. Furuta, F. Tanaka, M. Yoshimura, A. Miyawaki, and M. Ikura. Crystallographic evidence for water-assisted photo-induced peptide cleavage in the stony coral fluorescent protein Kaede. *J. Mol. Biol.*, 372(4):918–926, 2007.

[112] M. Lelimousin, V. Adam, G.U. Nienhaus, D. Bourgeois, and M.J. Field. Photoconversion of the Fluorescent Protein EosFP: A Hybrid Potential Simulation Study Reveals Intersystem Crossings. *J. Am. Chem. Soc.*, 131(46):16814–16823, 2009.

[113] N.G. Gurskaya, V.V. Verkhusha, A.S. Shcheglov, D.B. Staroverov, T.V. Chepurnykh, A.F. Fradkov, S. Lukyanov, and K.A. Lukyanov. Engineering of a monomeric green-to-red photoactivatable fluorescent protein induced by blue light. *Nat. Biotechnol.*, 24(4):461–465, 2006.

[114] H. Tsutsui, S. Karasawa, H. Shimizu, N. Nukina, and A. Miyawaki. Semi-rational engineering of a coral fluorescent protein into an efficient highlighter. *EMBO Rep.*, 6(3):233–238, 2005.

[115] R. Ando, H. Hama, M. Yamamoto-Hino, H. Mizuno, and A. Miyawaki. An optical marker based on the UV-induced green-to-red photoconversion of a fluorescent protein. *Proc. Natl. Acad. Sci. U. S. A.*, 99(20):12651–12656, 2002.

[116] J. Wiedenmann, S. Ivanchenko, F. Oswald, F. Schmitt, C. Röcker, A. Salih, K.D. Spindler, and G.U. Nienhaus. EosFP, a fluorescent marker protein with UV-inducible green-to-red fluorescence conversion. *Proc. Natl. Acad. Sci. U. S. A.*, 101(45):15905, 2004.

[117] S.A. McKinney, C.S. Murphy, K.L. Hazelwood, M.W. Davidson, and L.L. Looger. A bright and photostable photoconvertible fluorescent protein. *Nat. Methods*, 6(2):131–133, 2009.

[118] J. Fuchs, S. Böhme, F. Oswald, P.N. Hedde, M. Krause, J. Wiedenmann, and G.U. Nienhaus. A photoactivatable marker protein for pulse-chase imaging with superresolution. *Nat. Methods*, 7(8):627–630, 2010.

[119] M. Andresen, A.C. Stiel, S. Trowitzsch, G. Weber, C. Eggeling, M.C. Wahl, S.W. Hell, and S. Jakobs. Structural basis for reversible photoswitching in Dronpa. *Proc. Natl. Acad. Sci U.S.A.*, 104(32):13005–13009, 2007.

[120] V. Adam, M. Lelimousin, S. Boehme, G. Desfonds, K. Nienhaus, M.J. Field, J. Wiedenmann, S. McSweeney, G.U. Nienhaus, and D. Bourgeois. Structural characterization of IrisFP, an optical highlighter undergoing multiple photo-induced transformations. *Proc. Natl. Acad. Sci U.S.A.*, 105(47):18343–18348, 2008.

[121] S. Abbruzzetti, R. Bizzarri, S. Luin, R. Nifosi, B. Storti, C. Viappiani, and F. Beltram. Photoswitching of E222Q GFP mutants:"concerted"c mechanism of chromophore isomerization and protonation. *Photochem. Photobiol. Sci.*, 9(10):1307–1319, 2010.

[122] P.G. Wilmann, K. Turcic, J.M. Battad, M.C.J. Wilce, R.J. Devenish, M. Prescott, and J. Rossjohn. The 1.7 Å crystal structure of Dronpa: a photoswitchable green fluorescent protein. *J. Mol. Biol.*, 364(2):213–224, 2006.

[123] D.M. Chudakov, A.V. Feofanov, N.N. Mudrik, S. Lukyanov, and K.A. Lukyanov. Chromophore environment provides clue to "kindling fluorescent protein" riddle. *J. Biol. Chem.*, 278(9):7215–7219, 2003.

[124] L.V. Schäfer, G. Groenhof, A.R. Klingen, G.M. Ullmann, M. Boggio-Pasqua, M.A. Robb, and H. Grubmüller. Photoswitching of the fluorescent protein asFP595: mechanism, proton pathways, and absorption spectra. *Angew. Chem., Int. Ed.*, 119(4):536–542, 2007.

[125] H. Mizuno, T.K. Mal, M. Wälchli, A. Kikuchi, T. Fukano, R. Ando, J. Jeyakanthan, J. Taka, Y. Shiro, M. Ikura, et al. Light-dependent regulation of structural flexibility in a photochromic fluorescent protein. *Proc. Natl. Acad. Sci U.S.A.*, 105(27):9227–9232, 2008.

[126] H. Mizuno, T.K. Mal, M. Wälchli, T. Fukano, M. Ikura, and A. Miyawaki. Molecular basis of photochromism of a fluorescent protein revealed by direct 13C detection under laser illumination. *J. Biomol. NMR*, 48(4):237–246, 2010.

[127] A.C. Stiel, S. Trowitzsch, G. Weber, M. Andresen, C. Eggeling, S.W. Hell, S. Jakobs, and M.C. Wahl. 1.8 Å bright-state structure of the reversibly switchable fluorescent protein Dronpa guides the generation of fast switching variants. *Biochem. J.*, 402(1):35–42, 2007.

[128] J.N. Henderson, H. Ai, R.E. Campbell, and S.J. Remington. Structural basis for reversible photobleaching of a green fluorescent protein homologue. *Proc. Natl. Acad. Sci U.S.A.*, 104(16):6672–6677, 2007.

[129] X. He, A.F. Bell, and P.J. Tonge. Ground state isomerization of a model green fluorescent protein chromophore. *FEBS Lett.*, 549(1-3):35–38, 2003.

[130] S. Violot, P. Carpentier, L. Blanchoin, and D. Bourgeois. Reverse pH-dependence of chromophore protonation explains the large Stokes shift of the red fluorescent protein mKeima. *J. Am. Chem. Soc.*, 131(30):10356–10357, 2009.

[131] M. Andresen, A.C. Stiel, J. Fölling, D. Wenzel, A. Schönle, A. Egner, C. Eggeling, S.W. Hell, and S. Jakobs. Photoswitchable fluorescent proteins enable monochromatic multilabel imaging and dual color fluorescence nanoscopy. *Nat. Biotechnol.*, 26(9):1035–1040, 2008.

[132] A.C. Stiel, M. Andresen, H. Bock, M. Hilbert, J. Schilde, A. Schönle, C. Eggeling, A. Egner, S.W. Hell, and S. Jakobs. Generation of monomeric reversibly switchable red fluorescent proteins for far-field fluorescence nanoscopy. *Biophys. J.*, 95(6):2989–2997, 2008.

[133] F.V. Subach, L. Zhang, T.W.J. Gadella, N.G. Gurskaya, K.A. Lukyanov, and V.V. Verkhusha. Red fluorescent protein with reversibly photoswitchable absorbance for photochromic FRET. *Chem. Biol.*, 17(7):745–755, 2010.

[134] Hoffman R.M. Wouters F.S. Wessels J.T., Yamauchi K. Advances in cellular, subcellular, and nanoscale imaging in vitro and in vivo. *Cytometry A*, 77(7):667–676, 2010.

[135] W.E. Moerner. New directions in single-molecule imaging and analysis. *Proc. Natl. Acad. Sci U.S.A.*, 104(31):12596–12602, 2007.

[136] H. Shroff, C.G. Galbraith, J.A. Galbraith, H. White, J. Gillette, S. Olenych, M.W. Davidson, and E. Betzig. Dual-color superresolution imaging of genetically expressed probes within individual adhesion complexes. *Proc. Natl. Acad. Sci U.S.A.*, 104(51):20308–20313, 2007.

[137] C.N. Pace, F. Vajdos, L. Fee, G. Grimsley, and T. Gray. How to measure and predict the molar absorption coefficient of a protein. *Protein Sci.*, 4(11):2411–2423, 1995.

[138] A. Schenk, S. Ivanchenko, C. Röcker, J. Wiedenmann, and G.U. Nienhaus. Photodynamics of red fluorescent proteins studied by fluorescence correlation spectroscopy. *Biophys. J.*, 86(1):384–394, 2004.

[139] C. Röcker, M. Pötzl, F. Zhang, W.J. Parak, and G.U. Nienhaus. A quantitative fluorescence study of protein monolayer formation on colloidal nanoparticles. *Nat. Nanotechnol.*, 4(9):577–580, 2009.

[140] V. Adam, H. Mizuno, A. Grichine, J. Hotta, Y. Yamagata, B. Moeyaert, G.U. Nienhaus, A. Miyawaki, D. Bourgeois, and J. Hofkens. Data storage based on photochromic and photoconvertible fluorescent proteins. *J. Biotechnol.*, 149(4):289–298, 2010.

[141] J. Wiedenmann, F. Oswald, and G.U. Nienhaus. Fluorescent proteins for live cell imaging: opportunities, limitations, and challenges. *IUBMB Life*, 61(11):1029–1042, 2009.

[142] J. Wiedenmann, S. Gayda, V. Adam, F. Oswald, K. Nienhaus, D. Bourgeois, and G.U. Nienhaus. From EosFP to mIrisFP: structure-based development of advanced photoactivatable marker proteins of the GFP-family. *J. Biophotonics*, pages doi: 10.1002/jbio.201000122, Epub ahead of print, 2011.

[143] C.E.L. Stokes, D. Murphy, J.F.R. Paton, and S. Kasparov. Dynamics of a transgene expression in acute rat brain slices transfected with adenoviral vectors. *Exp. Physiol.*, 88(4):459–466, 2003.

[144] C.K. Choi, M. Vicente-Manzanares, J. Zareno, L.A. Whitmore, A. Mogilner, and A.R. Horwitz. Actin and α-actinin orchestrate the assembly and maturation of nascent adhesions in a myosin II motor-independent manner. *Nat. Cell Biol.*, 10(9):1039–1050, 2008.

[145] D.J. Webb, J.T. Parsons, and A.F. Horwitz. Adhesion assembly, disassembly and turnover in migrating cells–over and over and over again. *Nat. Cell Biol.*, 4(4):E97–E100, 2002.

[146] X. Li, L.W. Chung, H. Mizuno, A. Miyawaki, and K. Morokuma. A theoretical study on the nature of on-and off-states of reversibly photoswitching fluorescent protein Dronpa: absorption, emission, protonation, and Raman. *J. Phys. Chem. B*, 114(2):1114–1126, 2009.

[147] R. Bizzarri, M. Serresi, F. Cardarelli, S. Abbruzzetti, B. Campanini, C. Viappiani, and F. Beltram. Single amino acid replacement makes Aequorea victoria fluorescent proteins reversibly photoswitchable. *J. Am. Chem. Soc.*, 132(1):85–95, 2009.

[148] S. Habuchi, R. Ando, P. Dedecker, W. Verheijen, H. Mizuno, A. Miyawaki, and J. Hofkens. Reversible single-molecule photoswitching in the GFP-like fluorescent protein Dronpa. *Proc. Natl. Acad. Sci. U. S. A.*, 102(27):9511–9516, 2005.

[149] S. Habuchi, P. Dedecker, J. Hotta, C. Flors, R. Ando, H. Mizuno, A. Miyawaki, and J. Hofkens. Photo-induced protonation/deprotonation in the GFP-like fluorescent protein Dronpa: mechanism responsible for the reversible photoswitching. *Photochem. Photobiol. Sci.*, 5(6):567–576, 2006.

[150] P. Dedecker, J. Hotta, R. Ando, A. Miyawaki, Y. Engelborghs, and J. Hofkens. Fast and reversible photoswitching of the fluorescent protein Dronpa as evidenced by fluorescence correlation spectroscopy. *Biophys. J.*, 91(5):L45–L47, 2006.

[151] S.L.C. Moors, S. Michielssens, C. Flors, P. Dedecker, J. Hofkens, and A. Ceulemans. How Is cis-trans Isomerization Controlled in Dronpa Mutants? A

Replica Exchange Molecular Dynamics Study. *J. Chem. Theory Comput.*, 4(6):1012–1020, 2008.

[152] T. Brakemann, G. Weber, M. Andresen, G. Groenhof, A.C. Stiel, S. Trowitzsch, C. Eggeling, H. Grubmüller, S.W. Hell, M.C. Wahl, et al. Molecular basis of the light-driven switching of the photochromic fluorescent protein Padron. *J. Biol. Chem.*, 285(19):14603–14609, 2010.

[153] J.N. Henderson and S.J. Remington. Crystal structures and mutational analysis of amFP486, a cyan fluorescent protein from Anemonia majano. *Proc. Natl. Acad. Sci. U. S. A.*, 102(36):12712–12717, 2005.

[154] T.A. Schüttrigkeit, T. Feilitzsch, C.K. Kompa, K.A. Lukyanov, A.P. Savitsky, A.A. Voityuk, and M.E. Michel-Beyerle. Femtosecond study of light-induced fluorescence increase of the dark chromoprotein asFP595. *Chem. Phys.*, 323(2-3):149–160, 2006.

[155] N.J. Turro. *Modern molecular photochemistry.* Univ Science Books, 1991.

[156] G. Jackson and G. Porter. Acidity constants in the triplet state. *Proc. R. Soc. London, Ser. A*, 260(1300):13–30, 1961.

[157] E. Fron, C. Flors, G. Schweitzer, S. Habuchi, H. Mizuno, R. Ando, F.C. De Schryver, A. Miyawaki, and J. Hofkens. Ultrafast excited-state dynamics of the photoswitchable protein Dronpa. *J. Am. Chem. Soc.*, 129(16):4870–4871, 2007.

[158] A.R. Faro, V. Adam, P. Carpentier, C. Darnault, D. Bourgeois, and E. de Rosny. Low-temperature switching by photoinduced protonation in photochromic fluorescent proteins. *Photochem. Photobiol. Sci.*, 9(2):254–262, 2010.

Appendix

Danksagung

An dieser Stelle möchte ich mich bei einigen Menschen bedanken, die maßgeblich zum Gelingen dieser Arbeit beigetragen haben.

Prof. G. U. Nienhaus danke ich für die Gelegenheit meine Dissertation in seiner Abteilung anfertigen zu dürfen. Er hat mir damit die seltene Chance gegeben, zu sehen wie fließend die Übergänge zwischen den einzelnen Disziplinen sind und wie sehr sie voneinander profitieren können. Außerdem möchte ich ihm besonders für die Unterstützung meiner Arbeit danken, nicht nur für die fachliche Hilfe, sondern auch für die vielen Möglichkeiten, die er mir geboten hat. Dabei habe ich unter seiner Anleitung sehr viel gelernt, angefangen von der wissenschaftlichen Herangehensweise bis hin zur Präsentation von Ergebnissen.

Karin Nienhaus danke ich für die geduldige Unterstützung und die vielen intensiven Diskussionen. Ihr Talent auf anspornende Weise konstruktiv kritisch zu hinterfragen hat mich in meiner Arbeit immer wieder voran gebracht. Sie hat mir dabei immer das Gefühl vermittelt, dass etwaige Schwachpunkte keine Hindernisse sind, sondern nur Herausforderungen, die es zu überwinden gilt. Mein größter Dank gilt ihr allerdings dafür, dass sie so viel Interesse an diesem Thema gezeigt hat. Ihre Begeisterung am Forschen ist einfach mitreißend und immer wieder motivierend!

Carlheinz Röcker, *Jochen Fuchs*, *Per Niklas Hedde* und *Robert Rieger* danke ich für die vielen Diskussionen, die guten Ideen und Anregungen und vor allem für ihre Unterstützung bei den zahlreichen physikalischen und technischen Fragen, an die sie mich Schritt für Schritt herangeführt haben.

Uwe Theilen und *Susanne Matschulo*, unseren guten Geistern aus dem Biochemielabor, danke ich für ihre tatkräftige Unterstützung bei der Generierung und Aufreinigung der Proteine. Damit haben sie mir so manches Mal den Rücken frei gehalten.

Die letzten Jahre waren eine wirklich schöne Zeit für mich und das verdanke ich vor allem meinen Kollegen, die bald auch Freunde für mich waren. *Elena, Robert, Stefan* und all den anderen, die ich hier leider gar nicht alle aufzählen kann, möchte ich ganz besonders für ihr immer offenes Ohr danken ...und für das abwechslungsreiche *Entertainment*.

Kay, mein Mann, hat mich begleitet, seit ich meine ersten Schritte in eine Universität gesetzt habe. Woher er in den letzten Jahren die unerschöpfliche Geduld aufgebracht hat, sich immer wieder die 'neuesten Erkenntnisse' über Citratzyklus & Co und später IrisFP anzuhören, bleibt hierbei sein Geheimnis. Ihm möchte ich besonders für sein Vertrauen in mich danken, und dafür, dass er mich so bedingungslos unterstützt. Er hat mir damit immer wieder geholfen scheinbar unüberwindbare Aufgaben zu bewältigen, sei es 'Anorganische Chemie II' im 2. Semester oder den Wust an unorganisierten Gedanken beim Schreiben dieser Arbeit.

List of Publications

S. Gayda, P.N. Hedde, K. Nienhaus, G.U. Nienhaus **'Probes for Nanoscopy: Fluorescent Proteins'** in Springer Series on Fluorescence: Far-Field Optical Microscopy, eds.: P. Tinnefeld, C. Eggeling and S. W, Hell, in press. , submitted

J. Wiedenmann, S. Gayda, V. Adam, F. Oswald, K. Nienhaus, D. Bourgeois, G.U. Nienhaus (2011) 'From EosFP to mIrisFP: structure-based development of advanced photoactivatable marker proteins of the GFP-family.' *J. Biophotonics* **4**(3): DOI: 10.1002/jbio.201000122

J. Fuchs*, S. Böhme*, F. Oswald, P.N. Hedde, M. Krause, J. Wiedenmann , G. U. Nienhaus , 'A photoactivatable marker protein for pulse-chase imaging with superresolution.' *Nature Methods* **7**(8): 627-30 (2010)
*authors contributed equally to this work

V. Adam, M. Lelimousin, S. Böhme, G. Desfonds, K. Nienhaus, M.J. Field, J. Wiedenmann, S. McSweeney, G. U. Nienhaus, D. Bourgeois, 'Structural characterization of IrisFP, an optical highlighter undergoing multiple photo-induced transformations', *PNAS*, **105**(47): 18343-18348 (2008)

List of Presentations

10/2010	S. Gayda, K. Nienhaus, G. U. Nienhaus, 'Chromophore isomerization pathways in mIrisGFP', *Poster* presented at the German Biophysical Society Meeting in Bochum
07/2009	S. Böhme, V. Adam, K. Nienhaus, D. Bourgeois, G.U. Nienhaus , 'Multiple Photoactivation of IrisFP', *Poster* presented at the European Biophysics Congress in Genoa
02/2009	S. Böhme, V. Adam, K. Nienhaus, D. Bourgeois, G.U. Nienhaus , 'Structural Background of Photoinduced Transformations in IrisFP', *Talk* presented at Neutrons and X-rays Meets Biology Workshop in Berlin
10/2008	S. Böhme, V. Adam, K. Nienhaus, D. Bourgeois, G.U. Nienhaus, 'Multiple Photoinduced Transformations of IrisFP', *Poster* presented at the German Biophysical Society Meeting in Berlin
06/2008	D. Meyer, S. Böhme, R. Golbik, G. Will, K. Tittmann, 'Glu 483 is involved in multiple steps of LpPOX catalysis', *Poster* presented at Chemical Biology of Thiamine in Wittenberg

Curriculum Vitae

Personal Information

Date and Place of Birth	28/12/1982 in Leipzig (Germany)
Birth Name	Böhme
Citizenship	German

Education

10/2009 - present	*PhD* (continuation of work from Ulm) Karlsruhe Institute of Technology, Institute for Applied Physics and Center for Functional Nanostructures Research Group Prof. Dr. Nienhaus
08/2007 - 09/2009	*PhD* (engineering and characterization of photoactivatable fluorescent proteins), University of Ulm, Institute for Biophysics (Prof. Dr. Nienhaus)
09/2001 - 07/2007	*Diploma Biochemistry* (emphasis: enzymology) Martin-Luther-University Halle-Wittenberg
09/1993 - 07/2001	Gymnasium Schkeuditz Certificate: Abitur